Magnetic T^3-Atomic and Light-Based Gravimetry

Novel Approaches Beyond Traditional Methods

Tesis que para obtener el grado de
Doctor en Física

Presenta:

M.C. Edgar Alberto Zúñiga Pérez

Asesor: Dr. Eduardo Gómez García

Facultad de Ciencias
Universidad Autónoma de San Luis Potosí

San Luis Potosí, S.L.P., México
Noviembre 2025

Magnetic T^3-Atomic and Light-Based Gravimetry

Contents

Preface

The present work summarizes the research I conducted during my doctoral studies at the Facultad de Ciencias of the Universidad Autónoma de San Luis Potosí, spanning the period 2022–2026. When I entered the doctoral program in 2022, I chose to join the Cold Atoms Group under the supervision of Dr. Eduardo Gómez. One of the main research areas of this group is gravimetry, the science of measuring gravity. Gravimeters play a crucial role in a wide range of scientific and technological applications, ranging from navigation and inertial guidance [**1**]to the detection of gravitational waves [**2, 3, 4**], determination of fundamental constants such as the fine-structure constant [**5**] and Newton's gravitational constant G [**6**], and experimental verification of general relativistic predictions [**7**]. In recent years, gravimetric sensors exploiting atom interferometry [**8, 9, 10**] have proven to be particularly powerful platforms, finding use in areas as diverse as climate studies [**11**], geodetic surveying [**12**], archaeological prospection [**13, 14**], monitoring of subsurface hydrology [**15**], and surveillance of volcanic systems [**16**]. For these reasons, the ultra-high-precision measurement of gravity is of particular interest, making gravimetry an active and important area of current research.

The central theme of my thesis is the development and analysis of alternative approaches to gravimetry based on quantum and optical interference, with a particular emphasis on methods that go beyond the standard light-pulse atom interferometer [**17**]. The work is organized around two main lines of research, each of which gave rise to a scientific article:

1. Magnetic T^3-atomic gravimetry
The first part of this thesis is devoted to a detailed study of a gravimeter based on a state-dependent magnetic acceleration of atomic wave packets in a magnetic field gradient. In this scheme, a sequence of microwave pulses creates and manipulates a superposition of internal states that experience different accelerations, causing the spatial branches of the wave function to separate and recombine. Unlike traditional Raman-based atomic gravimeters, where the interferometric phase scales as T^2 with the interrogation time, the phase in this "magnetic" interferometer scales as T^3, which is the origin of the name T^3-gravimetry.

The key results of this research, including a semiclassical and a quantum derivation of the interferometer phase and an analysis of the limits imposed by the expansion of the atomic cloud, were published in *Physical Review A* under the title *"Precision limits of magnetic T^3-atomic gravimetry due to atomic cloud expansion"* (co-authored with Eduardo Gómez and Luis Castaños).

For reasons of space and focus, the journal article could not include many of the intermediate derivations, alternative approaches, and complementary calculations that were essential to the development of the work. Chapter 1 of this thesis ("The Magnetic Gravimeter") is intended to fill that gap. There, I present:

- A complete semiclassical treatment of the pulse sequence and the resulting phase shift, including a comparison between position, velocity, and acceleration splittings.
- A full quantum-mechanical derivation of the interferometer phase using the exact solution of the center-of-mass dynamics in a magnetic field gradient.
- A detailed analysis of detuning effects induced by the Zeeman shift in an inhomogeneous magnetic field, and the resulting constraint on the spatial extent ("warning width") of the atomic wave packet during the microwave pulses.
- Two complementary models for the expansion of the atomic cloud: (i) the evolution of a single Gaussian wave packet, and (ii) the evolution of a thermal ensemble released from a harmonic trap, treated with the density-matrix formalism.
- An estimate of the achievable gravimetric precision as a function of experimental parameters (microwave power, magnetic-field gradient, trap temperature, etc.), and a discussion of intrinsic decoherence and acceleration gradients.

In this sense, the first chapter can be read both as an expanded, self-contained version of the published article and as a technical appendix that collects many of the calculations and insights that did not fit within the constraints of a journal manuscript.

2. Light-based gravimetry

After completing the main part of the work on the magnetic gravimeter, I turned to a conceptually related but physically distinct idea: measuring gravity using light itself, via the gravitational redshift, rather than using matter waves as probes. The motivation for this second line of research arose from discussions with my advisor, Eduardo Gómez, about whether one could build an interferometric gravimeter that relies purely on photons propagating in a gravitational potential.

The basic proposal, which is developed in detail in Chapter 2 ("The Light-based Gravimeter"), is to use an optical interferometer in which one arm remains near the Earth's surface while the other arm extends to large altitudes (for example, toward a satellite or a lunar retroreflector). The light in the long arm experiences a gravitational redshift as it climbs out of the potential and back, and this results in a small but measurable phase shift in the interference pattern. Although the idea is simple in spirit, its quantitative analysis is subtle and requires careful treatment of the gravitational potential, atmospheric effects, beam propagation, and systematic errors.

The main results of this second part of the thesis, obtained in collaboration with Eduardo Gómez, are summarized in the article *"Light-based Gravimetry"*, which is currently under review. In the thesis, I present an expanded version of that work, including:

- A derivation of the interferometric phase shift due to gravitational redshift in realistic Earth–Moon–Sun configurations, with explicit separation of the contributions from geometry, the Earth's field, and external bodies.
- An estimation of the achievable sensitivity to g and a comparison with state-of-the-art atomic gravimeters, highlighting conceptual similarities and practical differences.
- A detailed discussion of atmospheric effects (refractive-index variations, refraction, Rayleigh scattering) and laser-beam systematics (Rayleigh range, mode matching, Gouy phase, beam misalignment, Doppler shifts).
- A unified perspective showing that, at a fundamental level, both light-based and matter-based gravimeters are governed by the same underlying phase expression: the action along each path divided by $\hbar$, leading to an interferometer phase of the form $\Delta\Phi \propto k' g T^2$ under appropriate limits.

As in the first chapter, many of the technical steps, alternative derivations, and side calculations that were omitted or abbreviated in the manuscript are fully developed here, with the aim of providing a complete and transparent account of the reasoning that led to our conclusions.

Beyond presenting my specific contributions, this thesis also reflects my personal scientific trajectory during the Ph.D. I began by working on a relatively new variant of atomic interferometry—the magnetic T^3-gravimeter—and that experience shaped how I later approached the more speculative proposal of a light-based gravimeter. In both cases, I tried to maintain a balance between physical intuition and mathematical rigor, and to connect idealized models with realistic experimental constraints.

The thesis is structured as follows:

- The **Preface** (this section) explains the origin, context, and structure of the work.
- **Chapter 1**: *The Magnetic Gravimeter* — complements and extends the results published in *Physical Review A*, providing a comprehensive theoretical treatment of the technique and its limitations.
- **Chapter 2**: *The Light-based Gravimeter* — presents the theoretical foundations and feasibility analysis of a gravimeter based solely on light, along with a comparison with matter-based approaches.
- The **Appendix** contains technical material, including numerical simulations used to study intrinsic decoherence in the magnetic gravimeter.

Acknowledgments

This work would not have been possible without the guidance, patience, and insight of my advisor, Dr. Eduardo Gómez García, whose ideas and questions were fundamental to both projects. I am also grateful to Dr. Luis Castaños for his collaboration on the magnetic gravimeter and for many stimulating discussions. I thank my colleagues and friends in the research group and at the Facultad de Ciencias for their support over these years.

Finally, I wish to acknowledge the support of my family, whose encouragement and confidence sustained me throughout the long and often demanding process that culminates in this thesis.

1 The Magnetic Gravimeter

1.1 Intermission

The purpose of this chapter is to serve as a complement to the article *Precision limits of magnetic T^3-atomic gravimetry due to atomic cloud expansion* that I published[1] in *Physical Review A* **[18]** during my Ph.D. studies. Some calculations and ideas were left out of the final paper during the revision process or were shortened for brevity. In this chapter, I will present them.

1.2 Concept of the technique

The operating principle of atomic gravimetry relies on coherently dividing an atomic wave packet into two components and subsequently recombining them. Because each component propagates at a distinct height, they accumulate different phases associated with their respective positions in the gravitational potential. In the traditional atomic gravimetry, the splitting of the atomic wave function appears due to the momentum transfer in a Raman transition, so that the two terms in the atomic superposition have different momentum **[19]**. Here, we study atomic gravimetry where the splitting is due to a difference in acceleration.

Consider an atom prepared in the state $|F, m_F\rangle$. Application of a resonant microwave pulse drives a hyperfine transition, producing a coherent superposition of $|F, m_F\rangle$ and $|F', m'_F\rangle$. When immersed in a magnetic field gradient oriented along z, each component of this superposition is subject to a state-dependent force arising from its magnetic dipole moment, superimposed on the common gravitational acceleration g **[20]**. They separate vertically and a gravitational relative phase appears in the superposition in a similar way to traditional atomic gravimetry. Additional pulses bring the two parts back together and a final pulse makes them interfere. The value of g can be extracted from the measurement with the advantage that counter-propagating Raman beams are not needed in contrast with traditional atomic gravimetry and that the phase scales with the interrogation time as T^3 instead of T^2. For this reason, this magnetic gravimetry is better known as T^3-gravimetry in the literature.

1.3 Semi-classical treatment

Prior to developing a full quantum-mechanical treatment, it is instructive to examine the problem from a semi-classical perspective in order to build physical intuition. Consider a magnetic field of the form

$$\mathbf{B} = \eta z \hat{\mathbf{z}}, \tag{1}$$

with η the magnetic field gradient in the z direction. Let's consider transitions between two different hyperfine levels $|F, m_F\rangle$ and $|F', m'_F\rangle$. The only requirement is that at least one of the levels has to be sensible to the magnetic field and that the response of each level to the magnetic field has to be different[2]. We can take for example two hyperfine levels in the ground state of an alkali atom. We consider low magnetic fields so the Zeeman effect is linear. The vertical acceleration due to the magnetic gradient force (F) is

$$a_C = \frac{F}{m} = \frac{\mu_B g_F m_F \eta}{m}, \tag{2}$$

with μ_B the Bohr magneton and g_F the g factor. The total acceleration for the above states is

[1] with the help and collaboration of Eduardo Gomez and Luis Castanos.

[2] For a phase signal linearly proportional to g, we will require the two levels to have an opposite magnetic response as will be shown in a moment.

$$a_+ = g + a_{C_e},$$
$$a_- = g + a_{C_g}, \tag{3}$$

where $a_{C_e}(a_{C_g})$ is the acceleration in the first(second) level.

1.3.1 Sequence of pulses

Treating each pulse as instantaneous, attention is directed to the free-evolution intervals between them. The differential acceleration experienced by the two internal states causes a progressive spatial separation of the superposition components. In a Mach-Zehnder atomic interferometer, a sequence of $\pi/2 - \pi - \pi/2$ pulses splits the wave function, inverts the velocities to recombine the two paths, and makes them interfere. The magnetic gravimeter requires a slightly more complicated pulse sequence. In order to close the interferometer and observe fringes, we need the atoms to end up at the same height and with the same velocity right at the last $\pi/2$ pulse. This is achieved with a sequence of $\pi/2 - \pi - \pi - \pi/2$ pulses separated by fall times T_1, T_2 and T_3.

1.3.1.1 Sequence $\frac{\pi}{2} - \pi - \frac{\pi}{2}$

Let's study the sequence of pulses used in light-pulse atom interferometers to see if it can be used to close the interferometer in the case of magnetic gravimetry. Suppose that each state in the superposition follows a classical trajectory (path 1 and path 2). If both states have the same initial position z_0 and initial velocity v_0, then, its final position will be different due to the different acceleration experienced by each one. The final velocity for each path is given by

$$v_1 = v_0 + a_+T_1 + a_-T_2, \tag{4}$$
$$v_2 = v_0 + a_-T_1 + a_+T_2, \tag{5}$$

where T_1 is the time elapsed between the first $\frac{\pi}{2}$-pulse and the π-pulse, and T_2 is the time elapsed between the π-pulse and the second $\frac{\pi}{2}$ pulse. On the other hand, the final position for each state is given by the classical equation of motion

$$z_1 = (z_0 + v_0T_1 + \frac{a_+T_1^2}{2}) + (v_0 + a_+T_1)T_2 + \frac{a_-T_2^2}{2}, \tag{6}$$
$$z_2 = (z_0 + v_0T_1 + \frac{a_-T_1^2}{2}) + (v_0 + a_-T_1)T_2 + \frac{a_+T_2^2}{2}, \tag{7}$$

by using Eqs. 4-5, and by demanding that the final velocities must be equal, we get that in order to produce interference, the acceleration a_+ must equal a_- or alternatively, T_1 must equal T_2. Since, by assumption, a_+ and a_- cannot be the same (because this would not split the spatial wave function), then, the only acceptable condition is $T_1 = T_2$. By accepting this condition on the duration of the pulses, and by using Eqs. 6-7 to demand that the final positions must be the same, we recover the unacceptable condition $a_+ = a_-$. Therefore, we cannot close the proposed interferometer by applying just one π-pulse between the $\frac{\pi}{2}$ pulses.

1.3.1.2 Sequence $\frac{\pi}{2} - \pi - \pi - \frac{\pi}{2}$

Let's study the sequence of pulses with an extra π-pulse before the last $\frac{\pi}{2}$-pulse. In this case, the equations for the final velocities are

$$v_1 = v_0 + a_+T_1 + a_-T_2 + a_+T_3, \tag{8}$$
$$v_2 = v_0 + a_-T_1 + a_+T_2 + a_-T_3, \tag{9}$$

where T_3 is the time elapsed between the second π-pulse and the second $\frac{\pi}{2}$-pulse. Likewise, the equations for the final positions are

$$z_1 = [(z_0 + v_0T_1 + \frac{a_+T_1^2}{2}) + (v_0 + a_+T_1)T_2 + \frac{a_-T_2^2}{2}] + (v_0 + a_+T_1 + a_-T_2)T_3 + \frac{a_+T_3^2}{2}, \tag{10}$$

$$z_2 = [(z_0 + v_0 T_1 + \frac{a_- T_1^2}{2}) + (v_0 + a_- T_1) T_2 + \frac{a_+ T_2^2}{2}] + (v_0 + a_- T_1 + a_+ T_2) T_3 + \frac{a_- T_3^2}{2}. \quad (11)$$

By using Eqs. 8 and 9, we get an equation that relates the periods between pulses as

$$T_a = 1 + T_b, \quad (12)$$

where we have defined $T_a \equiv \frac{T_2}{T_1}$ and $T_b \equiv \frac{T_3}{T_1}$. Now, by using Eqs. 10, 11, and 12, we get the condition for the times elapsed between each pulse,

$$\begin{aligned} T_2 &= 2T_1, \\ T_1 &= T_3. \end{aligned} \quad (13)$$

These equations hold independently of the values for a_+ and a_-, as can be shown by substituting them into Eqs. 8 and 9. Therefore, the sequence of pulses required to close the interferometer is

$$\pi/2 \xrightarrow{T} \pi \xrightarrow{2T} \pi \xrightarrow{T} \pi/2. \quad (14)$$

This sequence holds even in a quantum description as will be shown later. Figure 1 shows the velocity and position of the two paths under the sequence of Eq. 14. After the first $\frac{\pi}{2}$-pulse is applied, a superposition of states is created, in the semi-classical picture described above, each state moves independently and with a different acceleration dependent on the hyperfine level under consideration and the magnitude of the gradient field at the position where the state is located. Every time that a π-pulse is applied, the velocity of each state changes. Interestingly, the position curves never cross each other during the lifetime of the superposition, unlike the velocity curves which cross each other once. One of the paths (blue solid line) remains at a higher position during all the fall time. This height difference is what introduces the relative phase in the superposition that contains the gravitational acceleration.

1.3.2 Calculation of the phase signal

Now that we have settled down the sequence of pulses needed to close the interferometer and produce interference, we are in a position to compute the expected signal for gravimetry. In the semi-classical picture, each state of the superposition follows a different path and consequently accumulates a different phase. Therefore, to obtain the gravimetry signal, we need to compute the phase accumulated by each state during the lifetime of the superposition and then compute the difference between these two phases. We compare the phase difference resulting solely from propagation[3] and caused by the splitting of the spatial wave function for each state. This splitting may be caused by state-dependent differences in the position, velocity (as in the case of light-pulse atom interferometers), or acceleration (as in the case of magnetic gravimetry) for the states in the superposition. The phase of each path can be computed from [**21**]

$$\Phi_i = \frac{1}{\hbar} \int_0^t (L_c - E_i) dt', \quad (15)$$

where L_c is the classical Lagrangian evaluated along the classical trajectory of the i-th path and E_i is the internal atomic energy of the atom.

Let's compute the phase difference for each of the different types of splittings described above. We suppose that all the cases begin with the atom in a single state right before the splitting. In a position splitting the atom is separated instantaneously by a distance $\Delta d = z_2 - z_1$ which remains constant since the initial velocities and accelerations are the same for both states. This case would need an instantaneous recombination at the end to obtain the interference making it difficult to implement since the position splitting (or recombination) is never instantaneous [**22**], and the potential required to do so introduces additional complications such as decoherence due to the shift operation in position [**23**]. For this reason, traditional atomic gravimeters, rely on velocity splitting [**17**] where one path has a velocity v_0 and the other $v_0 + 2\hbar k/m$ right after the first $\pi/2$ Raman pulse. The interferometer is closed by adding a π and a $\pi/2$ pulses. In this case, the separation grows (decreases) linearly in time for the first

[3]We can neglect the phase due to a difference in separation of the wave packets at the end of the interferometer since we are considering an interferometer closed in position. Additionally, we are disregarding the phase accumulation resulting from the interaction with the microwaves, as the change in momentum is negligible.

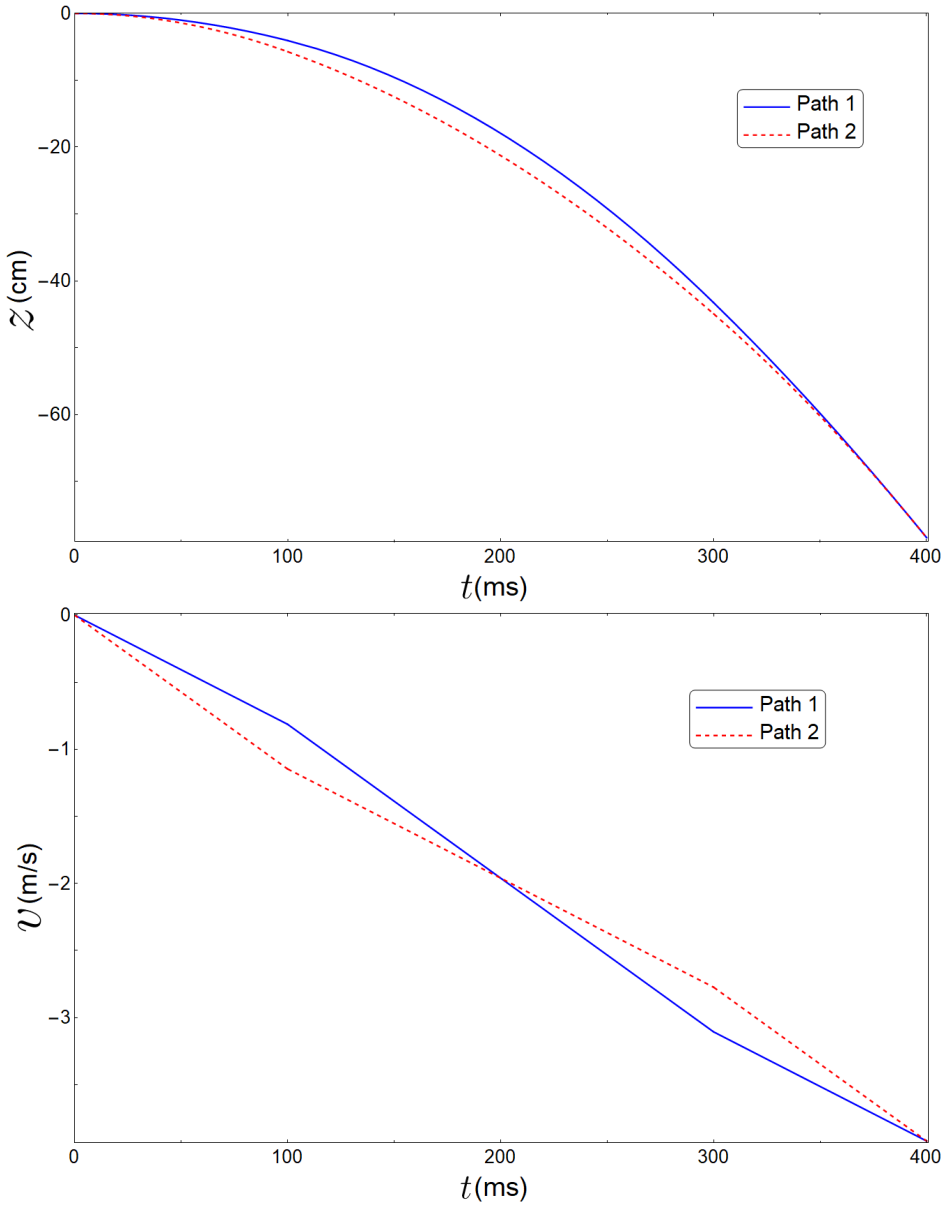

Figure 1: Position and velocity as a function of time for the two paths (blue solid and red dashed lines). We used ^{87}Rb atoms, a gradient of $\eta = 0.05$ T/m, $T = 100$ ms, $m_F = m'_F = 1$ and $g_F = \pm 1/2$ for the two levels respectively.

(second) half. On the other hand, having an acceleration splitting instead gives a separation that grows (and decreases later on) quadratically with time. The comparison of the precession of the magnetic moment in the magnetic field gradient for the two trajectories is what encodes the information about gravitational acceleration.

From Eq. 15, the phase for the splitting due to acceleration for each path turns out to be given by[4]

$$\Phi_i = \frac{m}{\hbar}\int_0^t \left(\frac{1}{2}v_i^2(t') - a_{\pm}z_i(t') - E_i/m\right)dt', \tag{16}$$

by using the semi-classical equations of motion to solve the above integral for each interval in the sequence of pulses (Eq. 14), the phase difference between both paths becomes

$$\Delta\Phi = \Phi_2 - \Phi_1 = 3\frac{m}{\hbar}(a_{C_e} - a_{C_g})\big(a_{C_e} + a_{C_g} + 2g\big)T^3. \tag{17}$$

This semi-classical result that we have derived is the same as the formula originally obtained for the T^3-interferometer of Ref. **[24]** (except for a factor of 3) but was derived with much less effort. Additionally, this result is equivalent to the phase observed in the T^3 Stern Gerlach matter wave interferometer which was proposed in Ref. **[25]** when the delay time is set to zero (up to a constant factor in front of the magnetic gradient). The main difference between both interferometers lies in the method of producing the changes in magnetic acceleration. While the magnetic interferometer proposed here and that of Ref. **[24]** achieve changes in magnetic acceleration by changing the internal state of the atom while the magnetic gradient is kept constant in time, the SG interferometer achieves the same by using magnetic pulses that change the direction of the magnetic gradient directly without having to change the internal state of the atom. As a result, the path followed by the arms of both interferometers is the same. It is important to remark that the precision of the magnetic interferometer is not limited by the delay time imposed by electronic circuits as it is in the SG interferometer. Instead, the precision of the magnetic interferometer is primarily determined by the power of the microwaves used to change the internal state of the atom, as will be discussed later.

We can gain more insight by considering states with an opposite magnetic response, for example, the stretched states of the ^{87}Rb atom ($g_{F_{g,e}} = 1/2$ and $m_{F_{g,e}} = \mp 2$). In this case, the phase difference is linearly proportional to g, i.e.,

$$\Delta\Phi_s = 12\frac{\mu_B\eta}{\hbar}gT^3, \tag{18}$$

where the subscript indicates that this is the total phase difference when considering the transition between the stretched states. We can compare this result with the signal measured in traditional gravimetry that uses stimulated Raman transitions to induce state transitions and changes in momentum **[17]**

$$\Delta\Phi = k_{eff}gT^2, \tag{19}$$

where $\hbar k_{eff}$ is the effective momentum gained by the atom after the Raman transition has finished.

Following the same procedure used above, we can derive the phase signal for the rest of the types of splitting, including that of the light-pulse atom gravimetry (Eq. 19). Table 1 gives the phase difference ($\Delta\Phi = \Phi_2 - \Phi_1$) for the case of splitting in position, velocity, or acceleration in terms of the total time (T_t) of the sequence. The sequence requires an extra π pulse as one moves from position to velocity splitting, or from velocity to acceleration. The phase difference grows as a linear, quadratic, and cubic function of time respectively, and is proportional to the quantity responsible for the splitting. Figure 2 shows a comparison of the phase difference for the three cases as a function of the total time T_t. The acceleration splitting gives a bigger phase difference for a relatively short time (T_t) compared to the other methods. In the case of the magnetic gravimeter, T_t depends on experimental parameters such as the magnetic field gradient η, and at fall times slightly below 1 s, one already gets a reasonable phase difference.

[4]We are considering a static reference frame. In this reference frame, the integral of the Lagrangian does not vanish as is the case of a reference frame that follows the atom. When using a reference frame that follows the atom, a new term that can be interpreted as the phase printed by the light on the atom arises (see for example Ref. **[17]**).

Table 1: Comparison of the phase difference with splitting by position, velocity, and acceleration. We suppose that the internal atomic energy of the atom in Eq. 15 is the same for both paths in the case of position splitting. Note that in a splitting due to differences in velocity or acceleration, the internal energy of the atom does not contribute to the phase difference since the corresponding term in the integral does not change with time and there is a change of sign due to the π-pulse(s) that cancels out the contribution for each path.

Splitting by	Position	Velocity	Acceleration
Separated by	$\Delta d = z_2 - z_1$	$\Delta v = v_2 - v_1$	$\Delta a = a_2 - a_1$, $(a_1 = -a_2)$
Sequence	$\pi/2 \xrightarrow{T} \pi/2$	$\pi/2 \xrightarrow{T} \pi \xrightarrow{T} \pi/2$	$\pi/2 \xrightarrow{T} \pi \xrightarrow{2T} \pi \xrightarrow{T} \pi/2$
Total time T_t	$T_t = T$	$T_t = 2T$	$T_t = 4T$
Phase difference $\Delta\Phi$	$\left(\frac{mg}{\hbar}\right) \Delta d T_t$	$2\left(\frac{mg}{\hbar}\right) \Delta v T_t^2$	$6(\frac{mg}{\hbar})\Delta a T_t^3$

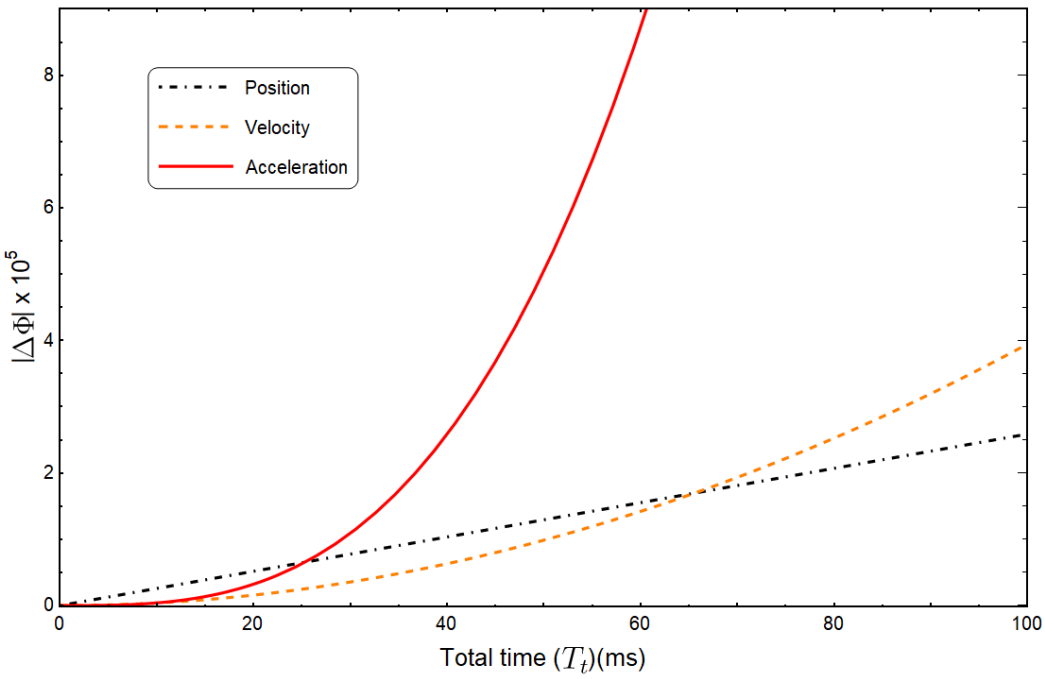

Figure 2: Comparison of the phase acquired for a gravimeter separated by position (black dotted dashed line), velocity (orange dashed line), or acceleration (red solid line) as a function of the total time (T_t). We used ^{87}Rb with $\Delta d = 200$ μm; $\Delta k = 2\pi/780$ nm; $\eta = 0.05$ T/m, $g_{F_{g,e}} = 1/2$ and $m_{F_{g,e}} = \mp 2$.

1.4 Quantum treatment

The calculations above considered a semi-classical picture to represent the superposition of states. Nevertheless, a correct calculation of the interferometer phase demands solving the evolution of each state using a quantum mechanical approach. A solution using time-evolution operators can be found in Ref. [**24**]. However, our calculation follows a different approach. Consider an alkali-metal atom with quantized center-of-mass motion along the z-axis, subject to a constant gravitational field and interacting with a classical magnetic field of the form given by Eq. 1 and subject to microwave excitations ($\mathbf{B}_p$) that propagate along the x-axis with polarization along the $\hat{\mathbf{q}}$-direction. Note that $\mathbf{B}_p$ is only used to control the internal state of the atom, so its polarization can be chosen in any convenient direction. We focus on the z-axis movement of the atom since the transverse (x and y) directions give a free evolution. The resulting Hamiltonian is [**20**]

$$H(t) = \frac{1}{2m}P_z^2 + mgZ + H_A - \boldsymbol{\mu}\cdot[\eta Z\hat{\mathbf{z}} + \mathbf{B}_p(t)], \tag{20}$$

where H_A is the atomic structure Hamiltonian and $\boldsymbol{\mu}$ is the magnetic dipole moment operator of the atom. The solution to this Hamiltonian, in momentum space, for the stretched states ($g_{F_{g,e}} = 1/2$ and $m_{F_{g,e}} = \mp 2$) of the ^{87}Rb atom was calculated in Ref. [**20**] and is given by

$$\widehat{\phi}(k,\tau) = \widehat{\phi}(k + q_2\tau, 0)\exp\left[-iq_1\tau + i\frac{\epsilon}{3q_2}k^3 - i\frac{\epsilon}{3q_2}(k+q_2\tau)^3\right], \tag{21}$$

where k is the momentum of the state and ϵ is given by

$$\epsilon = \frac{\hbar\kappa^2}{2M\Delta W}, \tag{22}$$

where M is the mass of the atom. Also, we have defined

$$q_1 = \frac{1}{2}, \quad q_2 = \left(\frac{Mg}{\hbar\Delta W\kappa} \pm \gamma_1\right), \tag{23}$$

where g_0 is the acceleration of gravity and

$$\gamma_1 = \frac{g_s - 2Ig_n\frac{m_e}{m_p}}{2(g_s + g_n\frac{m_e}{m_p})}, \tag{24}$$

where m_e and m_p are the electron mass and the proton mass respectively and I is the nuclear spin. Finally, we have defined the inverse of the characteristic length of the system as

$$\kappa \equiv (g_s\frac{\mu_B}{\hbar} + g_n\frac{\mu_n}{\hbar})\frac{\eta}{\Delta W} > 0, \tag{25}$$

where g_s is the electron spin g-factor, g_n is the nuclear g-factor, μ_B is the Bohr magneton, μ_n is the nuclear magneton, $\hbar\Delta W$ is the field-free ground-state hyperfine splitting energy, η is the proportionality constant of the magnetic field (Eq. 1), and $\tau \equiv \Delta W t$ is the non-dimensional time.

Equation 21 gives the evolution of the state (subject to Eq. 20) recursively. In particular, it gives the evolution before the pulse ($\mathbf{B}_p(t) = 0$). Now, using this solution for our calculation, we consider the same sequence of pulses as before (Eq. 14). The state at the end of the first interval will be given by

$$\widehat{\phi}_\pm(k,\tau) = \widehat{\phi}_\pm(k + q_{2_\pm}\tau, 0)\exp\left[-iq_1\tau + i\frac{\epsilon}{3q_{2_\pm}}k^3 - i\frac{\epsilon}{3q_{2_\pm}}(k+q_{2_\pm}\tau)^3\right], \tag{26}$$

where the subscript $\pm$ denotes the choice of either a plus or minus sign preceding γ_1 in the definition of q_2 (Eq. 23), i.e., it specifies the state under consideration. At the end of the second interval, the state will be given by

$$\widehat{\phi}_\pm(k,\tau+2\tau) = \widehat{\phi}_\pm(k + 2q_{2_\mp}\tau, \tau)\exp\left[-2iq_1\tau + i\frac{\epsilon}{3q_{2_\mp}}k^3 - i\frac{\epsilon}{3q_{2_\mp}}(k+2q_{2_\mp}\tau)^3\right], \tag{27}$$

and at the end of the last interval, the state will be given by

$$\widehat{\phi}_{\pm}(k,\tau+2\tau+\tau)=\widehat{\phi}_{\pm}(k+q_{2_{\pm}}\tau,\tau+2\tau)\exp\left[-iq_1\tau+i\frac{\epsilon}{3q_{2_{\pm}}}k^3-i\frac{\epsilon}{3q_{2_{\pm}}}(k+q_{2_{\pm}}\tau)^3\right]. \quad (28)$$

We can substitute Eq. 27 into Eq. 28 to get

$$\begin{aligned}\widehat{\phi}_{\pm}(k,\tau+2\tau+\tau)=\widehat{\phi}_{\pm}(k+q_{2_{\pm}}\tau+2q_{2_{\mp}}\tau,\tau)\\ \exp\left[-2iq_1\tau+i\frac{\epsilon}{3q_{2_{\mp}}}(k+q_{2_{\pm}}\tau)^3-i\frac{\epsilon}{3q_{2_{\mp}}}((k+q_{2_{\pm}}\tau)+2q_{2_{\mp}}\tau)^3\right]\\ \exp\left[-iq_1\tau+i\frac{\epsilon}{3q_{2_{\pm}}}k^3-i\frac{\epsilon}{3q_{2_{\pm}}}(k+q_{2_{\pm}}\tau)^3\right]. \quad (29)\end{aligned}$$

Similarly, we can substitute Eq. 26 into the last equation to get

$$\begin{aligned}\widehat{\phi}_{\pm}(k,\tau+2\tau+\tau)=\widehat{\phi}_{\pm}(k+q_{2_{\pm}}\tau+2q_{2_{\mp}}\tau+q_{2_{\pm}}\tau,0)\\ \exp\left[-iq_1\tau+i\frac{\epsilon}{3q_{2_{\pm}}}(k+q_{2_{\pm}}\tau+2q_{2_{\mp}}\tau)^3-i\frac{\epsilon}{3q_{2_{\pm}}}((k+q_{2_{\pm}}\tau+2q_{2_{\mp}}\tau)+q_{2_{\pm}}\tau)^3\right]\\ \exp\left[-2iq_1\tau+i\frac{\epsilon}{3q_{2_{\mp}}}(k+q_{2_{\pm}}\tau)^3-i\frac{\epsilon}{3q_{2_{\mp}}}((k+q_{2_{\pm}}\tau)+2q_{2_{\mp}}\tau)^3\right]\\ \exp\left[-iq_1\tau+i\frac{\epsilon}{3q_{2_{\pm}}}k^3-i\frac{\epsilon}{3q_{2_{\pm}}}(k+q_{2_{\pm}}\tau)^3\right]. \quad (30)\end{aligned}$$

This equation describes each of the two states of the superposition at the end of the last interval and can be used to compute the total phase difference between them. Note that the first term on the right side of this equation can be interpreted as a wave packet that has not evolved in time and in consequence, it does not contribute to the phase difference. For this reason, the phase gained for each state will be given by

$$\begin{aligned}\widehat{\varphi}_{\pm}(k)=-4q_1\tau\\ +\frac{\epsilon}{3q_{2_{\pm}}}\left[(k+q_{2_{\pm}}\tau+2q_{2_{\mp}}\tau)^3-((k+q_{2_{\pm}}\tau+2q_{2_{\mp}}\tau)+q_{2_{\pm}}\tau)^3+k^3-(k+q_{2_{\pm}}\tau)^3\right]\\ +\frac{\epsilon}{3q_{2_{\mp}}}\left[(k+q_{2_{\pm}}\tau)^3-((k+q_{2_{\pm}}\tau)+2q_{2_{\mp}}\tau)^3\right]. \quad (31)\end{aligned}$$

Thereby, the total phase difference between both states when the last $\frac{\pi}{2}$-pulse is applied will be given by

$$\Delta\Phi=\widehat{\varphi}_{+}(k)-\widehat{\varphi}_{-}(k)=2\left[(q_{2_{+}})^2-(q_{2_{-}})^2\right]\epsilon\tau^3. \quad (32)$$

We can gain more insight into this result by substituting the definition of the non-dimensional parameters and using an approximation for the κ and γ_1 parameters defined in Eqs. 24 and 25 as follows. The Bohr magneton and the nuclear magneton are defined as

$$\mu_B=\frac{\hbar e}{2m_e},\quad \mu_n=\frac{\hbar e}{2m_p}, \quad (33)$$

where m_e and m_p are the electron and proton mass respectively. However, the proton mass is several orders of magnitude larger than the electron mass, therefore, we can use the following approximation

$$\kappa\approx g_s\frac{\mu_B}{\hbar}\frac{\eta}{\Delta W}. \quad (34)$$

Additionally, since we are considering the alkali atom of ^{87}Rb, we have the following values for this atom **[26, 27]**

$$g_s \approx 2.002, \quad g_n \frac{m_e}{m_p} \approx 0.001, \quad I = \frac{3}{2}. \tag{35}$$

As a result, we can also use the following approximation

$$\gamma_1 \approx 1/2. \tag{36}$$

Thus, by using the definitions in Eqs. 22-23 and the above approximations (Eqs. 34 and 36), we get the total phase difference

$$\Delta\Phi = 4\frac{\mu_B \eta}{\hbar} g \left(\frac{\tau}{\Delta W} \right)^3 = 4\frac{\mu_B \eta}{\hbar} g t^3, \tag{37}$$

where we have used $\tau \equiv \Delta W t$. Notice that, as expected, the result of our calculation is the same as that obtained following a semi-classical approach (Eq. 18) except for a factor of 3 (see discussion following Eq. 17). Therefore, the result in Eq. 37 coincides with and is a particular case of the general solution demonstrated in Ref. **[24]**

$$\Delta\Phi = \frac{m}{\hbar}(a_{C_e} - a_{C_g})\big(a_{C_e} + a_{C_g} + 2g\big)T^3. \tag{38}$$

1.5 Detuning of the transitions due to the Zeeman effect

Equation 37 establishes that the value of g can be extracted from the measured phase difference at the output port of the interferometer. Under ideal conditions, the pulse sequence of Eq. 14 would be implemented with precisely tuned Rabi frequencies to drive the target transitions resonantly. However, even if we started with the correct frequency, there is a position-dependent detuning that has to be taken into account when the atoms exist in free fall. To see why, remember that the experiment takes place inside a magnetic field gradient on the z-axis of the form given by Eq. 1 and consider transitions between two hyperfine state levels of the atom with a different magnetic quantum number

$$\begin{aligned} |g\rangle &= |F_g, m_{F,g}\rangle\,, \\ |e\rangle &= |F_e, m_{F,e}\rangle\,, \end{aligned} \tag{39}$$

where $m_{F,e}(m_{F,g})$ is the magnetic quantum number of the excited(ground) state, and $F_g(F_e)$ is the total angular momentum of the excited(ground) state. The transitions in this two-level system are characterized by a frequency ω_{21}, i.e.,

$$\omega_{21} = \frac{E_e - E_g}{\hbar}. \tag{40}$$

Since the atom is placed inside this external magnetic field, its energy levels will be split according to the (linear) Zeeman effect, i.e.,

$$\Delta E = \mu_B g_F m_F B, \tag{41}$$

where μ_B is the Bohr magneton and g_F is the Landé g_F-factor. Moreover, due to the linear dependence of the magnetic field with the position, the Zeeman split will depend on the position as well, i.e.,

$$\Delta E(z) = \mu_B g_F m_F \eta z. \tag{42}$$

This change in the energy due to the Zeeman effect can be translated into a change in the corresponding frequency of the energy level with the magnetic number m_F through the Planck relation, i.e.,

$$\Delta\omega(z, g_F, m_F) = \frac{\mu_B g_F m_F \eta}{\hbar} z. \tag{43}$$

We suppose that the wave packet describing the atom is initially located at z_0 where the magnetic field is B_0, and induce Rabi transitions between our two states by applying a perturbation with a frequency-tuned with the transition that interests us. Then, both levels will suffer a shift, so the new transition frequency will be given by

$$\omega'_{21} = \omega_{21} + \Delta\omega(z_0, g_{F_e}, m_{F_e}) - \Delta\omega(z_0, g_{F_g}, m_{F_g}) = \omega_{21} + \frac{\mu_B g_{F_{eff}} m_{F_{eff}} \eta}{\hbar} z_0, \tag{44}$$

where we have defined an effective product between the quantum magnetic numbers and the Landé g_F-factors as

$$g_{F_{eff}} m_{F_{eff}} \equiv g_{F_e} m_{F_e} - g_{F_g} m_{F_g}. \tag{45}$$

Hence, the detuning of the Rabi oscillations when the atom is at z will be given by

$$\delta(z) = \omega_B - \omega'_{21} = \frac{\mu_B g_{F_{eff}} m_{F_{eff}} \eta}{\hbar}(z - z_0). \tag{46}$$

1.6 The warning width

It turns out that this detuning in Eq. 46 sets a constraint in the width, in position space, that the atom's wave function can have to have resonant transitions. To determine this warning width, we recall that the probability of finding the atom in the excited state at time t when it was initially in the ground state at $t = 0$ is given by **[28]**

$$|c_e(t)|^2 = \frac{\Omega^2}{\tilde{\Omega}^2} \sin^2\left[\frac{\tilde{\Omega} t}{2}\right], \tag{47}$$

where $\tilde{\Omega}$ is defined in terms of the Rabi flopping frequency Ω and the detuning δ[5], i.e.,

$$\tilde{\Omega} = \sqrt{\delta^2 + \Omega^2}. \tag{48}$$

Now, consider the point where a π-pulse results in no transfer of population, i.e.,

$$\sqrt{\left[\delta(z)\right]^2 + \Omega^2}\left(\frac{t}{2}\right) = \pi, \tag{49}$$

from which we get

$$\delta(z) = \frac{\sqrt{4\pi^2 - \Omega^2 t^2}}{t}. \tag{50}$$

Using the above result and Eq. 45, we get

$$\Delta Z = \frac{\sqrt{4\pi^2 - \Omega^2 t^2}}{t} \frac{\hbar}{\mu_B g_{F_{eff}} m_{F_{eff}} \eta}. \tag{51}$$

For experimental purposes, we would like to have Ω fixed. Therefore, the width will be fixed by t. For example, if we use a π-pulse, i.e., $t = \pi/\Omega$. Then, the warning width will be given by

$$\Delta Z = \pi\sqrt{3}\Omega \frac{\hbar}{\mu_B g_{F_{eff}} m_{F_{eff}} \eta}. \tag{52}$$

Thus, to stay in resonance during the application of the Rabi pulses, the width of the atom's wave function in position space must remain smaller than the width given by Eq. 52.

Finally, notice that usually the electric field dominates since it is several orders of magnitude larger than the magnetic field so the Rabi flopping frequency is usually taken to be

$$\Omega = \frac{-eE_0 \langle e| r |g\rangle}{\hbar},$$

where r is the position operator in the direction of the polarization of the electric field, E_0 is the amplitude of the electric field, and e is the electron charge. Nonetheless, for an alkali atom inside a magnetic field gradient, the transitions are driven by the magnetic field of the microwaves and not by the electric field. This is because we will only consider transitions between hyperfine sub-levels in the

[5]Other references name $\tilde{\Omega}$ as the Rabi flopping frequency instead of Ω. In any case, notice that $\tilde{\Omega}$ is the parameter that contains the information about the transition frequency while Ω only contains the information about the strength of the electromagnetic field.

ground state $5^2S_{1/2}$ of ^{87}Rb [**20**] for which the dipole matrix elements are zero due to selection rules [**29**]. Therefore, the Rabi flopping frequency will depend solely on the magnetic field, i.e.,[6]

$$\Omega = \frac{-B_0 \langle e| \mu |g\rangle}{\hbar}, \tag{53}$$

where μ is the total magnetic moment operator in the direction of the polarization of the magnetic field, B_0 is the amplitude of the magnetic field $\mathbf{B}$ which in the case of a monochromatic polarized microwave can be written in the generic form

$$\mathbf{B} = B_0 \cos(\omega t)\hat{\boldsymbol{e}}, \tag{54}$$

where we have ignored the spatial variation due to the dimensions of the atom. Thereby, the amplitude of the magnetic field will set the warning width. The more intense the magnetic field, the larger the warning width and vice-versa.

1.7 Expansion of the atomic wave function for a pure state

As previously seen, to have resonant transitions, the width of the atom's wave function in position space has to be smaller than the warning width set by Eq. 52. Therefore, it is imperative to know what is the width of the wave packet and its expansion. In general, the expansion will depend on how the initial state was prepared and its initial width. In this section, we will consider the case of a pure state resulting from the application of a selector pulse in position space and later, we will consider the case where the expansion is described by the evolution of a thermal ensemble of atoms initially trapped in an optical dipole trap. We will begin by reviewing the time evolution of a Gaussian wave packet.

1.7.1 Time-evolution of the free wave packet

We begin by considering a superposition of plane waves with different amplitudes [**31**]

$$\Psi(z,t) = \int_{-\infty}^{\infty} dk A(k) e^{i(kz-\omega t)}, \tag{55}$$

where k is the wave number and the amplitude $A(k)$ is of the Gaussian form

$$A(k) = Ce^{-\alpha(k-k_0)^2/2}, \tag{56}$$

where k_0 is the center of the distribution, C is a scale factor that we can use to normalize the wave packet, and α is a parameter that defines the initial width of the wave packet as we will see in a moment. To compute the integral in Eq. 55, we need to establish the dependence between ω and k, i.e., the dispersion relation. We will consider the dispersion relation to be sharply peaked about $k = k_0$ and use a Taylor expansion about this point to second order, i.e.,

$$\omega(k) = \omega_0 + (k-k_0)v_g + \frac{1}{2}(k-k_0)^2\beta, \tag{57}$$

where $\omega_0 = \omega(k_0)$, and v_g is the group velocity defined as

$$v_g \equiv \left(\frac{\partial\omega(k)}{\partial k}\right)_{k=k_0}, \tag{58}$$

and β is given by

$$\beta \equiv \left(\frac{\partial^2\omega(k)}{\partial k^2}\right)_{k=k_0}. \tag{59}$$

Now, we can substitute Eqs. 56-57 into Eq. 55 and workout the integral. Then, the wave packet in position space, normalized and initially centered around z_0, is given by

[6] This is the paramagnetic contribution to the magnetic moment of the atom and is valid for weak magnetic fields. In general, there is another quadratic contribution called the diamagnetic moment of the atom which is very small [**30**].

$$\Psi(z,t)=\left(\frac{\sqrt{\alpha}}{2\pi^{3/2}}\right)^{1/2}\sqrt{\frac{2\pi}{\alpha+i\beta t}}\exp\left[\frac{i}{2}\frac{(z-z_0-v_g t)^2}{\beta t-i\alpha}\right]\exp[i(k_0(z-z_0)-\omega_0 t)]. \tag{60}$$

We can cast the above equation into a more illuminating form by putting the complex factors in the denominators in the standard form ($Z=[\Re(Z)+i\Im(Z)]$), and by using the de Moivre's theorem to compute the required squared root. In this way, we obtain the expansion of the free Gaussian wave packet as follows

$$\Psi(z,t)=(2\pi)^{-1/4}\left(\frac{\alpha^2+\beta^2t^2}{2\alpha}\right)^{-1/4}\exp\left[-\frac{1}{4}\frac{(z-z_0-v_g t)^2}{(\alpha^2+\beta^2t^2)/(2\alpha)}\right]$$
$$\exp\left[i\left(k_0(z-z_0)-w_0t+\frac{\beta t}{2}\frac{(z-z_0-v_g t)^2}{\alpha^2+\beta^2t^2}-\frac{1}{2}\arctan\left[\frac{\beta t}{\alpha}\right]\right)\right]. \tag{61}$$

If we re-accommodate terms, we can write the equation describing the evolution of the normalized free wave packet as

$$\Psi(z,t)=\left[\frac{1}{2\pi\big(\sigma_z(t)\big)^2}\right]^{1/4}\exp\left[-\frac{1}{4}\frac{\big(z-z_0-v_g t\big)^2}{\big(\sigma_z(t)\big)^2}\right]\exp\left[-\frac{i}{2}\arctan\left(\frac{\beta t}{2\big(\sigma_z(0)\big)^2}\right)\right]$$
$$\exp\left[i\left(k_0(z-z_0)-w_0t+\frac{\big[(z-z_0)^2+2z_0v_g t\big]}{4[\sigma_z(t)\sigma_z(0)]^2}\frac{\beta t}{2}+\frac{v_g t(v_g t-2z)}{4[\sigma_z(t)\sigma_z(0)]^2}\frac{\beta t}{2}\right)\right], \tag{62}$$

where the width of the wave packet is given by

$$\sigma_z(t)=\sqrt{\frac{\alpha^2+\beta^2t^2}{2\alpha}}. \tag{63}$$

Thereby, the initial width of the free wave packet is given by

$$\sigma_z(0)=\sqrt{\alpha/2}. \tag{64}$$

Hence, the expansion of the free wave packet is described by

$$\sigma_z(t)=\sqrt{[\sigma_z(0)]^2+\left[\frac{\beta t}{2\sigma_z(0)}\right]^2}. \tag{65}$$

1.7.2 Initialization of the free wave packet

Notice that we can take advantage of the result in Eq. 52 to perform a measurement in position space and discard the atoms that did not end up in the desired final state because the width of its wave function was larger than ΔZ, so we end up with a cloud of atoms with a definite uncertainty (width) in position space. We can use this selector pulse to set the initial width of the atom's wave function in position space. This approach only works if the initial width of the atom's wave packet is larger than the warning width set according to Eq. 51. The application of this selector pulse results approximately in a pure state (for the external degrees of freedom) described by a Gaussian wave packet of the form given by Eq. 62 with its expansion described by Eq. 65. Notice that if the initial width is too small, the wave packet will expand quickly and the detuning will begin to be a problem. On the other hand, if the initial width is too large, the expansion time will be short. It seems that there should exist a sweet spot where the initial width is not too small or too big. Thus, we need to try to optimize Eq. 65. As mentioned earlier, the maximum Rabi frequency that can be obtained in the laboratory will usually set the final width that can be used to drive the transitions, thus, it makes sense to set the final width as a constant in Eq. 65 and find out the initial width that maximizes the time needed to reach the final width. Thereby, we re-write Eq. 65 as follows

$$t=2\frac{\sigma_{z0}}{\beta}\sqrt{(\sigma_{zf})^2-(\sigma_{z0})^2}, \tag{66}$$

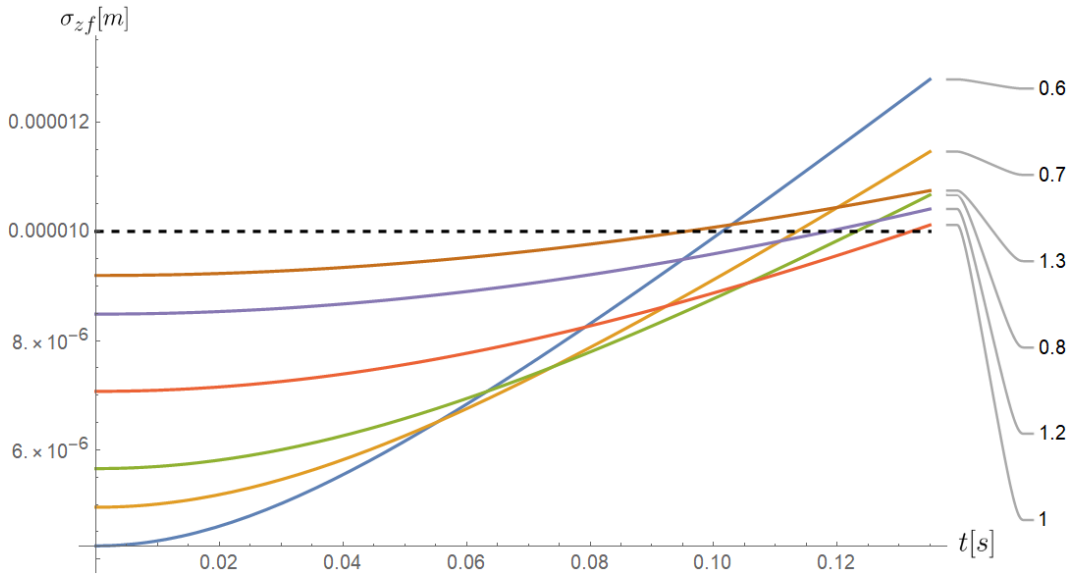

Figure 3: Maximization of the time needed to reach a given final width σ_{z0}. The initial width $(\sigma_{z0})^*$ that maximizes the time needed to reach σ_{zf} is given in Eq. 67. The numbers on the right mean: *times* $(\sigma_{z0})^*$; so 0.6 means $0.6(\sigma_{z0})^*$, 0.7 means $0.7(\sigma_{z0})^*$, and so on. The dashed line represents the desired final width σ_{zf}. This plot was generated by considering M in Eq. 68 equal to the mass of the ^{87}Rb atom.

where σ_{z0} and σ_{zf} are the initial and final width respectively. The initial width that maximizes this expression is given by

$$(\sigma_{z0})^* = \frac{\sigma_{zf}}{\sqrt{2}}. \tag{67}$$

If we substitute back this value into Eq. 66, we get the time that we can let the wave packet expand

$$t_{max} = \frac{\sigma_{zf}^2}{\beta}. \tag{68}$$

By comparing Eq. 62 and the wave function of Eq. 21 written in position space for an initial coherent state wave packet **[20]**, we get that $\beta = \hbar/M$ where M is the mass of the atom. We show in Fig. 3 the optimization of the wave packet for a given final width.

1.8 Expansion of the atomic cloud for an ensemble of atoms initially trapped in thermal equilibrium

The pure state considered in the last section, helped us to understand the general behavior of the expansion of the wave function. However, it does not take into consideration the thermal distribution of the atoms. To take into account the effect of the temperature, we need to consider the density matrix of the ensemble of atoms. Thus, in a more realistic computation, the expansion of the wave packet has to depend on both the temperature of the atomic cloud and the frequency of oscillation of the atoms in the initial trap.

1.8.1 Initial Conditions of the atomic cloud

The first step in atomic gravimetry is to trap and cool the atoms to be used. Let us assume that we use an optical dipole trap and that the atoms in this trap oscillate along the z-axis under a harmonic oscillator potential with frequency ω. Furthermore, let's suppose that we keep the atoms trapped until they reach a thermal equilibrium[7]. Afterward, we turn off the trap and let the cloud of atoms expand. After we release the atoms from the trap, every atom will have a different wave function so we will

[7]The conditions to get a thermal equilibrium will depend on the type of trap chosen.

have to rely on statistical methods to know the properties of this ensemble. In the following sections, we will give a brief review of the formalism of the density matrix and show how the density matrix for our particular case can be computed. We will suppose that the ensemble is a canonical ensemble kept at temperature T even after we release them from the trap. This is justified because the potential is turned off instantaneously so we can expect that the thermal equilibrium stands for a short period since the atoms do not have enough time to reach the walls of the system to interchange kinetic energy. Besides, we suppose that we have a dilute gas so the atoms do not interact with each other. Finally, it is important to mention that for the next results, we will consider that this ensemble follows the Boltzmann statistics. This is justified since trapping atoms by simply using an optical dipole trap is not enough to produce a Bose-Einstein condensate. To achieve the quantum regime of Bose-Einstein statistics, we would need to additionally use evaporative cooling.

1.8.2 Review of the density matrix

Statistical properties of the ensemble are most conveniently expressed through the density operator formalism. For an ensemble of non-degenerate states, the density matrix is given by

$$\rho = \sum_n w_n \left|\phi_n\right\rangle \left\langle\phi_n\right|, \tag{69}$$

where the probability w_n is normalized such that $\sum_n w_n = 1$. In the case where $|\phi_n\rangle$ are the eigenvectors of the Hamiltonian H, i.e., $H\left|\phi_n\right\rangle = E_n\left|\phi_n\right\rangle$, we have that **[28]**

$$w_n = e^{-\beta E_n}/Q, \tag{70}$$

where w_n is the probability of finding, in the ensemble, a system with energy E_n, i.e., in the state $|\phi_n\rangle$. Also, $Q = \sum_n e^{-\beta E_n}$ is the well-known partition function, and $\beta = \frac{1}{kT}$, where k is the Boltzmann constant and T is the temperature of every system in the ensemble. Therefore, we have that

$$\begin{aligned}\rho &= Q^{-1}\sum_n e^{-\beta H}\left|\phi_n\right\rangle\left\langle\phi_n\right| = Q^{-1}e^{-\beta H}\sum_n \left|\phi_n\right\rangle\left\langle\phi_n\right|, \\ &= \frac{e^{-\beta H}}{Tr(e^{-\beta H})}, \\ &= Q^{-1}e^{-\beta H}.\end{aligned} \tag{71}$$

Now, we will try to compute the density matrix by following the method described in **[32]**. Let us define the non-normalized density matrix ρ_u given by

$$\rho_u \equiv e^{-\beta H}. \tag{72}$$

If we take the derivative of this equation with respect to β, we have

$$-\frac{\partial \rho_u}{\partial \beta} = H\rho_u. \tag{73}$$

Thereby, by solving this PDF we can find find ρ_u. The initial condition needed to solve this equation is that if we take the limit $\beta \longrightarrow 0$, i.e., $T \longrightarrow \infty$, we have to recover the density matrix of a completely random ensemble, that is

$$\rho_u(0) = 1. \tag{74}$$

From now on, we will omit the sub-index and just write ρ for the non-normalized density matrix. What's more, to write the matrix elements in position space, we will use the following notation

$$\left\langle x\right|\rho\left|x'\right\rangle \equiv \rho(x, x'|\beta) = \sum_n Q^{-1}e^{\beta E_n}\phi_n(x)\phi_n^*(x'). \tag{75}$$

Therefore, in position space, Eqs. 73 and 74 have the following form

$$-\frac{\partial \rho(x, x'|\beta)}{\partial \beta} = H_x\rho(x, x'|\beta), \tag{76}$$

and

$$\rho(x, x'|0) = \delta(x - x'). \tag{77}$$

Note that H_x operates in the x-axis. Let us see how to solve these equations for different Hamiltonians.

1.8.2.1 Density matrix for a 1-D free particle Hamiltonian

Now, we will show how to solve Eqs. 76 and 77 for the case of the 1-dimensional free particle Hamiltonian, i.e.,

$$H = \frac{\hat{p}^2}{2m}, \tag{78}$$

where $\hat{p}$ is the momentum operator given by

$$\hat{p} = -i\hbar\nabla. \tag{79}$$

Therefore, the equations to solve are

$$-\frac{\partial\rho(x, x'|\beta)}{\partial\beta} = -\frac{\hbar^2}{2m}\frac{\partial^2}{\partial x^2}\rho(x, x'|\beta), \tag{80}$$

and

$$\rho(x, x'|0) = \delta(x - x'). \tag{81}$$

The solution that satisfies these equations can be easily found to be

$$\rho(x, x'|\beta) = \sqrt{\frac{m}{2\pi\hbar^2\beta}}\exp\left[-\left(\frac{m}{2\hbar^2\beta}\right)(x - x')^2\right]. \tag{82}$$

This is the equation of a normal distribution and can be written as

$$\rho(x, x'|\beta) = \frac{1}{\sigma\sqrt{2\pi}}\exp\left[-\frac{1}{2}\frac{(x - x')^2}{\sigma^2}\right], \tag{83}$$

where the standard deviation of the distribution is given by

$$\sigma = \hbar\sqrt{\frac{\beta}{m}}. \tag{84}$$

This result means that the matrix elements of the density operator in position space follow a normal distribution centered at the diagonal. Then, the diagonal elements are given by

$$\rho(x, x|\beta) = \frac{1}{\sigma\sqrt{2\pi}}. \tag{85}$$

Observe that this solution is not normalizable. This makes sense since the wave function of a free particle is not normalizable either.

1.8.2.2 Density matrix for an ensemble of free particles in a box

If we have an ensemble of free particles confined in a box, the matrix elements of the density operator are still given by Eqs. 84 and 85. However, this time the diagonal elements are normalizable. If the box (1-dimensional) has a length L, we have that the normalization constant is given by

$$\begin{aligned} N &= \int_{-L/2}^{L/2}\rho(x, x|\beta)dx, \\ &= \frac{1}{\sigma\sqrt{2\pi}}\int_{-L/2}^{L/2}dx, \\ &= \frac{L}{\sigma\sqrt{2\pi}}. \end{aligned} \tag{86}$$

1.8.3 Density matrix for an ensemble of atoms subjected to a harmonic oscillator potential

Notice that the potential in an optical dipole trap can be approximated with a harmonic oscillator **[33]**. Thus, now, we focus on solving Eqs. 76 and 77 for the case of a harmonic oscillator Hamiltonian[8], i.e.,

$$H = \frac{\hat{p}^2}{2m} + \frac{m\omega^2\hat{x}^2}{2}. \tag{87}$$

With this Hamiltonian, the equation to be solved becomes

$$-\frac{\partial\rho}{\partial\theta} = -\frac{\partial^2\rho}{\partial\xi^2} + \xi^2\rho, \tag{88}$$

where we have introduced the non-dimensional quantities

$$\xi \equiv \sqrt{\frac{m\omega}{\hbar}}x, \tag{89}$$

and

$$\theta \equiv \frac{\hbar\omega}{2}\beta. \tag{90}$$

Similarly, the initial condition can be re-written using the non-dimensional variable ξ and by using the composition property of the Dirac delta function

$$\delta[f(x)] = \sum_i \frac{1}{|f'(x_i)|}\delta(x - x_i), \tag{91}$$

where $f(x_i) = 0$ and $f'(x_i) \neq 0$. Thus, if we write

$$f(x) = \xi - \xi' = \sqrt{\frac{m\omega}{\hbar}}(x - x'), \tag{92}$$

we get

$$\delta[f(x)] = \delta(\xi - \xi') = \sqrt{\frac{\hbar}{m\omega}}\delta(x - x'), \tag{93}$$

and the initial condition can be written as

$$\rho(\xi, \xi'|0) = \sqrt{\frac{m\omega}{\hbar}}\delta(\xi - \xi'). \tag{94}$$

In order to solve Eq. 88, we will analyze the solution in the high-temperature limit, i.e., when $\theta \longrightarrow 0$. In this limit, the particles have to behave like a free particle so the solution has to be the Gaussian distribution in Eq. 83. Thus, we suppose a solution of the form

$$\rho = exp\big[-\big(a(\theta)\xi^2 + b(\theta)\xi + c(\theta)\big)\big], \tag{95}$$

where a, b, and c are parameters that depend on θ. If we differentiate this equation and substitute it back into Eq. 88, we reduce the PDE into the following system of ordinary differential equations

$$\begin{aligned} \frac{da}{d\theta} &= 1 - 4a^2, \\ \frac{db}{d\theta} &= -4ab, \\ \frac{dc}{d\theta} &= 2a - b^2. \end{aligned} \tag{96}$$

The first of these equations has two possible solutions,

[8]This procedure was taken from Ref. **[32]**, we repeat the calculation here since the reference has an error in the final result.

$$a = \frac{1}{2}\coth\big(2(\theta - c_1)\big), \tag{97}$$

and

$$a = \frac{1}{2}\tanh\big(2(\theta - c_1)\big), \tag{98}$$

where c_1 is a constant. However, if we want to satisfy the initial condition, we have to choose the first solution. Then, we substitute this solution back into the second line of Eq. 96, and solve the resulting ODE to get

$$b = c_2\coth\big(2(\theta - c_1)\big)\,\mathrm{sech}\big(2(\theta - c_1)\big), \tag{99}$$

where c_2 is a constant. Similarly, if we substitute this solution and the solution for a into the last line of Eq. 96, and solve the resulting ODE, we get

$$c = \frac{1}{2}\ln\Big(\sinh\big(2(\theta - c_1)\big)\Big) + \frac{c_2^2}{2}\coth\big(2(\theta - c_1)\big) - \ln(c_3), \tag{100}$$

where c_3 is a constant. Then, we can substitute back the solutions for Eq. 96 into Eq. 95 to get

$$\rho = \frac{c_3}{\sqrt{\sinh(2\theta)}}\exp\left[-\coth\big(2(\theta - c_1)\big)\left(\frac{\xi^2}{2} + c_2\,\mathrm{sech}\big(2(\theta - c_1)\big)\xi + \frac{c_2^2}{2}\right)\right]. \tag{101}$$

Nonetheless, to satisfy the initial condition (Eq. 94), we have to choose $c_1 = 0$, so we have

$$\rho = \frac{c_3}{\sqrt{\sinh(2\theta)}}\exp\left[-\coth\big(2\theta\big)\left(\frac{\xi^2}{2} + c_2\,\mathrm{sech}\big(2\theta\big)\xi + \frac{c_2^2}{2}\right)\right]. \tag{102}$$

Now, we have to analyze the behavior of our solution in the high-temperature limit, i.e., $\theta \longrightarrow 0$. For that reason, we use the following Taylor expansions

$$\begin{aligned}
\sinh x &= x + \frac{x^3}{16} + \cdots, \\
\coth x &= \frac{1}{x} + \frac{x}{3} + \cdots, \\
\mathrm{sech}\, x &= 1 - \frac{x^2}{2} + \cdots.
\end{aligned} \tag{103}$$

Then, if we expand at first order the trigonometric functions in the solution for ρ, we get

$$\rho = \frac{c_3}{\sqrt{2\theta}}\exp\big[-\frac{1}{4\theta}(\xi^2 + 2c_2\xi + c_2^2)\big]. \tag{104}$$

Thus, if we choose $c_2 = -\xi'$ to complete the square in the exponential, and $c_3 = \sqrt{\frac{m\omega}{2\pi\hbar}}$, we recover the solution for the free particle (Eq. 83) as expected. Therefore, the desired solution for the harmonic oscillator potential is

$$\rho(\xi, \xi'|\beta) = \sqrt{\frac{m\omega}{2\pi\hbar\sinh(2\theta)}}\exp\left[-\frac{\coth(2\theta)}{2}\big(\xi^2 - 2\xi'\xi\,\mathrm{sech}(2\theta) + \xi'^2\big)\right]. \tag{105}$$

Note that when $\theta \approx 0$, we recover the initial condition, i.e.,

$$\rho(x, x'|\beta) \approx \sqrt{\frac{m\omega}{2\pi\hbar(2\theta)}}\exp\left(-\frac{m\omega}{2\hbar}\frac{(x - x')^2}{2\theta}\right) \xrightarrow{\theta\longrightarrow 0} \delta(x - x'), \tag{106}$$

where we have used the fact that

$$\lim_{a\to 0^+}\sqrt{\frac{1}{\pi a}}\exp\left(\frac{-(x - x_0)^2}{a}\right) = \delta(x - x_0). \tag{107}$$

Note that since the partition function is defined as the trace of the density operator, we will only need the diagonal elements to compute average values[9]. Fortunately, the diagonal elements of the density operator can be written in a very simple form by using the following trigonometric identity

$$\coth(2\theta)\big[1-\operatorname{sech}(2\theta)\big]=\tanh\theta. \tag{108}$$

Therefore, for the diagonal elements of the density operator, we have

$$\rho(x,x|\beta)=\sqrt{\frac{m\omega}{2\pi\hbar\sinh(2\theta)}}\exp\bigg(-\frac{m\omega}{\hbar}x^2\tanh(\theta)\bigg). \tag{109}$$

Thus, we can compute the average value of the squared position as follows

$$\overline{x^2}=\frac{\int x^2\rho(x,x|\beta)dx}{\int\rho(x,x|\beta)dx}=\frac{\hbar}{2m\omega}\coth\bigg(\frac{\omega\beta\hbar}{2}\bigg). \tag{110}$$

Notice that we had to normalize the result because the density operator was not normalized. Similarly, for the average of the position, we have

$$\overline{x}=\frac{\int x\rho(x,x|\beta)dx}{\int\rho(x,x|\beta)dx}=0. \tag{111}$$

Therefore, the dispersion of the distribution function in position space can be easily computed as follows

$$\sigma_x^2=\overline{x^2}-\overline{x}^2=\frac{\hbar}{2m\omega}\coth\bigg(\frac{\hbar\omega}{2kT}\bigg). \tag{112}$$

In the case of ^{87}Rb atoms, we have $m\approx 1.4*10^{-25}$ Kg. Besides, a typical temperature value for an atomic trap is $T\approx 1\mu$K, while a typical frequency value is $\omega=2\pi*10$kHz. With these values, the width of the distribution function in position space becomes

$$\sigma_x\approx 0.1\mu m. \tag{113}$$

1.8.4 Time-evolution of the density matrix

The calculation of the last section was for the static case where the density matrix does not change in time. Nevertheless, once the atoms are released from the atomic trap, we can expect the density matrix to evolve in time under a new Hamiltonian. Thus, we need to compute the evolution of the density operator. Let's consider that at time t_0 the density operator is given by

$$\rho(t_0)=\sum_n\omega_n\left|n(t_0)\right\rangle\left\langle n(t_0)\right|. \tag{114}$$

In the Schrodinger picture, the state vectors evolve in time using the time-evolution operator as

$$U(t,t_0)\left|t_0\right\rangle=\left|t\right\rangle, \tag{115}$$

where

$$U(t,t_0)=\exp\bigg(-i\frac{H}{\hbar}(t-t_0)\bigg). \tag{116}$$

Then, the density operator at time t is given by

$$\begin{aligned}\rho(t)=U\rho(t_0)U^\dagger&=U\big(\sum_n\omega_n\left|n(t_0)\right\rangle\left\langle n(t_0)\right|\big)U^\dagger,\\&=\sum_n\omega_nU\left|n(t_0)\right\rangle\left\langle n(t_0)\right|U^\dagger.\end{aligned} \tag{117}$$

[9]It can be easily shown that the partition function is the trace of the density operator if we use the energy eigenkets. However, when two matrices are similar, their trace is the same, independently of the basis chosen, so this result is general.

As shown in many Quantum mechanics textbooks [**28**], it can be easily proved from this equation that the density operator evolves according to the following equation

$$i\hbar\frac{\partial\rho(t)}{\partial t} = -\big[\rho(t), H\big]. \tag{118}$$

However, if we could compute $U\left|n(t_0)\right\rangle$, our problem would be solved without the need to solve this PDE. It turns out that if we use as our base, the energy eingenkets of the Hamiltonian

$$H\left|n\right\rangle = E_n\left|n\right\rangle. \tag{119}$$

Then, the matrix elements of the density operator can be easily computed when the Hamiltonian does not depend on time, i.e.,

$$\begin{aligned}\left\langle n\right|\rho(t)\left|n'\right\rangle &= \left\langle n\right| e^{-i\frac{E_n}{\hbar}t}\rho(t_0)e^{i\frac{E_{n'}}{\hbar}t}\left|n'\right\rangle, \\ &= e^{-i\omega_{n,n'}t}\left\langle n\right|\rho(t_0)\left|n'\right\rangle,\end{aligned} \tag{120}$$

where we have defined

$$\omega_{n,n'} = \frac{E_n - E_{n'}}{\hbar}. \tag{121}$$

Note that this result means that when we use the energy eigenkets as our base, and when the Hamiltonian is independent of time, then the matrix elements out of the diagonal oscillate while the elements in the diagonal do not change with time.

1.8.5 Time-evolution of the density matrix due to a free particle Hamiltonian

Now that we know how to compute the time evolution of the density matrix, let's compute[10] the evolution of the density matrix when we release the atoms from the trap. When the atoms are trapped, the Hamiltonian is that of the harmonic oscillator. Thus, when the atoms are trapped, the density matrix of our system is given by Eq. 105. Then, we turn off the trap instantaneously, so we can suppose that the states immediately after we turn off the trap will still be the same (sudden approximation). Therefore, we can suppose that at time t_0 the density matrix is still given by Eq. 105. Let's suppose that the Hamiltonian after we turn off the trap is given by the free particle Hamiltonian, i.e.,

$$H = \frac{\hat{p}^2}{2m}.$$

If we want to use Eq. 120 to compute the time-evolution of the density matrix, we have to use the energy eigenkets of this Hamiltonian. Fortunately, we can use the momentum space eigenkets

$$\hat{p}\left|p\right\rangle = p\left|p\right\rangle, \tag{122}$$

since they are energy eigenkets of the free particle Hamiltonian, i.e,

$$H\left|p\right\rangle = \frac{\hat{p}^2}{2m}\left|p\right\rangle = \frac{p^2}{2m}\left|p\right\rangle. \tag{123}$$

Thus, using this base, the time-evolution of the matrix elements of ρ is given by

$$\rho(p,p',t|\beta) = e^{-i\omega_{p,p'}t}\rho(p,p',t_0\beta), \tag{124}$$

where

$$\rho(p,p',t_0) = \left\langle p\right|\rho(t_0)\left|p'\right\rangle, \tag{125}$$

and

$$\omega_{p,p'} = \frac{p^2 - p'^2}{2\hbar m}. \tag{126}$$

[10]This calculation is mine and was not taken from any reference.

Note that although we know the matrix elements in position space, now we need to know them in momentum space. Therefore, we have to change the base of the density matrix. This can be easily done by using the closure relation two times, i.e.,

$$\begin{aligned}\rho(p,p'|\beta) &= \langle p|\,\rho\,|p'\rangle\,,\\ &= \int dx\,\langle p|x\rangle\,\langle x|\,\rho\,|p'\rangle\,,\\ &= \int dx'\int dx\,\langle p|x\rangle\,\langle x|\,\rho\,|x'\rangle\,\langle x'|p'\rangle\,,\end{aligned} \tag{127}$$

where

$$\langle x|p\rangle = \frac{1}{\sqrt{2\pi\hbar}}e^{ipx/\hbar}. \tag{128}$$

Thus, we can write

$$\rho(p,p'|\beta) = \frac{1}{2\pi\hbar}\int dx'\int dx\exp\left[\frac{i}{\hbar}(p'x'-px)\right]\rho(x,x'|\beta). \tag{129}$$

In the same way, we can show that the inverse transformation is given by

$$\rho(x,x'|\beta) = \frac{1}{2\pi\hbar}\int dp'\int dp\exp\left[\frac{i}{\hbar}(px-p'x')\right]\rho(p,p'|\beta). \tag{130}$$

Therefore, we can compute the evolution of the density matrix as follows. First, the density matrix at time t_0 is given by Eq. 105, i.e.,

$$\rho(x,x',t_0|\beta) = \sqrt{\frac{m\omega}{2\pi\hbar\sinh(2\theta)}}\exp\left[-\frac{m\omega}{2\hbar}\coth(2\theta)\big(x^2-2x'x\,\mathrm{sech}(2\theta)+x'^2\big)\right]. \tag{131}$$

Then, we use Eq. 129 to change the basis from position space to momentum space. The final result after performing the integrals is

$$\rho(p,p',t_0|\beta) = \sqrt{\frac{\mathrm{csch}(\beta\hbar\omega)}{2\pi\hbar m\omega}}\exp\left[-\frac{\big[(p^2+p'^2)\coth(\beta\hbar\omega)-2pp'\,\mathrm{csch}(\beta\hbar\omega)\big]}{2m\hbar\omega}\right]. \tag{132}$$

Then, we can use Eq. 124 to compute the time-evolution, i.e.,

$$\begin{aligned}\rho(p,p',t|\beta) = \sqrt{\frac{\mathrm{csch}(\beta\hbar\omega)}{2\pi\hbar m\omega}}\exp\left[\frac{-i(p-p')(p+p')\omega t}{2m\hbar\omega}\right]\\ \exp\left[\frac{-(p^2+p'^2)\coth(\beta\hbar\omega)+2pp'\,\mathrm{csch}(\beta\hbar\omega)}{2m\hbar\omega}\right].\end{aligned} \tag{133}$$

Finally, we can use Eq. 130 to return the matrix elements to the position base. The result after performing the integrals is

$$\rho(x,x',t|\beta) = f(t)\exp\left[mw\frac{\big[i\omega t(x^2-x'^2)-(x^2+x'^2)\coth(\beta\hbar\omega)+2xx'\,\mathrm{csch}(\beta\hbar\omega)\big]}{2(\hbar+\omega^2t^2\hbar)}\right], \tag{134}$$

where we have defined the amplitude $f(t)$ as follows

$$f(t) = \frac{1}{2\pi\hbar}\sqrt{\mathrm{csch}(\beta\hbar\omega)\frac{\big(-2\pi mt\omega^2\hbar+2i\pi m\omega\hbar\coth(\beta\hbar\omega)\big)}{\big(i\omega t+\coth(\beta\hbar\omega)\big)\big(i+i\omega^2t^2\big)}}. \tag{135}$$

Therefore, the matrix elements at the diagonal are

$$\rho(x,x,t|\beta) = f(t)\exp\left[\frac{x^2 mw\big(-\coth(\beta\hbar\omega)+\operatorname{csch}(\beta\hbar\omega)\big)}{\hbar(1+w^2t^2)}\right]. \tag{136}$$

We can use this result to compute the average value of the squared position, i.e.,

$$\overline{x^2}(t) = \frac{\int x^2\rho(x,x,t|\beta)dx}{\int \rho(x,x,t|\beta)dx} = \frac{\hbar}{2m\omega}(1+\omega^2t^2)\coth\left(\frac{\hbar\omega}{2kT}\right). \tag{137}$$

Similarly, the average value of the position is

$$\overline{x}(t) = \frac{\int x\rho(x,x,t|\beta)dx}{\int \rho(x,x,t|\beta)dx} = 0. \tag{138}$$

Finally, we can use these results to compute the dispersion of the distribution in position space, i.e.,

$$\sigma_x^2(t) = \overline{x^2}(t) - \overline{x}^2(t) = \frac{\hbar}{2m\omega}(1+\omega^2t^2)\coth\left(\frac{\hbar\omega}{2kT}\right). \tag{139}$$

The above equation gives the expansion of the atomic distribution in position space for the atoms after they are released from the trap. Note how the expansion depends on the parameters of the trap (ω and T). Besides, for $t = 0$ we recover the standard deviation for the harmonic oscillator distribution in position space as expected (Eq. 112).

1.8.6 Time-evolution of the density matrix due to a free fall Hamiltonian

In the previous section, we computed the density matrix for an atomic ensemble initially subjected to a harmonic oscillator potential and then its time evolution due to a free particle Hamiltonian. As a result, we were able to compute the expansion of the atomic cloud. However, that calculation did not include the gravitational potential. In this section, we will generalize our calculation to include the potential energy due to gravity. We will show that the result in Eq. 139 holds even if we consider the gravitational potential with the difference that now distribution travels following a free fall trajectory.

In this case, when we turn off instantaneously the atomic trap at $t = t_0$, the new Hamiltonian will be given by[11]

$$H = \frac{\hat{p}^2}{2m} + mg\hat{x}. \tag{140}$$

We will assume that the momentum operator acts in the x-direction, i.e., $\hat{p}_x$, but we will continue writing just $\hat{p}$ for simplicity. We remember that the time-evolution of the matrix elements of the density operator is given by

$$\langle n|\,\rho(t)\,|n'\rangle = \langle n|\,U^\dagger\rho(t_0)U\,|n'\rangle\,, \tag{141}$$

and this time, the evolution operator will be given by

$$U = \exp\left[-\frac{i}{\hbar}\left(\frac{\hat{p}^2}{2m} + mg\hat{x}\right)t\right]. \tag{142}$$

Previously, it was possible to compute the matrix elements of $\rho(t)$ by using the energy eigenkets. This time is not so trivial to know what are the eigenkets of the Hamiltonian in Eq. 140, but let's insist on continuing using the momentum eigenkets $|p\rangle$. Thus, using this base, the matrix elements are given by

$$\langle p|\,\rho(t)\,|p'\rangle = \langle p|\,U^\dagger\rho(t_0)U\,|p'\rangle\,. \tag{143}$$

This means that we need to evaluate

$$|p(t)\rangle = \exp\left[-\frac{i}{\hbar}\left(\frac{\hat{p}^2}{2m} + mg\hat{x}\right)t\right]|p(t_0)\rangle\,, \tag{144}$$

[11] Note that the gravitational potential $U_g = mgx$ is the result of taking the negative of the gradient of the gravitational force $F_g = -mg$. This means that the acceleration is $a = -g$. Thus, in this convention g is positive. Besides, we have that $x = x_0 + v_0t - \frac{1}{2}gt^2$, therefore, the system of coordinates points upwards such that if the atom is falling, its momentum will be negative as we will see later.

where $|p(t_0)\rangle \equiv |p\rangle$. To do so, we will prove that $\exp\left(\pm\frac{i}{\hbar}mg\hat{x}t\right)|p\rangle$ is an eigenfunction of the operator $\hat{p}$. We begin by using the following commutator relation **[28]**

$$\left[\hat{p}, f(\hat{x})\right] = -i\hbar\frac{\partial f}{\partial \hat{x}}, \tag{145}$$

where f is a function of the operator $\hat{x}$. If we choose $f(\hat{x}) = \exp\left(\pm\frac{i}{\hbar}mg\hat{x}t\right)$, then we have

$$\left[\hat{p}, \exp\left(\pm\frac{i}{\hbar}mg\hat{x}t\right)\right] = \pm mgt\exp\left(\pm\frac{i}{\hbar}mg\hat{x}t\right). \tag{146}$$

Thus, if we multiply this equation by $|p\rangle$ from the right, we get the following relation

$$\hat{p}\left(\exp\left(\pm\frac{i}{\hbar}mg\hat{x}t\right)|p\rangle\right) = (p \pm mgt)\left(\exp\left(\pm\frac{i}{\hbar}mg\hat{x}t\right)|p\rangle\right). \tag{147}$$

Then, we see that $\exp\left(\pm\frac{i}{\hbar}mg\hat{x}t\right)|p\rangle$ is an eigenfunction of the momentum operator with eigenvalue $(p \pm mgt)$. In other words, the operator $\exp\left(\pm\frac{i}{\hbar}mg\hat{x}t\right)$ is the translation operator in momentum since it translates $|p\rangle$ into $|p \pm mgt\rangle$[12]. It is convenient to use a more succinct notation for the next steps, we define[13]

$$k \equiv \frac{mg}{\hbar}t. \tag{148}$$

Thus, we have

$$\exp\left(\pm\frac{i}{\hbar}mg\hat{x}t\right) \equiv \exp\left(\pm\frac{i}{\hbar}\hbar k\hat{x}\right), \tag{149}$$

so we can see that $\hbar k\hat{x}$ is the generator of translation in momentum space. Hence, we can proceed to compute

$$|p(t)\rangle = \exp\left[-\frac{i}{\hbar}\left(\frac{\hat{p}^2}{2m} + \hbar k\hat{x}\right)t\right]|p(t_0)\rangle\,. \tag{150}$$

For that purpose, we will use the split operator method **[34, 35, 36, 37]**. This method is based on the Baker–Campbell–Hausdorff formula

$$e^A e^B = e^{A+B+\frac{1}{2}[A,B]+\cdots}, \tag{151}$$

where A and B are operators. By using this formula, we can approximate[14] the time-evolution operator for a small time step, Δt, as the product of two independent time-evolution operators, i.e.,

$$\exp\left(-\frac{i}{\hbar}\frac{\hat{p}^2}{2m}\Delta t - \frac{i}{\hbar}\hbar\Delta k\hat{x}\right) \approx \exp\left(-\frac{i}{\hbar}\frac{\hat{p}^2}{2m}\Delta t\right)\exp\left(-\frac{i}{\hbar}\hbar\Delta k\hat{x}\right), \tag{152}$$

where we have ignored non-linear terms in Δt, and $\Delta k = \frac{mg}{\hbar}\Delta t$. Using the above result, we can write

$$|p(\Delta t)\rangle \approx \exp\left(-\frac{i}{\hbar}\frac{\hat{p}^2}{2m}\Delta t\right)\exp\left(-\frac{i}{\hbar}\hbar\Delta k\hat{x}\right)|p\rangle\,. \tag{153}$$

Hence, to take a time-step Δt, we have to apply a translation in momentum, followed by the time-evolution step corresponding to the Hamiltonian of a free particle. More explicitly, for one step we have that[15]

[12] Note that the translation operator in momentum space has the reversed sign in comparison with the usual translation operator in position space. In that case, a negative sign means a translation $x + dx$, and vice versa

[13] I ran out of letters. Be aware that this definition will only apply to this section and do not confuse it with previous definitions using the same letter.

[14] Note that if the operators $[A, B]$ in the Baker–Campbell–Hausdorff commute, then this formula reduces to the familiar exponential identity of real exponents. In the case of position and momentum, we have that $[\hat{x}_i, \hat{p}_j] = i\hbar\delta_{i,j}$ so the Eq. 152 is exact when the position and momentum operators act on orthogonal directions. However, in our case, they act in the same direction.

[15] Note that the initial momentum can be positive if the atom was launched upwards when the trap was turned off, or negative if it was launched downwards.

$$\begin{aligned} |p(\Delta t)\rangle &= \exp\left(-\frac{i}{\hbar}\frac{\hat{p}^2}{2m}\Delta t\right)|p-\hbar\Delta k\rangle \\ &= \exp\left(-\frac{i}{\hbar}\frac{(p-\hbar\Delta k)^2}{2m}\Delta t\right)|p-\hbar\Delta k\rangle\,. \end{aligned} \tag{154}$$

If we now take a second step, we have

$$\begin{aligned} |p(2\Delta t)\rangle &= \exp\left(-\frac{i}{\hbar}\frac{\hat{p}^2}{2m}\Delta t\right)\exp\left(-\frac{i}{\hbar}\hbar\Delta k\hat{x}\right)|p(\Delta t)\rangle \\ &= \exp\left(-\frac{i}{\hbar}\frac{[(p-\hbar\Delta k)^2+(p-2\hbar\Delta k)^2]}{2m}\Delta t\right)|p-2\hbar\Delta k\rangle\,. \end{aligned} \tag{155}$$

In the same way, taking another step, we have

$$\begin{aligned} |p(3\Delta t)\rangle &= \exp\left(-\frac{i}{\hbar}\frac{\hat{p}^2}{2m}\Delta t\right)\exp\left(-\frac{i}{\hbar}\hbar\Delta k\hat{x}\right)|p(2\Delta t)\rangle \\ &= \exp\left(-\frac{i}{\hbar}\frac{[(p-\hbar\Delta k)^2+(p-2\hbar\Delta k)^2+(p-3\hbar\Delta k)^2]}{2m}\Delta t\right)|p-3\hbar\Delta k\rangle\,. \end{aligned} \tag{156}$$

Taking N steps we have that

$$|p(N\Delta t)\rangle = \exp\left(-\frac{i}{\hbar}\frac{1}{2m}\sum_{n=1}^{N}(p-n\hbar\Delta k)^2\Delta t\right)|p-N\hbar\Delta k\rangle\,. \tag{157}$$

We can recognize the sum in the exponential as a Riemann sum, thus, if we now take the limit $N\longrightarrow\infty$, we have that $N\Delta t\longrightarrow t$, and $N\hbar\Delta k\longrightarrow mgt$, so we can write

$$|p(t)\rangle = \exp\left(-\frac{i}{\hbar}\frac{1}{2m}I(t)\right)|p-mgt\rangle\,, \tag{158}$$

where $I(t)$ is a Riemann integral given by

$$\begin{aligned} I(t) &= \lim_{\Delta t\to 0}\sum_{n=1}^{N}(p-n\hbar\Delta k)^2\Delta t, \\ &= \int_0^t (p-mgt')^2dt', \\ &= p^2t - pmgt^2 + \frac{m^2g^2t^3}{3}. \end{aligned} \tag{159}$$

Finally, we have the evolution of the momentum eigenket

$$|p(t)\rangle = \exp\left(-\frac{i}{\hbar}\frac{1}{2m}\left(p^2t - pmgt^2 + \frac{m^2g^2t^3}{3}\right)\right)|p-mgt\rangle\,. \tag{160}$$

Thus, we can use this result to compute the time-evolution of the matrix elements of the density operator

$$\begin{aligned} \rho(p,p',t|\beta) &= \langle p|\,\rho(t)\,|p'\rangle\,, \\ &= \langle p(t)|\,\rho(t_0)\,|p'(t)\rangle\,, \\ &= e^{-i\omega_{p,p'}t}\,\langle p-mgt|\,\rho(t_0)\,|p'-mgt\rangle\,, \\ &= e^{-i\omega_{p,p'}t}\rho(p-mgt,p'-mgt,t_0|\beta), \end{aligned} \tag{161}$$

where we have defined

$$\omega_{p,p'} = \frac{1}{2m\hbar}\big[(p^2 - p'^2) - (p - p')mgt\big]. \tag{162}$$

Note that the matrix elements of the initial density operator appear translated by an amount $-mgt$, and that the frequency $\omega_{p,p'}$ has an extra term in comparison with Eq. 126. Thus, the procedure to get the evolution of the matrix elements of the density operator in the position basis is the same as before. First, we use Eq. 129 to write the initial density operator (Eq. 105) in the momentum basis. The result is given in Eq. 132. Then, we use this result alongside Eq. 161 to compute the time evolution of the density matrix in momentum space, i.e.,

$$\rho(p,p',t|\beta) = e^{-i\omega_{p,p'}t}\sqrt{\frac{\operatorname{csch}(\beta\hbar\omega)}{2\pi\hbar m\omega}} \exp\left[-\frac{\big[((p-mgt)^2 + (p'-mgt)^2)\coth(\beta\hbar\omega) - 2(p-mgt)(p'-mgt)\operatorname{csch}(\beta\hbar\omega)\big]}{2m\hbar\omega}\right] \tag{163}$$

Finally, we use Eq. 130 to return the matrix elements to the position base. After performing the integral, the result is

$$\rho(x,x',t|\beta) = \Delta\exp\left(i\frac{mt}{2\hbar}(x-x')\frac{\big[g(2+t^2\omega^2) + \omega^2(x+x')\big]}{(1+\omega^2t^2)}\right) \exp\left(-\frac{\pi}{2}\Delta^2\Big[\big(g^2t^4 - 2gt^2(x+x') + 2(x^2+x'^2)\big)\cosh(\beta\hbar\omega) - (gt^2-2x)(gt^2-2x')\Big]\right), \tag{164}$$

where

$$\Delta = \sqrt{\frac{m\omega}{2\pi\hbar(1+\omega^2t^2)\sinh(\beta\hbar\omega)}}. \tag{165}$$

Therefore, the diagonal elements are given by

$$\rho(x,x,t|\beta) = \Delta\exp\left(-\frac{\pi}{2}\Delta^2\Big[\big(g^2t^4 - 4gt^2x + 4x^2\big)\cosh(\beta\hbar\omega) - (gt^2-2x)^2\Big]\right). \tag{166}$$

Then, as usual, we can compute the average of the squared position and the position itself. After a lot of algebraic manipulation, we get

$$\overline{x^2}(t) = \frac{\int x^2\rho(x,x,t|\beta)dx}{\int\rho(x,x,t|\beta)dx} = \frac{gt^2(2+Bgt^2)}{4B}, \tag{167}$$

where

$$B = \frac{m\omega gt^2}{\hbar(1+w^2t^2)}\tanh\left(\frac{\beta}{2}\hbar\omega\right), \tag{168}$$

and also

$$\overline{x}(t) = \frac{\int x\rho(x,x,t|\beta)dx}{\int\rho(x,x,t|\beta)dx} = \frac{gt^2}{2}. \tag{169}$$

Using these results, we can compute the standard deviation as a function of time

$$\sigma_x(t) = \sqrt{\frac{\hbar(1+t^2\omega^2)}{2m\omega}\coth\left(\frac{\beta}{2}\hbar\omega\right)}. \tag{170}$$

We can see that this result is the same as that in Eq. 139. Thus, the only effect of gravity was to introduce a change in the average position. Indeed, the average position of the atom is that of a free-fall particle just as we could have expected.

1.9 Gravimetry signal set by the expansion time

In the last sections, we computed the expansion of the atomic width in position space for two different initial conditions. In this section, we will study the constraints that choosing a particular type of expansion will impose in the interrogation time without affecting the Rabi transitions due to the detuning. In particular, we are interested in knowing how the parameters that can be easily controlled during the experiment will affect the total expansion time. These parameters are the power of the microwaves used to drive the transitions and the linear magnetic field gradient.

1.9.1 Rabi frequency set by the power of the microwaves

As we showed in Eq. 53, the intensity of the magnetic field used to drive the Rabi oscillations will set a warning width that defines the maximum uncertainty in position space that the wave function can have for a successful transition to the desired state. To guarantee that the transition happens with a high probability of success, the wave function's width has to lie inside this warning width. The warning width $\Delta Z'$ is set by a frequency Ω' according to Eq. 53. Thus, the Rabi frequency will be directly proportional to the magnitude of the magnetic field of the microwaves used to drive the transition. This magnetic field can be measured by using a power meter to measure the power of the radiation according to

$$P = I \int dA, \tag{171}$$

where dA is the differential element of area perpendicular to the direction and I is the intensity of the electromagnetic wave. The power meter measures the intensity of the electric field E and is given by

$$I = \frac{1}{2} c\epsilon_0 |E|^2, \tag{172}$$

where ϵ_0 is the permittivity of free space and c is the speed of light in vacuum. Therefore, the power of the microwaves can be written as

$$P = \frac{1}{2} c\epsilon_0 |E|^2 A, \tag{173}$$

where we have evaluated the area of the power meter. This equation can be re-written in terms of the magnetic field using the following relation

$$E = cB = \frac{B}{\sqrt{\mu_0 \epsilon_0}}, \tag{174}$$

where μ_0 is the vacuum permeability. Thus, the power is given by

$$P = \frac{c|B|^2}{2\mu_0} A. \tag{175}$$

Now, we can solve for the magnetic field in terms of the power measured, i.e.,

$$|B| = \sqrt{\frac{2\mu_0 P}{cA}}. \tag{176}$$

We can calculate the Rabi frequency produced by this magnetic field using Eq. 53

$$\Omega = \frac{-B \langle e | \, \hat{\boldsymbol{e}} \cdot \boldsymbol{\mu} \, | g \rangle}{\hbar},$$

where $\hat{\boldsymbol{e}}$ is the direction of polarization of the magnetic field and $\boldsymbol{\mu}$ is the total magnetic moment of the atom given by the spin, orbital, and nuclear contributions, i.e.,[16]

$$\boldsymbol{\mu} = \frac{\mu_B}{\hbar} (g_S \boldsymbol{S} + g_L \boldsymbol{L} - g_I \boldsymbol{I}). \tag{177}$$

[16] In this convention the eigenvalues of the operators $\boldsymbol{S}$, $\boldsymbol{L}$, and $\boldsymbol{I}$ have units of angular momentum, i.e., $Joules * Seconds$, and the Bohr magneton is defined as $\frac{\hbar e}{2m_e}$. Besides, the Landé g-Factors g_S and g_L are positive while g_I has a negative value. Notice that $\boldsymbol{\mu}$ has to have units of $Amperes * (Meters)^2$.

We will take the magnetic field to be along the z-axis (the atomic quantization axis). Thus, we can write the Rabi frequency as[17]

$$\Omega' = \sqrt{\frac{2\mu_0 P}{cA}} \frac{\langle e| \mu_z |g\rangle}{\hbar}, \tag{178}$$

where

$$\mu_z = \frac{\mu_B}{\hbar}(g_S S_z + g_L L_z - g_I I_z). \tag{179}$$

1.9.2 Warning width set by the power of the microwaves

We can compute the warning width given by the Rabi frequency in Eq. 178 using Eq. 52, i.e.,

$$\Delta Z' = \sqrt{3}\Omega' \frac{\hbar}{\mu_B g_{F_{eff}} m_{F_{eff}} \eta},$$

so we can write

$$\Delta Z' = \sqrt{\frac{6\mu_0 P}{cA}} \frac{\langle e| \mu_z |g\rangle}{\mu_B g_{F_{eff}} m_{F_{eff}} \eta}. \tag{180}$$

This condition gives the maximum uncertainty in position space that the atomic wave function can have for resonant transitions. Thus, we have to work always within this range. For this reason, we define the maximum acceptable uncertainty as

$$\Delta Z_f = \gamma \Delta Z', \quad 0 < \gamma \leq 1, \tag{181}$$

where the smaller the value of γ, the better the chances to drive the desired transitions.

1.9.3 Interrogation time for a pure state

We can use Eq. 67 to compute the initial width that will maximize the time to reach the final width of Eq. 181, i.e.,

$$(\Delta Z_0)^* = \frac{\gamma \Delta Z'}{\sqrt{2}}. \tag{182}$$

By selecting this initial width, the time needed to reach ΔZ_f will be given by Eq. 68, i.e.,

$$t_{max} = \frac{M}{\hbar}(\gamma \Delta Z')^2. \tag{183}$$

By substituting Eq. 180 into the last equation we get

$$t_{max} = \frac{6M\mu_0 P}{\hbar c A} \left(\frac{\gamma \langle e| \mu_z |g\rangle}{\mu_B g_{F_{eff}} m_{F_{eff}} \eta} \right)^2. \tag{184}$$

This equation represents the maximum time that we can let the wave packet expand in terms of the power of the microwaves and the proportionality factor γ. Next, we can use Eq. 37 to compute the gravimetry signal that we could obtain by performing an atomic interference experiment with a total duration equal to t_{max}, i.e.,

$$\Delta\Phi = 4\frac{\mu_B \eta}{\hbar} g T^3, \tag{185}$$

where T controls the time of free evolution between the pulses according to Eq. 14. By considering the Rabi pulses to have an infinitesimal duration, the total duration of the experiment t_{max} is given by

$$4T \approx t_{max}. \tag{186}$$

Thereby, using Eqs. 184, 185, and 186, we obtain[18]

[17] We will consider the Rabi frequency to be real and positive.

[18] Note that P/A is the irradiance of the microwaves.

$$\Delta\Phi = bg\left(\frac{P}{A}\right)^3, \tag{187}$$

where we have defined the parameter

$$b \equiv \frac{1}{2}\frac{\mu_B}{\hbar^4\eta^5}\left(\frac{3M\mu_0}{c}\right)^3\left(\frac{\langle e|\,\mu_z\,|g\rangle}{\mu_B g_{F_{eff}} m_{F_{eff}}}\right)^6\gamma^6. \tag{188}$$

1.9.4 Interrogation time for an optical dipole trap

Notice that we can re-write Eq. 169 as

$$\Delta Z(t) = \Delta Z(0)\sqrt{1+t^2\omega^2}, \tag{189}$$

where $\Delta Z(0)$ is the initial width just after the dipole the trap is turned off and is given by

$$\Delta Z(0) = \sqrt{\frac{\hbar}{2M\omega}\coth\left(\frac{\hbar\omega}{2kT}\right)}. \tag{190}$$

Notice that, contrary to the behavior of Eq. 65, the only way to minimize the expansion from an optical dipole trap is to minimize the initial width as much as possible. Thus, we would have to either decrease the temperature of the trap or increase the oscillating frequency. However, these experimental parameters are not easy to tweak. For typical experimental values, we have a high-temperature regime ($\hbar\omega \gg kT$), thus, we can expand the hyperbolic cotangent in Eq. 190 using a Maclaurin series. In this limit, the initial width can be written as

$$\Delta Z(0) \approx \sqrt{\frac{kT}{M\omega^2}}, \quad (\hbar\omega \ll kT). \tag{191}$$

For instance, for $T \approx 1\mu$K and $\omega = 4\pi * 10$ kHz, we have that $\hbar\omega \approx 1.3 * 10^{-29}$ J and $2kT \approx 2.76 * 10^{-29}$ J. Thus, the argument of the hyperbolic cotangent in Eq. 189 is $\frac{\hbar\omega}{2kT} \approx 0.48$, and we have that the expansion of the hyperbolic cotangent using a Maclaurin series is justified. Indeed, we can relax our high-temperature condition to $\hbar\omega < 2kT$. We can use the above result to rewrite the expansion in Eq. 189 as

$$\Delta Z(t) = \sqrt{\frac{kT}{M\omega^2}}\sqrt{1+t^2\omega^2}, \quad (\hbar\omega < 2kT). \tag{192}$$

As before, this equation does not have a minimum with respect to ω or T. Indeed, the larger the frequency or the smaller the temperature, the smaller the expansion. Note that for long expansion times, we can approximate the last result as

$$\Delta Z(t) \approx \sqrt{\frac{kT}{M}}t, \quad (\hbar\omega < 2kT \quad , \quad 1 \ll \omega t). \tag{193}$$

Note that in this limit, the expansion is directly proportional to the RMS velocity $v_{rms} = \sqrt{kT/M}$ **[38]**. By using this result and Eq. 181, we get

$$t_{max} = \sqrt{\frac{M}{kT}}\gamma\Delta Z', \tag{194}$$

and by substituting Eq. 180 into this result, we obtain

$$t_{max} = \sqrt{\frac{6M\mu_0 P}{kTcA}}\frac{\gamma\,\langle e|\,\mu_z\,|g\rangle}{\mu_B g_{F_{eff}} m_{F_{eff}}\eta}. \tag{195}$$

The phase signal for this case is obtained, as before, by using Eqs. 186 and 185

$$\Delta\Phi = b_d g\left(\frac{P}{A}\right)^{3/2}, \tag{196}$$

where we have defined the parameter

$$b_d \equiv \frac{1}{16}\frac{\mu_B}{\hbar\eta^2}\left(\frac{\gamma\,\langle e|\,\mu_z\,|g\rangle}{\mu_B g_{F_{eff}} m_{F_{eff}}}\sqrt{6\frac{M}{kT}\frac{\mu_0}{c}}\right)^3. \tag{197}$$

1.10 Fractional precision

After the sequence of pulses has been applied not all the atoms in the cloud will have seen the same sequence of pulses. This is mainly because of the detuning introduced by the displacement in the position of the atoms due to the Zeeman effect. Therefore, after the sequence is applied, the normalized population of atoms in the upper state will be given by

$$P = \frac{1}{2}(1 + C\cos\Delta\Phi), \tag{198}$$

where C is the fringe contrast and $\Delta\Phi$ is given by Eq. 187 or Eq. 196. We define the signal-to-noise-ratio (SNR) as the ratio between the contrast of the fringes and the uncertainty on the slope of the fringe, i.e,

$$SNR = \frac{C/2}{\sigma_p}, \tag{199}$$

where the uncertainty on the slope of the fringe can be calculated using Eq. 198, i.e,

$$\sigma_p = \frac{C}{2}|\sin\Delta\Phi|\sigma_{_{\Delta\Phi}}. \tag{200}$$

Therefore, the SNR will be given by

$$SNR = \frac{1}{|\sin\Delta\Phi|\sigma_{_{\Delta\Phi}}}. \tag{201}$$

At mid fringe we have $\Delta\Phi = \frac{\pi}{2}$, so the SNR will be given by

$$SNR = \frac{1}{\sigma_{_{\Delta\Phi}}}. \tag{202}$$

Let's focus on Eq. 187 and take its the product with Eq. 202 as follows

$$\frac{\Delta\Phi}{\sigma_{_{\Delta\Phi}}} = bg\left(\frac{P}{A}\right)^3 SNR. \tag{203}$$

This equation is the sensitivity or fractional precision in the measurement of the gravimetry signal but we would like to have the sensitivity in the measurement of g. Thus, we have to notice that since there exists a linear relation between g and $\Delta\phi$ (Eq. 187), there also exists a linear relationship between the uncertainty σ_g and the uncertainty $\sigma_{_{\Delta\Phi}}$, i.e.,

$$\sigma_{_{\Delta\Phi}} = b\sigma_g\left(\frac{P}{A}\right)^3, \tag{204}$$

so we can write

$$\frac{\Delta\Phi}{\sigma_{_{\Delta\Phi}}} = \frac{g}{\sigma_g}. \tag{205}$$

Thus, if we substitute this equation back into Eq. 203, we get the sensitivity in the measurement of g, i.e.,

$$\frac{\sigma_g}{g} = \frac{1}{bg\big(P/A\big)^3 SNR}. \tag{206}$$

Thus, the precision in the measurement is given by

$$\sigma_g = \frac{1}{b\big(P/A\big)^3 SNR}. \tag{207}$$

In the same way, using Eq. 196, we get the fractional precision for the case of an optical dipole trap as follows

$$\frac{\sigma_g}{g} = \frac{1}{b_d g\big(P/A\big)^{3/2} SNR}, \tag{208}$$

and the precision is given by

$$\sigma_g = \frac{1}{b_d\big(P/A\big)^{3/2} SNR}. \tag{209}$$

Notice that the above results represent the fractional precision attainable in a single shoot measurement. However, the precision can be further improved by leveraging the fact that the uncertainty improves as the square root of the number of measurements [**39**]. For example, to improve the precision by two orders of magnitude, we could average 10^4 measurements.

1.11 Intrinsic decoherence of the Rabi oscillations

Up until now, we have been considering that the pulses in Eq. 14 have an infinitesimal duration. However, in reality, these pulses have a finite duration (e.g., $t = \pi/\Omega$ for a π-pulse). The finite pulse duration causes a phase shift in the case of conventional light-pulse atom interferometers [**40**] and a similar phase shift occurs in the case of the magnetic gravimeter as well. However, in the case of the magnetic gravimeter, this effect is intrinsic to the technique and is caused by the requirement of having opposite magnetic accelerations for each level (Eq. 3) as was discussed in Ref. [**18**]. The result is an inevitable loss of visibility of the Rabi oscillations that increases with the phase shift. In Ref. [**18**], we established the condition for a short-pulse

$$|\Delta\Phi_{sep}(\tau)| < \pi, \tag{210}$$

with the phase shift given by

$$\Delta\Phi_{sep}(\tau) = \frac{m}{2\hbar}\left[3v_{rms}(a_+ - a_-)\tau^2 + (a_+^2 - a_-^2)\tau^3\right], \tag{211}$$

where $v_{rms} = \sqrt{k_B T_0/m}$ and τ is the pulse duration. The condition for a short pulse ensures that the loss of visibility will not be significant and can be obtained through a numerical simulation. The code of the numerical simulation and a heuristic justification of it can be found in Appendix A.

1.12 Phase shift due to position-dependent acceleration gradients

In the last sections, we have been considering a total acceleration of the form given by Eq. 3. However, in reality, there may exist an additional position-dependent acceleration component that causes a phase shift in the result of Eq. 37. In this section, we compute the order of magnitude of that phase shift. Let's consider that there exists a linear acceleration gradient so the total acceleration now has the form

$$a_{\pm,grad} = a_\pm + \gamma_\pm z_{\pm,grad}, \tag{212}$$

where we have used a sub-index in the gradient term to indicate that the gradient may have a different value depending on the level under consideration. To compute the phase shift, we will solve the integral of Eq. 15 but this time, with the total acceleration given by Eq. 212. Firstly, we need to solve the following differential equation to get the time-dependent equations of motion

$$z''_{\pm,grad} - \gamma_\pm z_{\pm,grad} = a_\pm.$$

By using the appropriate initial conditions, the solution is given by

$$\begin{aligned}
z_{\pm,grad}(t) &= \frac{1}{\gamma_\pm}\big(-a_\pm + [a_\pm + z_0\gamma_\pm]\cosh\sqrt{\gamma_\pm}t + v_0\sqrt{\gamma_\pm}\sinh\sqrt{\gamma_\pm}t\big),\\
v_{\pm,grad}(t) &= v_0\cosh\sqrt{\gamma_\pm}t + \left[\frac{a_\pm + z_0\gamma_\pm}{\sqrt{\gamma_\pm}}\right]\sinh\sqrt{\gamma_\pm}t,\\
a_{\pm,grad}(t) &= [a_\pm + z_0\gamma_\pm]\cosh\sqrt{\gamma_\pm}t + v_0\sqrt{\gamma_\pm}\sinh\sqrt{\gamma_\pm}t.
\end{aligned} \tag{213}$$

Now, by using this result and the sequence of pulses of Eq. 14 to perform the integral of Eq. 15, we obtain

$$\Delta\tilde{\Phi} = -\frac{4m}{\hbar}\left[\frac{\mu_B\eta}{m}g_F m_F\{3g + z_0(\gamma_+ + \gamma_-)\} + (v_0^2 + gz_0)(\gamma_+ - \gamma_-)\right]T^3, \tag{214}$$

where we have performed an expansion around $T = 0$, only kept linear gradient terms, and we have considered that $a_{C_e} = -a_{C_g}$. By using Eq. 37, our final result can be written as

$$\tilde{g} \sim g + (\gamma_+ + \gamma_-)(z_0 + v_0T + 3gT^2) + \\ 2(\gamma_+ - \gamma_-)[(a_- - a_+)T^2 + (v_0^2 + gz_0 + 3gv_0T + 9g^2T^2)/(a_- - a_+)] + \cdots . \tag{215}$$

Finally, it is noteworthy that the gradient term can have different origins such as quadratic terms in the gravitational potential (see Eq. 20), the nonlinearity of the magnetic field (see Eq. 1), and the quadratic Zeeman effect (see Eq. 41).

1.13 Conclusions and perspectives

In this chapter, we have studied the magnetic gravimeter. We presented the concept of the technique, developed the theoretical framework, and showed the feasibility of the proposed apparatus to measure gravity. In particular, we estimated the fractional precision that could be achieved with this technique following the constraint set by the expansion of the atomic cloud. Later, we calculated the phase shift due to the finite pulse duration and its effect on the loss of visibility of the Rabi oscillations. Finally, we considered the effect of position-dependent acceleration gradients and provided an estimation of the correction caused by this effect. These calculations complement our work done in Ref. [**18**]. We leave for future work a more detailed study of acceleration gradients and other systematic effects that cause loss of visibility, the relationship of the parameter γ defined in Eq. 181 with the wave function alongside a more rigorous derivation of Eq. 210.

2 The Light-based Gravimeter

2.1 Intermission

The purpose of this chapter is to serve as a complement to the article *Light-based Gravimetry*, which I co-authored with Eduardo Gomez and is currently under review. Many calculations, derivations, and conceptual discussions were abbreviated or omitted in the manuscript for clarity and brevity. In this chapter, I present these additional details and insights.

2.2 Motivation

Since I was just finishing the second year of my doctoral studies and had already finished my research on the magnetic gravimeter (presented in the last section). I decided to look for a new research topic to continue my doctorate. I was introduced to the idea of a gravimeter that could leverage the gravitational redshift to measure the local acceleration of gravity by my supervisor: *Eduardo Gomez*. A quick calculation showed that the idea seemed feasible as will be shown below. I decided to pursue this idea because it seemed rather novel and interesting. Lately, we found out that Ref. [**41**] had already studied a similar experiment; however, their approach to the matter is quite different, so our contribution is still valuable. To the best of our knowledge, this is the only work, previous to ours, that seemed to have studied this type of gravimeter. The scientific community had only focused on experiments to measure the gravitational redshift (see, for example, Ref. [**42**]).

2.3 Gravitational redshift

When an electromagnetic wave propagates through a region of varying gravitational potential, its frequency undergoes a shift known as the gravitational redshift. Specifically, radiation climbing out of a gravitational well arrives at a lower potential with a reduced frequency (and correspondingly increased wavelength) relative to its emitted value [**43**]. This effect is a consequence of the Strong Equivalence Principle (SEP) also known as the Einstein Equivalence Principle[19] (EEP) [**44**], and therefore, it can be derived from General Relativity. However, according to the Schiff conjecture[20] [**46**], by considering that the Weak Equivalence Principle[21] (WEP) applies to clocks and normal matter alike, this effect can be derived solely from Special Relativity (SR) and the WEP [**44**].

Consider an electromagnetic wave with wave number k_0 escaping from a gravitational potential. In the Schwarzschild metric and at first-order, the wave number will be shifted as the gravitational potential changes according to [**43**]

$$k = k_0\left(1 - \frac{\Delta V}{c^2}\right), \tag{216}$$

where ΔV is the change in the gravitational potential, and c is the speed of light. Notice that we have decided to write the GR in terms of the wave number because this form will be helpful in the next sections but we could have written it in terms of the frequency or wavelength as well.

As a consequence of the GR (and for transitivity as a consequence of the Equivalence Principle), a clock closer to the surface of the Earth is red-shifted compared to an identical one at a higher altitude. Thus, if a clock on the surface of the Earth with period T measures, through the use of the relation $\lambda = cT$, the wavelength of a photon to be λ, then, a (blue-shifted) clock in a spacecraft with period $T' < T$ will measure the wavelength of the same photon to be red-shifted, i.e., $\lambda' > \lambda$.

[19] The EEP states that an inertial reference frame in a (uniform) gravitational field is equivalent for all physical processes to a (suitable) uniformly accelerated reference frame free from gravitational fields [**44, 45**].

[20] According to the Schiff conjecture, every relativistic theory that satisfies the WEP necessarily satisfies the EEP.

[21] The WEP states that the inertial and gravitational masses are equivalent.

2.4 Review of the interference term

For completeness, the key results of optical interference theory relevant to the light gravimeter are summarized here [22]. Two linearly polarized monochromatic plane waves are considered.

$$\begin{aligned}\vec{E_1}(\vec{r},t) &= \vec{E_{01}}\cos(\vec{k_1}\cdot\vec{r}-\omega t+\varphi_1),\\ \vec{E_2}(\vec{r},t) &= \vec{E_{02}}\cos(\vec{k_2}\cdot\vec{r}-\omega t+\varphi_2),\end{aligned} \tag{217}$$

where ω is the angular frequency, $\vec{r}$ is the position vector, t is the time, $\vec{k_i}$ is the wave vector, φ_i is a phase offset, and $\vec{E_{0i}}$ is the electric field amplitude of the waves $i = 1, 2$. When these waves interfere at a point $\vec{r}$ at time t, the detector measures the irradiance of the superposition $\vec{E} = \vec{E_1} + \vec{E_2}$ given by the time-averaged value of the squared electric field amplitude

$$I \propto \langle \vec{E}^2 \rangle_T \,, \tag{218}$$

where the time averaged value of a function $f(t)$ is given by

$$\langle f(t)\rangle_T = \frac{1}{T}\int_{t-T/2}^{t+T/2} f(t)\,dt. \tag{219}$$

Thus, the irradiance can be written as

$$I = I_1 + I_2 + I_{12}, \tag{220}$$

where

$$\begin{aligned} I_1 &\propto \langle \vec{E_1}^{\,2} \rangle_T \,,\\ I_2 &\propto \langle \vec{E_2}^{\,2} \rangle_T \,,\\ I_{12} &\propto 2\,\langle \vec{E_1}\cdot\vec{E_2}\rangle_T \,.\end{aligned} \tag{221}$$

The term I_{12} is known as the interference term and is responsible for the appearance of the interference fringes. We can perform the integral in Eq. 219 by considering that the period of integration of the sensor T is much larger than the period of oscillation τ of the plane waves, i.e., $T \gg \tau = 2\pi/\omega$ to get

$$I_{12} \sim \vec{E_{01}}\cdot\vec{E_{02}}\cos\Delta\Phi, \tag{222}$$

where $\Delta\Phi$ is the phase difference given by

$$\Delta\Phi = \vec{k_1}\cdot\vec{r} - \vec{k_2}\cdot\vec{r} + \varphi_1 - \varphi_2. \tag{223}$$

Thus, the phase difference is given by the sum of the path length difference and the initial phase offset difference. Notice that when $\Delta\Phi = (0, \pm 2\pi, \pm 4\pi \ldots)$ rad, we have total constructive interference while when $\Delta\Phi = (\pm\pi, \pm 3\pi, \pm 5\pi \ldots)$ rad, we have total destructive interference [23]. This result is general and also holds for spherical waves

$$\begin{aligned}\vec{E_1}(\vec{r_1},t) &= \vec{E_{01}}(r_1)\exp[i(kr_1-\omega t+\varphi_1)],\\ \vec{E_2}(\vec{r_2},t) &= \vec{E_{02}}(r_2)\exp[i(kr_2-\omega t+\varphi_2)],\end{aligned} \tag{224}$$

with

$$\Phi = k(r_1 - r_2) + (\varphi_1 - \varphi_2), \tag{225}$$

where r_1 and r_2 are the radius of the spherical wavefronts overlapping at point P. Note that for the interference term to be independent of ω, the frequency ω must remain constant and identical for both waves during the integration interval (homodyne detection [**48**]), when this condition is met, the interference pattern only depends on the path length difference and the initial phase offset. Later, we will consider the case in which one of the two waves in Eq. 217 becomes redshifted during its

[22] A broader review of the phenomena of interference can be found in many textbooks, here, we follow Ref. [**47**].
[23] Additionally, we suppose that the transverse mode is the same for both waves besides its polarization and amplitude.

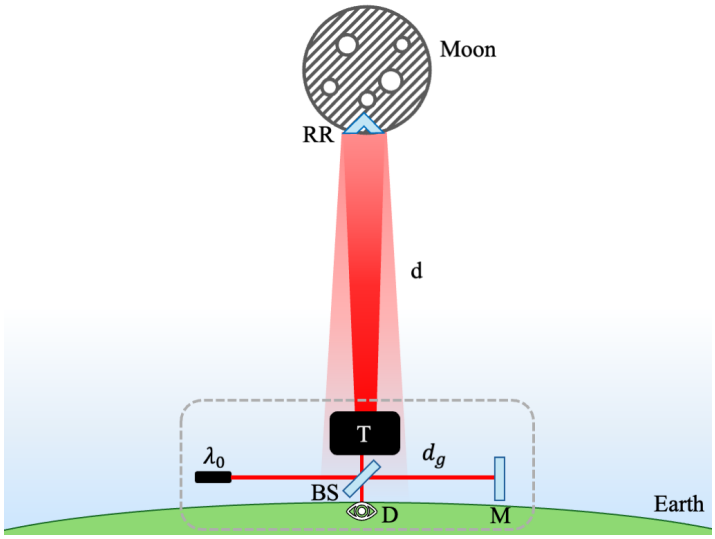

Figure 4: The experimental setup of the light gravimeter consists of a Michelson interferometer with a laser of wavelength λ_0. One arm of the interferometer stays on Earth and its optical path length is controlled, for example, through an optical cavity. The other arm of the interferometer acts as a probe of the gravitational field, extending out of the Earth's gravitational field and suffering from a GR while escaping from the potential. This beam is retroreflected after it has traveled a distance d from the beam-splitter and returns towards the Earth's surface where it interferes with the arm that did not suffer a GR and an interference pattern is measured. Notice that both beams have the same wavelength at the moment when they interfere.

propagation. In this situation, the previous conditions remain satisfied if we evaluate the interference at a spatial point where ω is the same for both waves, so that the redshift manifests only as an increase in the optical path length of one interferometer arm.

A more illuminating form of the signal measured by the detector can be obtained by considering that the waves have the same polarization with a perfect overlap and that the beam splitter is 50/50, i.e., $\vec{E_{01}} = \vec{E_{02}}$. Thus, we can re-write Eq. 220 as

$$I \propto \frac{1}{2}\left(1 + C\cos\Delta\Phi\right), \tag{226}$$

where we have introduced a constant C to quantify the contrast of the signal.

2.5 Overview of the light gravimeter

This section develops the idea of exploiting the gravitational redshift as a transduction mechanism for measuring the local gravitational acceleration g. The central novelty is the use of photons rather than massive particles as the probe. In this work, we refer to this hypothetical gravimeter as a light gravimeter in opposition to traditional gravimeters such as atomic gravimeters that use matter as the probe that measures gravity; therefore, we will refer to them as matter gravimeters. This idea is relatively recent, and to the best of our knowledge, only Ref. [**41**] has analyzed an equivalent experimental configuration for measuring gravity. Nevertheless, all the work presented in this manuscript was developed independently, without prior knowledge of that study. In any case, their research focuses on another aspect, which is the use of non-classical light to increase the sensitivity of this hypothetical gravimeter. On the other hand, our approach relies entirely on the use of classical light to understand the basic principles and limitations of the idea and the derivation of expressions that allow a straightforward comparison with matter gravimeters.

Consider the experimental setup of Fig. 4. consisting of a Michelson interferometer. A laser of wavelength λ_0, as measured on the Earth's surface, is split into two paths. One arm of length d_g is kept on the ground and its optical path length can be controlled by using an optical cavity or an optical fiber to increase the optical path length. The other arm of the interferometer, of length d,

extends out of the Earth's gravitational potential and suffers a GR. Thus, it acts as a probe of the gravitational field as it travels towards outer space. This beam is retroreflected and sent back to the Earth's surface where it interferes with the arm that did not suffer a GR. The concept of this gravimeter is in principle simpler than typical atomic gravimeters (see for example Refs. **[49, 19]**) since it consists of just a light interferometer, however, the placement of the mirrors with enough precision and in a reproducible manner lurks with being one of the hardest challenges for the implementation of this gravimeter. Now, we show that it is possible to extract the value of g using the signal at the output port of the interferometer.

The phase difference of the interference pattern measured by the detector is given by Eq. 223. However, the wavelength of the arm that travels out of the gravitational potential is not constant, furthermore, it depends on the altitude due to the GR. Therefore, we have to consider all the infinitesimal contributions to the phase. Thus, the phase difference is more generally given by

$$\Delta\Phi = \Phi_2 - \Phi_1, \tag{227}$$

with

$$\Phi_i = \int_\Gamma \vec{k}\cdot\vec{ds} + \varphi_i, \tag{228}$$

where Γ is the path of integration (given by Fermat's principle in the ray optics approximation **[48]**). By considering a plane wave in a homogeneous medium (i.e., with a constant refractive index), placed inside a gravitational field, and by taking the direction of propagation along the z-axis, the integrand $\vec{k}\cdot\vec{dr}$ becomes $k\,dz$, where k is now a function of z due to the GR. Let's label the beam that suffers the GR with the index $i = 2$ and the beam that stays on the ground at $z = 0$ with the index $i = 1$. Thus, by using Eq. 228, the phase of arm $i = 1$ will be given by

$$\Phi_1 = k_0\, d_g, \tag{229}$$

where d_g is the total distance traveled by the beam on this arm. Similarly, the phase for the other arm will be given by

$$\Phi_2 = k_0\left[\int_0^d \left(1 - \frac{\Delta V(z)}{c^2}\right) dz + \int_0^d \left(1 - \frac{\Delta V(d-z)}{c^2}\right) dz\right], \tag{230}$$

The first integral accounts for the phase accumulated while the beam goes upwards while the second integral accounts for the beam traveling downwards. Notice that for the arm on the ground ($z = 0$), the change in gravitational potential is zero and there's no contribution from the GR to the phase. On the other hand, for the upper arm, as the light travels escaping from the Earth's gravitational field, there is a contribution arising from the change in gravitational potential. The above integral can be easily simplified as

$$\Phi_2 = 2k_0 \int_0^d \left(1 - \frac{\Delta V(z)}{c^2}\right) dz. \tag{231}$$

Physically, this simplification means that the contribution to the phase is the same when the beam goes upwards than when it comes back. It is worth mentioning that k_0 could be taken out of the integral as a constant because the optical medium that we specified is homogeneous[24]. Before solving the above equation, we have to specify the change in gravitational potential $\Delta V(z)$. To get a grasp on the proposed gravimeter, let's consider the following approximation, valid for small distances, for the gravitational potential and leave a more thorough calculation for the next sections

$$\Delta V(z) = V(z) - V(0) \approx g\, z. \tag{232}$$

Note that the gravitational potential reference has been set such that wave number is simply k_0 as measured on the ground. The phase difference, after performing the integral in Eq. 231 using the approximation in Eq. 232 is given by

$$\Delta\Phi = 2k_0\Big(d - d_g\Big) + \Delta\Phi_g, \tag{233}$$

[24]Later, we will include the effect of the change in the refractive index.

where we have considered equal initial phase offsets ($\varphi_1 = \varphi_2$), and we have defined

$$\Delta\Phi_g = -k_0 g T^2. \tag{234}$$

with $T \equiv d/c$. Notice that we can control the optical path of the arm that stays on the ground by changing d_g, thus, we could cancel out the first term in Eq. 233 and get $\Delta\Phi = \Delta\Phi_g$. In this way, we could use the interference pattern, measured by the detector, to extract the value of g. Now, let's analyze the achievable fractional precision with this result. The fringe shift is linearly proportional to g, consequently, the uncertainty in the measurement of the phase difference ($\sigma_{_{\Delta\Phi}}$) is also directly proportional to the uncertainty in the measurement of the local acceleration of gravity (σ_g). Thus, in terms of fractional precision, we have that

$$\frac{\Delta\Phi}{\sigma_{_{\Delta\Phi}}} = \frac{g}{\sigma_g}. \tag{235}$$

By using Eq. 226, we can define signal-to-noise-ratio (SNR) of the interferometry signal, from which the value of g is extracted, as the ratio between the contrast of the fringes and the uncertainty on the slope of the fringe, i.e.,

$$SNR = \frac{C/2}{\sigma_{I_{12}}}, \tag{236}$$

where

$$\sigma_{I_{12}} = \frac{C}{2} |\sin\Delta\Phi| \sigma_{_{\Delta\Phi}}. \tag{237}$$

Since the change in the slope of the signal is maximal at the middle fringe, i.e., when $\Delta\Phi = \pi/2\,\text{rad}$, we focus at this point so the sensitivity to changes in the measured value of g is maximal as well, thus, we have that

$$SNR = \frac{1}{\sigma_{_{\Delta\Phi}}}. \tag{238}$$

Thus, the fractional precision in the measurement of g is given by

$$\frac{\sigma_g}{g} = \frac{1}{\Delta\Phi\, SNR}.$$

Therefore, the fractional precision of the measurement increases as the phase difference $\Delta\Phi$ increases. Nonetheless, in reality, the only component that contains information about g is $\Delta\Phi_g$. This is the term that has to be maximized to increase the sensitivity of the measurement, i.e.,

$$\frac{\sigma_g}{g} = \frac{1}{\Delta\Phi_g\, SNR}. \tag{239}$$

Since the speed of light appears squared in the denominator of Eq. 234, the value of $\Delta\Phi_g$ is in general small, except for very long distances or very energetic beams [25]. This is the most important drawback of this hypothetical gravimeter. As an example, for $\lambda_0 = 650\,\text{nm}$ and $d \sim 10^8\,\text{m}$ (average distance from the Earth to the Moon), we get that $\Delta\Phi_g \sim 10^7\,\text{rad}$. Thus, by considering a $SNR = 100$, we get a sensitivity of about $\sigma_g/g \sim 10^{-9}$ in a single-shot measurement. This precision can be further improved by leveraging the fact that the uncertainty improves as the square root of the number of measurements [**39**], thus, by considering a detector with a bandwidth of 1 MHz the precision could be enhanced by a factor of 1000 in just a second. This is another of the advantages of the light gravimeter versus matter gravimeters such as atomic gravimeters whose detection bandwidth is of the order of 1 Hz [**8**], which is much slower than the bandwidth of the detectors required by the light gravimeter. For comparison, the accuracy of portable atomic gravimeters is usually at the 10^{-9} level after tens of minutes of averaging [**8**]. The sensitivity of the light gravimeter looks promising but we have to remember that the assumptions used to get the result in Eq. 234 were not too realistic. Thus, in

[25] We will see later that the equivalent to very energetic beams in matter atomic gravimeters is the increment of the momentum-space splitting.

the next sections, we refine our calculation of the gravimetry signal. Our goal will be to get a better estimation of the order of magnitude of the phase and to consider additional corrections.

Finally, it is important to mention that the values of k_0 and d have to be known with a precision at least equal to the precision we expect for the measurement of g otherwise the precision of the measurement will be limited by them. The value of k_0 can be determined with the precision required. However, determining the value of d is more challenging. A long vertical arm is needed for high sensitivity. A possible solution could be to use lunar laser ranging (LLR) [**50, 51**] to determine the distance between the gravimeter and the retroreflectors. This could be potentially achieved by using a retro-reflecting mirror on the Moon (or those planned for the near future that operate in the visible and infrared [**51**]) or reflecting off a geostationary satellite ($d \sim 10^7$ m), with the obvious complications of aligning an interferometer under those conditions. As an alternative, a Mach-Zehnder interferometer [**41**] could be used to have the detection in the satellite and avoid the retro-reflection back to Earth [**42**] at the cost of a much-reduced distance. Advancements to extend the length of quantum communication channels have successfully reached link distances between ground-based stations and satellites equipped with retroreflectors in the order of $d \sim 10^6$ m [**52, 53, 54**] and even with $d \sim 20000$ km [**55**]. The current single-shot precision of LLR is in the order of 1 cm (which gives a fractional precision of about 10^{-11}), and a future method is expected to improve it 200 times [**50, 51**]. Another option to avoid having to perform complex LLR measurements is to operate in a relative gravimeter configuration such that the actual value of d is not relevant and only changes in d would need to be determined at every measurement. This could help to compete with portable atom gravimeters [**8, 10**].

2.6 Corrections to the gravitational potential

In the last section, we saw that to solve the integral of Eq. 231, we need to know $\Delta V(z)$. The computation of this function is not trivial. In general, one must take into account the contribution stemming from other objects in the solar system such as planets, thus, it is imperative to know their position, shape, and mass density. Fortunately, as we will show, it turns out that the most important contributions to the gravitational potential, for the distances and regions considered in this work, are due to the Moon and the Sun. Thus, in this section, we refine our calculation of $\Delta V(z)$ by using a toy model that only considers the gravitational potential generated by the Earth-Moon-Sun system. This model is suitable for our purposes since we are only interested in the order of magnitude of the potential.

2.6.1 Correction due to the shape of the Earth

A correct calculation of the Earth's gravitational potential must take into account its shape. This can be achieved by remembering that Newton's law of universal gravitation

$$F = G\frac{M_1 M_2}{|\vec{r_1} - \vec{r_2}|^3}(\vec{r_1} - \vec{r_2}), \tag{240}$$

where $\vec{r_i}$ is the position vector of the mass M_i, is an inverse-square law. Thus, in an region free of masses, the gravitational potential must be a solution to Laplace's equation [**56**]

$$\nabla^2 V = 0. \tag{241}$$

The most general solution can be written in spherical coordinates as

$$V(r,\theta,\varphi) = \sum_{l=0}^{\infty}\sum_{m=-l}^{l} A_{lm} r^{-(l+1)} Y_{lm}(\theta,\varphi), \tag{242}$$

where θ is the co-latitude, φ is the longitude, Y_{lm} are the spherical harmonics and A_{lm} are constants. The value of the constants A_{lm} cannot be determined analytically and they have to be obtained by measurements of the perturbation of the orbits of artificial satellites. Usually, these satellites sample, in the same way, all the longitudes, i.e., they cannot reveal variations with longitude [**57**]. As a consequence, the solution can be re-written by considering azimuthal symmetry as

$$V(r,\theta) = \sum_{l=0}^{\infty} A_l r^{-(l+1)} P_l(\cos\theta), \tag{243}$$

where $P_l(\cos\theta)$ are the Legendre polynomials. The first term of this expansion goes like $1/r$ and has to be the potential of a point mass, the rest of the terms are corrections due to the Earth's oblateness. Therefore, the potential can be written as **[58, 59, 60]**

$$V(r,\theta) = \frac{GM_e}{R_e}\left[\frac{R_e}{r} - \sum_{l=2}^{\infty} A_l \left(\frac{R_e}{r}\right)^{l+1} P_l(\cos\theta)\right], \tag{244}$$

where M_e is the Earth's mass and R_e is the Earth's equatorial radius. Notice that the term $l = 1$ is zero because we considered that the equatorial plane passes through the center of mass of the Earth. To understand this, notice that when the origin of the coordinate system and the center of mass coincide, the potential cannot be symmetric in θ because the distribution of mass is not uniform[26]. Thus, since $P_1(\cos\theta) = \cos\theta$, the term $l = 1$ must be zero. Several of the first coefficients A_l have been measured to confirm the oblateness of the Earth **[61, 62, 63]**.

The result of Eq. 244 is general and can be used to describe the potential of the Moon or any other planet. However, since our interest is to get a correction in the order of magnitude of the calculation done in Section 2.5, for the sake of simplicity, we will only consider the first term of Eq. 244. This term corresponds to the potential due to a point mass or to a distribution of mass with spherical symmetry. Thus, when considering the contribution to the potential due to the Earth, Moon, Sun, and other planets, we will consider that they are perfect spheres with homogeneous mass densities.

2.6.2 Validity of the approximation gz at long distances

In Section 2.5, we approximated the change in potential using Eq. 232. However, this approximation is expected to be valid only for distances close to the surface of the Earth. Thus, we have to determine how bad our first approximation was. In this section, we compute the error obtained in the calculation of the gravitational redshift by considering this approximation and show that it is not valid for the distances needed by the light gravimeter. Later, in Section 2.6.6, we determine the error in the phase obtained by computing the integral of Eq. 231 using the approximation $\Delta V = g\,z$.

By considering the first term in Eq. 244, the change in potential between a point on the surface of the Earth and a point at a distance z above it is given by

$$\Delta V = -GM_e\left(\frac{1}{R_e + z} - \frac{1}{R_e}\right). \tag{245}$$

From this result, the approximation in Eq. 232 can be obtained by taking $(R_e + z)R_e \approx R_e^2$ and using the definition $g \equiv GM_e/R_e^2$. For future reference, we write here the approximations in the case of short and long distances at second order

$$\Delta V \approx \begin{cases} gR_e - gR_e^2/z, & \text{for } z \gg R_e \\ gz - gz^2/R_e, & \text{for } z \ll R_e \end{cases} \tag{246}$$

The relative error of using Eq. 232 instead of Eq. 245 is given by

$$\varepsilon_r = z/R_e, \tag{247}$$

where the average radius of the Earth can be taken to be $R_e \approx 6371\text{km}$ **[64]**. For a distance $z = 100\,\text{m}$, the relative error in the calculation of the change in potential is just $\varepsilon_r = 0.0015\%$, however, for $z = 10^7\,\text{m}$ the relative error scales up to $\varepsilon_r = 150\%$. Therefore, the approximation in Eq. 232 is not valid for long distances from the Earth. Notice, that since the change in wavelength due to the gravitational redshift is proportional to the change in potential (Eq. 216), then the relative error computed with Eq. 247 is also the relative error in the calculation of the gravitational redshift obtained when using the approximation of Eq. 232 instead of Eq. 245.

2.6.3 Contribution of the Moon and the Sun

A complete calculation of the function ΔV must take into account not only the contribution of the Earth (Eq. 244) but also the contribution from other objects in the solar system. The most important

[26] This means that the center of mass is different from the center of gravity.

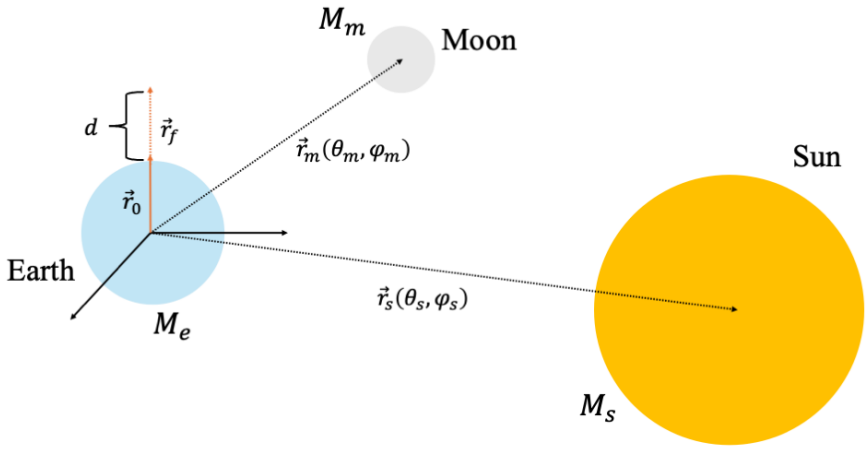

Figure 5: Earth-Moon-Sun system (not at scale) used to compute the change in gravitational potential between an initial point on the surface of the Earth ($\vec{R_e}$) and a final point ($\vec{r_f}$). We model the Earth, Moon, and Sun as perfect spheres with homogeneous mass density and use spherical coordinates to describe their position. Notice that the center of coordinates is at the center of the Earth and the system has azimuthal symmetry since both $\vec{R_e}$ and $\vec{r_f}$ are aligned along the z-axis so that $|\vec{R_e}| = R_e$ and $|\vec{r_f}| = z$. The position of the Moon and the Sun is indicated by the vectors $\vec{r_m}(\theta_m, \varphi_m)$ and $\vec{r_s}(\theta_s, \varphi_s)$ respectively.

contributions to the gravitational potential at regions close to the Earth are the Sun (due to its massive mass) and the Moon (due to its close distance to the Earth). The rest of the planets in the solar system, as we will show in the next section, do not contribute significantly to the potential. We are only interested in knowing the order of magnitude of the correction to the phase difference (Eq. 233) by considering the system Earth-Moon-Sun, thus, it will suffice to use the toy model shown in Fig. 5. In this model, we consider that the Earth, the Moon, and the Sun are perfect spheres with homogeneous mass density so their potential in regions free of mass can be described by the first term of Eq. 244 with M_e substituted by the corresponding mass of the Moon M_m or the mass of the Sun M_s. Thus, the change in potential due to these bodies is given by

$$\Delta V = V_f - V_0, \tag{248}$$

where

$$V_0 = -G\left(\frac{M_e}{|\vec{R_e}|} - \frac{M_m}{|\vec{r_m} - \vec{R_e}|} - \frac{M_s}{|\vec{r_s} - \vec{R_e}|}\right), \tag{249}$$

and

$$V_f = -G\left(\frac{M_e}{|\vec{r_f}|} - \frac{M_m}{|\vec{r_m} - \vec{r_f}|} - \frac{M_s}{|\vec{r_s} - \vec{r_f}|}\right), \tag{250}$$

where the positions of the Moon and the Sun are described by the vectors $\vec{r_m}(\theta_m, \varphi_m)$ and $\vec{r_s}(\theta_m, \varphi_m)$ respectively. Note that, as before, the potential reference V_0 is taken with respect to the potential on the surface of the Earth. For our purposes, it suffices to consider that r_m and r_s are the average distance from the Earth to the Moon and to the Sun respectively, and that $|R_e|$ is the average Earth radius. The z-axis points to the zenith and is aligned with the direction of propagation of the light beam so the system has azimuthal symmetry and the distances between the position vectors are simplified to

$$\begin{aligned}
|\vec{r_m} - \vec{R_e}| &= \left(r_m^2 + R_e^2 - 2r_m R_e \cos\theta_m\right)^{1/2}, \\
|\vec{r_s} - \vec{R_e}| &= \left(r_s^2 + R_e^2 - 2r_s R_e \cos\theta_s\right)^{1/2}, \\
|\vec{r_m} - \vec{r_f}| &= \left(r_m^2 + r_f^2 - 2r_m r_f \cos\theta_m\right)^{1/2}, \\
|\vec{r_s} - \vec{r_f}| &= \left(r_s^2 + r_f^2 - 2r_s r_f \cos\theta_s\right)^{1/2}.
\end{aligned} \tag{251}$$

To further simplify the next calculations, we will consider that $\theta_m = \theta_s = 0$ and restrict the distance d to the interval $d \in (R_e, r_m)$. In this way, the change in potential can be written as

$$\Delta V = \Delta V_e + \Delta V_m + \Delta V_s, \tag{252}$$

where

$$\begin{aligned}
\Delta V_e &= -GM_e\left(\frac{1}{R_e + z} - \frac{1}{R_e}\right) = -g\left(\frac{R_e^2}{R_e + z} - R_e\right), \\
\Delta V_m &= -GM_m\left(\frac{1}{r_m - R_e - z} - \frac{1}{r_m - R_e}\right), \\
\Delta V_s &= -GM_s\left(\frac{1}{r_s - R_e - z} - \frac{1}{r_s - R_e}\right).
\end{aligned} \tag{253}$$

Now, we can use this result to estimate the contribution to the change in potential for different values of z. Table 2 shows the change in the gravitational potential for the Earth-Moon-Sun system for different values of z. Notice that the contribution to the change in gravitational potential coming from the Earth is always larger than the contributions from the Moon and the Sun for the distances considered. Their contribution is small for distances close to the Earth's surface but becomes significant for larger distances. Furthermore, the contribution from the Sun is larger than the contribution from the Moon except for distances close to the Moon. These are the distances that we would need to operate a light gravimeter, thus, this calculation shows that we cannot ignore the contribution coming from the Sun and Moon.

Table 2: Change in gravitational potential for the Earth-Moon-Sun system for different distances d. Although the fractional contribution of ΔV_m and ΔV_s is not negligible for large distances, notice that, for measurement purposes, their fluctuations are more relevant and since during the experiment these values will not change considerably then their contribution to the final result can be easily subtracted. The purpose of this table (and the current section) is simply to illustrate how much each body contributes to the gravitational potential experienced by a photon in the light gravimeter and to see that our initial estimation of ΔV is not valid for long distances (although this error can be easily subtracted from the measurement at the end of the experiment as was already mentioned).

$z(m)$	ΔV_e (J/kg)	ΔV_m (J/kg)	ΔV_s (J/kg)	ΔV (J/kg)
100	980	-3.3×10^{-3}	-5.5×10^{-1}	979
10^7	3.7×10^7	-3.4×10^2	-5.5×10^4	3.7×10^7
3×10^8	6×10^7	-4.8×10^4	-1.6×10^6	5.8×10^7

2.6.4 Contribution of other celestial bodies

In the last section, we saw that it is imperative to consider the contribution of the Moon and the Sun when calculating the change in gravitational potential for the distances under consideration. Aside from the Sun and Moon, the other objects in the solar system that may contribute significantly to the gravitational potential due to their mass are the planets. We can estimate their contribution to the change in the gravitational potential by using the same assumptions used for the Moon and the Sun, i.e., they are perfect spheres with homogeneous mass density and their position vector is aligned with the z-axis. In this way, the individual contribution of every planet will be given by

$$\Delta V_p = -GM_p\left(\frac{1}{r_p - R_e - z} - \frac{1}{r_p - R_e}\right), \tag{254}$$

where M_p is the mass of the planet and r_p is the average distance between the Earth and the planet. Table 3 shows the contribution of solar system planets to the change in gravitational potential. Notice that their contribution is much smaller than the contribution from the Sun or the Moon. Thus, it is justified to neglect their contribution in our next calculations[27].

[27] In fact, what matters are the fluctuations (variations) in these values. If the contribution from the Sun, Moon, or any other planet is known, then, we can always correct our measurement to isolate the desired effect. Furthermore, we can

Table 3: Contributions to the change in gravitational potential (ΔV) for different bodies in the solar system. We considered $d = r_E - r_M - r_{M-E} \approx 3.76\times\ 10^8$ m, where r_E is the average Earth radius, r_M is the average Moon radius, and r_{M-E} is the average Moon-Earth distance; r_{avg} is the average distance of the body to the Earth. Notice that we had to subtract r_M and r_E because r_{M-E} is the average center-to-center distance not the surface-to-surface distance which is the correct distance to be considered since in this calculation the upper arm of the interferometer goes from a point at the surface of the Earth to a point on the surface of the Moon. Data used in this calculation was consulted from **[65]**. As was pointed out in the previous section, these contributions to the gravitational potential are not expected to change considerably during the experiment so their contribution to the final measurement can be easily subtracted from the final result. They are studied here just to illustrate how much they contribute to the gravitational potential seen by a photon traveling in the light gravimeter.

Body	*mass* (kg)	r_{avg} (m)	ΔV (J kg^{-1})
Earth	5.97×10^{24}	-	6.14×10^{7}
Moon	7.34×10^{22}	3.85×10^{8}	-2.81×10^{6}
Sun	1.98×10^{30}	1.49×10^{11}	-2.24×10^{6}
Mercury	3.30×10^{23}	1.55×10^{11}	-0.34
Venus	4.86×10^{24}	1.70×10^{11}	-4.23
Mars	6.41×10^{23}	2.54×10^{11}	-0.25
Jupiter	1.89×10^{27}	7.86×10^{11}	-76.99
Saturn	5.68×10^{26}	1.43×10^{12}	-6.98
Uranus	8.68×10^{25}	2.87×10^{12}	-0.26
Neptune	1.02×10^{26}	4.50×10^{12}	-0.12

2.6.5 Phase of the light gravimeter for the Earth-Moon-Sun system

In the last section, we saw that to calculate the change in the gravitational potential (ΔV), we can neglect the contribution from the planets, but not from the Sun and, especially from the Moon when considering placing retro-reflectors there. Thus, in this section, we refine our calculation of the integral of Eq. 231 to get the phase difference from which we can extract the value of g. First, notice that the change in gravitational potential for the Earth-Moon-Sun system (Eq. 252) can be written as

$$\Delta V = -\left[g\left(\frac{R_e^2}{R_e+z}\right) + \frac{GM_m}{r_m - R_e - z} + \frac{GM_s}{r_s - R_e - z}\right] + V', \tag{255}$$

where

$$V' = g\,R_e + \frac{GM_m}{r_m - R_e} + \frac{GM_s}{r_s - R_e}. \tag{256}$$

Notice that the term V' does not have any dependence on the distance z. Thus, by substituting this result into Eq. 216, we get

$$k = k_0\left[1 + \frac{1}{c^2}\left(\frac{gR_e^2}{R_e+z} + \frac{GM_m}{r_m - R_e - z} + \frac{GM_s}{r_s - R_e - z} - V'\right)\right]. \tag{257}$$

In this way, the integral of Eq. 231 can be easily solved to get

$$\Delta\Phi = k_0\left\{\frac{2}{c^2}\left[d\big(c^2 - V'\big) + g\,R_e^2 \ln\left(\frac{d+R_e}{R_e}\right) + GM_m \ln\left(\frac{R_e - r_m}{d + R_e - r_m}\right) + GM_s \ln\left(\frac{R_e - r_s}{d + R_e - r_s}\right)\right] - 2d_g\right\}. \tag{258}$$

Notice that this result can be easily generalized to consider the contribution of the planets (and other objects in the solar system) by using Eq. 254

$$\Delta\Phi = k_0\left\{\frac{2}{c^2}\left[d\big(c^2 - V'\big) + g\,R_e^2 \ln\left(\frac{d+R_e}{R_e}\right) + \frac{c^2}{2}\sum_i R_{s,i} \ln\left(\frac{R_e - r_i}{d + R_e - r_i}\right)\right] - 2d_g\right\}, \tag{259}$$

expect that the variation over time of the contribution to the gravitational potential will be smaller the farther the planet is. Our calculation considers average values but an estimation of the order of magnitude of these fluctuations can be obtained by considering the maximum and minimum distances a planet can be from the Earth.

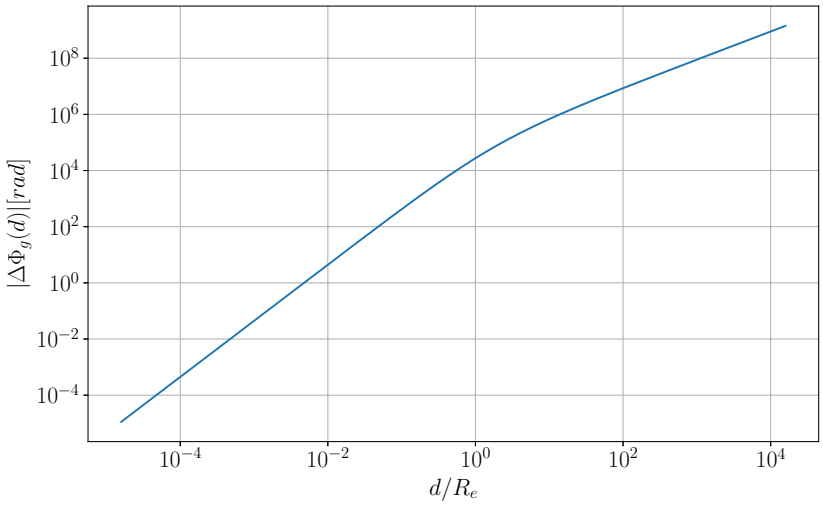

Figure 6: Dependency of the gravitational phase (Eq. 263) as a function of the arm distance d. There is a change from a quadratic to a linear dependence at a distance of $d \simeq R_e$. We considered $\lambda = 650$ nm, $g = 9.8\,\mathrm{m\,s^{-2}}$, and normalized the distance in the horizontal axis.

where the index i represents the i-th solar system object to be considered in the calculation, r_i is its average distance from the Earth, $R_{s,i} \equiv 2GM_i/c^2$ is its Schwarzschild radius and M_i its mass. Nonetheless, as shown in Section 2.6.4, the most important contributions are due to the Moon and Sun, thus, we will continue working with Eq. 258. To get a better understanding of this result, we need to split the contributions stemming from the different actors as follows

$$\Delta\Phi = \Delta\Phi_d + \Delta\Phi_g + \Delta\Phi_{ms}, \tag{260}$$

where $\Delta\Phi_d$ is the term corresponding to the difference in optical path length given by

$$\Delta\Phi_d = 2k_0\big(d - d_g\big), \tag{261}$$

$\Delta\Phi_{ms}$ is the contribution due to the change in gravitational potential attributable to the Moon and the Sun given by

$$\Delta\Phi_{ms} = \frac{2k_0G}{c^2}\left[-d\left(\frac{M_m}{r_m - R_e} + \frac{M_s}{r_s - R_e}\right) + M_m \ln\left(\frac{R_e - r_m}{d + R_e - r_m}\right) + M_s \ln\left(\frac{R_e - r_s}{d + R_e - r_s}\right)\right], \tag{262}$$

and $\Delta\Phi_g$ is the term attributable to g given by

$$\Delta\Phi_g = -2k_0 g\Theta^2, \tag{263}$$

where Θ is a parameter with units of time given by

$$\Theta = \sqrt{\frac{R_e}{c^2}\left[-d + R_e \ln\left(\frac{d + R_e}{R_e}\right)\right]}. \tag{264}$$

A plot of $\Delta\Phi_g$ against d is shown in Fig. 6. Notice that for short distances, the phase in Eq. 263 grows quadratically with d, however, for long distances, it grows linearly. This behavior will be better understood when we analyze different approximations in the next section.

2.6.6 Validity of the approximation for short distances

In section 2.5, we analyzed the light gravimeter using the approximation of the potential valid for short distances. The term of interest is that due to gravity, therefore, we must compare Eqs. 234 and 263.

By considering that Eq. 263 gives the actual phase shift due to the value of g, then the relative error of using Eq. 234 is given by

$$\varepsilon_r = 1 - \frac{d^2/2R_e}{d - R_e \ln\left[(d+R_e)/R_e\right]} \tag{265}$$

Figure 7 shows the relative error in Eq. 265 for different values of d. Notice that as expected, the result obtained in Eq. 234 is only valid for low heights (below $d \sim 10^6$). The gravimetry signal in Eq. 263 is one order of magnitude smaller than that calculated in Section 2.5.

2.6.7 Order of magnitude of the different contributions to the phase shift

Figure 8 shows the order of magnitude of the contributions in Eq. 260. Notice that the term due to the path length ($\Delta\Phi_d$) has the largest contribution for all distances, however, in the phase difference (Eq. 260), the term $k_0 d_g$ (accumulated in the horizontal arm) can always be used to cancel it out. On the other hand, the term $\Delta\Phi_{ms}$ gives the smallest contribution to the phase shift. The term of interest for our purposes is $\Delta\Phi_g$ and as was stated previously, it becomes relevant only for very long distances. For reference, $d \sim 10^7$ m is approximately the distance from the surface of the Earth to a satellite in a geostationary orbit, and $d \sim 10^8$ m is the average distance from the Earth to the Moon. The small value of $\Delta\Phi_g$ with respect to $\Delta\Phi_d$ is because the GR is a correction in the wave vector given by the perturbative term $\Delta V/c^2$ as can be seen from Eq. 216 or from taking the quotient between Eqs. 234 and 261, that is,

$$\frac{\Delta\Phi_g}{\Delta\Phi_d} \propto -\frac{gd}{c^2}, \tag{266}$$

where $c = d/T$ was used alongside $\Delta V \approx gd$ which, as was shown before, is valid for $d \ll R_e$.

According to Eq. 263, two parameters can be controlled experimentally to increase the gravimeter signal, the beam wavelength, and the length of the upper arm. Due to the large distances required to operate the light gravimeter, it is natural to think of using a satellite or even the Moon to put a mirror (as shown in Fig. 4) to redirect the light beam back. A second alternative is to use one of the retroreflectors placed on the surface of the Moon. Nonetheless, the existing lunar retroreflectors and those planned for the near future are designed to operate in the visible and IR spectrum [**51**], thus, the beam wavelength would be constrained to this range. Notice that the wavelength of the light beam is particularly important because the gravimetry signal in Eq. 263 is inversely proportional to the beam wavelength, therefore, a light gravimeter operating with a smaller wavelength would obtain a larger gravimetry signal and consequently a better precision in a single-shot measurement. Nonetheless, the disadvantage of choosing another regime of the electromagnetic spectrum such as x or gamma rays is the increasing complexity of the type of optical components needed to operate an interferometer using those wavelengths. In the case of gamma rays, Mössbauer spectroscopy was successfully used by Pound and Rebka (1960) and later by Pound and Snider (1965) in a 22-meter-long tower to quantify the GR by measuring the difference in photon frequency at different heights [**66, 67, 68**].

Finally, it is worth noticing that the experimental setup under consideration (Fig. 4) is not the only possible arrangement that could be used to build the light gravimeter, an alternative is to send the light beam toward a satellite where the detection can take place without needing to return the beam by using Mach Zender interferometry [**42, 41**].

2.6.8 Behavior of the phase with the distance

The result in Eq. 258 is a general result for the Earth-Moon-Sun system under the assumptions stated in Section 2.6.3. However, it is noteworthy to consider a few approximations of this result to get more insights. Let us write the general result in Eq. 258 for the case when there is no Moon and Sun contribution, that is, focusing only on the contribution from the earth

$$\Delta\Phi = k_0\left\{\frac{2}{c^2}\left[d\left(c^2 - gR_e\right) + g\,R_e^2 \ln\left(\frac{d+R_e}{R_e}\right) + \right] - 2d_g\right\}. \tag{267}$$

As expected, this result is simply the contribution coming from Eqs. 261 and 263. By considering that $d/R_e \ll 1$, the change in gravitational potential is given by Eq. 232. This approximation is suitable for

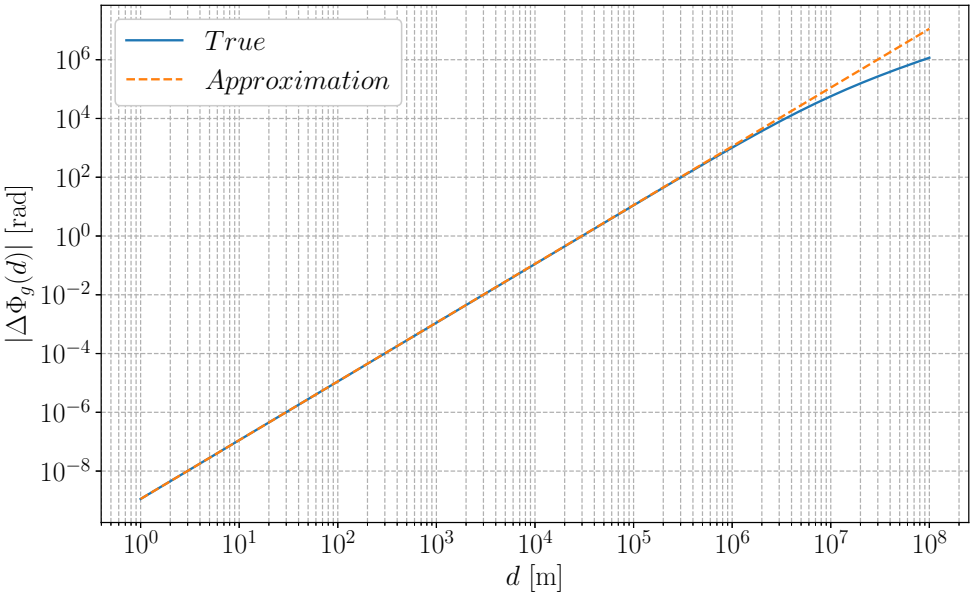

(a) $|\Delta\Phi_g(d)|$ and its approximation.

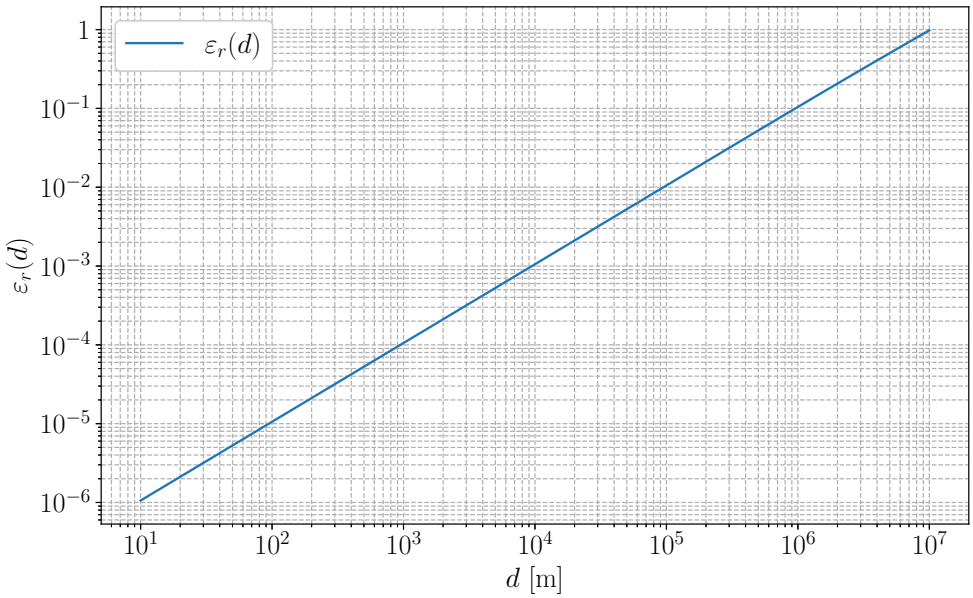

(b) Relative error $\varepsilon_r(d)$.

Figure 7: Relative error of the phase shift in Eq. 234 by considering that it is an approximation and that the result of Eq. 263 is the true gravimetry signal. The values were obtained by considering that $\lambda_0 = 650\,\text{nm}$.

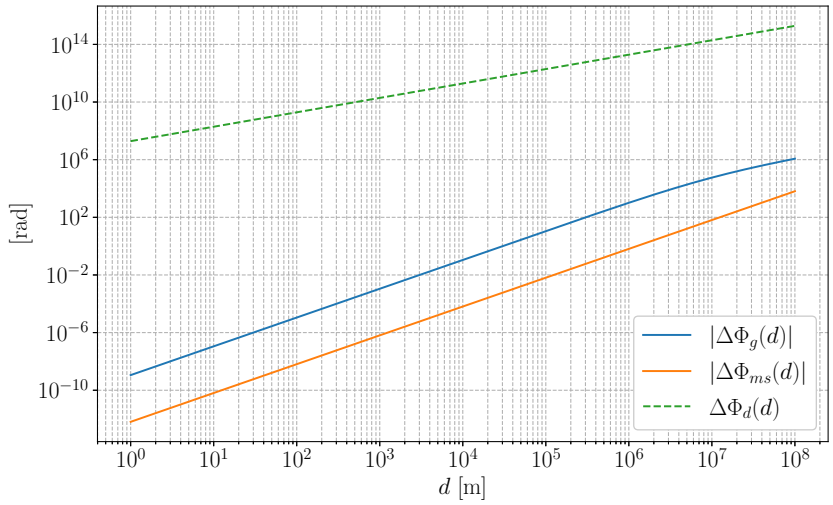

Figure 8: Order of magnitude of the different contributions in Eq. 260 for $\lambda_0 = 650\,\text{nm}$. In this plot, the term $\Delta\Phi_d$ is not taking into account the contribution from the horizontal arm ($2k_0 d_g$).

short distances and gives the quadratic behavior that can be appreciated in Fig. 6. The value of g can be obtained from the shift due to the GR given by Eq. 234, i.e.

$$\Delta\Phi_g = -k_0 g\left(\frac{d}{c}\right)^2. \tag{268}$$

This phase shift resembles exactly the phase shift seen in traditional atomic gravimetry [**17**] and is one of our main results. We'll discuss the connection between light and matter-based gravimetry with much more detail in section 2.9. Equation 268 also has the form of the result reported in Ref. [**42**]

$$\Delta\Phi_g \sim (1+\alpha)k_0 g\frac{dl}{c^2}, \tag{269}$$

where l is the horizontal length of an optical delay introduced by using optical fibers in a Mach-Zender interferometer configuration that allows the measurement in the receiving node. The parameter α is introduced to test the validity of the universality of gravitational redshift, this parameter has a value equal to zero for general relativity. Similarly, our conceptual experiment shown in Fig. 4, could be used to test the value of the parameter α by introducing this parameter in the general result of Eq. 263, i.e.,

$$\Delta\Phi_g = 2(1+\alpha)k_0 g\Theta^2. \tag{270}$$

Thus, the results of our analysis are equally applicable to both cases, the measurement of g or α. On the other hand, by considering that $d/R_e \gg 1$. The gravitational phase becomes

$$\Delta\Phi_g = -\frac{k_0 g R_e}{c}\left(\frac{2d}{c}\right). \tag{271}$$

This result explains the linear behavior shown in Fig. 6 for long distances. For future reference, we write here the approximations for Eq. 267 in the case of short and long distances at second order

$$\Delta\Phi \approx \begin{cases} 2k_0(d-d_g) - \dfrac{2k_0}{c^2}dR_e\left(g\left[1-(R_e/d)\ln(d/R_e)\right]\right), & \text{for } d \gg R_e \\ 2k_0(d-d_g) - \dfrac{2k_0}{c^2}dR_e\left(g\left[(1/2)(d/R_e)-(1/3)(d/R_e)^2\right]\right), & \text{for } d \ll R_e. \end{cases} \tag{272}$$

Before finishing this section, it is important to mention another fact about the results in Eqs. 268 and 271. As can be seen, there is a change in the scaling of $\Delta\Phi_g$ from a quadratic to a linear dependency with the vertical distance d. This change in scaling arises because d (the length of the interferometer's vertical arm) affects the gravitational phase in two distinct ways. First, increasing d increases the propagation

time, allowing more phase to accumulate. Second, increasing d also changes the gravitational potential experienced along the path, adding an additional phase shift. At sufficiently large d, the difference in gravitational potential saturates: it effectively stops growing, so its contribution to the phase becomes negligible. Consequently, for small d the phase receives both contributions and scales quadratically with d (or with t, since $d = cT$), while at large d only the time-accumulation contribution remains.

2.6.9 Effective point of measurement

Since the length of the vertical arm required to operate the light gravimeter is enormous, it is natural to ask at which location corresponds the local gravity that is being measured. To calculate the effective point of measurement, we need to isolate the effect of gravity along the integration path. To do so, suppose that, in some way, we send all the light in the upper arm instantaneously to the end of the path and let it stay there for some time $T = \tilde{d}/c$ such that Eq. 231 becomes

$$\tilde{\Phi}_2 = -\frac{2k_0}{c^2}\Delta V \tilde{d}. \tag{273}$$

By using Eq. 246, we get

$$\tilde{\Phi}_2 \approx \begin{cases} -\dfrac{2k_0}{c^2}\tilde{d}\left(gR_e - g\dfrac{R_e^2}{\tilde{d}}\right), & \text{for } \tilde{d} \gg R_e \\ -\dfrac{2k_0}{c^2}\tilde{d}\left(g\tilde{d} - g\dfrac{\tilde{d}^2}{R_e}\right), & \text{for } \tilde{d} \ll R_e. \end{cases} \tag{274}$$

Now, by equating the above result with the corresponding gravitational term of the vertical arm in Eq. 272 and solve for $\tilde{d}/d$, we get

$$\tilde{d}/d \approx \begin{cases} \dfrac{1}{\ln(d/R_e)}, & \text{for } d \gg R_e \\ 1/2, & \text{for } d \ll R_e. \end{cases} \tag{275}$$

Notice that, for short distances, the effective point where the local gravity is being measured is at the middle of the vertical arm. In the case of $d \sim 10^8$, the limit $d \gg R_e$ applies and $\tilde{d}/d \sim 0.25$, that is, the effective point of measurement lies approximately at a quarter the distance from the Earth to the end of the vertical arm. Finally, it is noteworthy to recall that the same systematic, of measuring an average value of g over the trajectory, is present in atomic gravimetry [**17**], however, it's effect is much less prominent since the vacuum chamber can only be a few meters long.

2.7 Atmospheric considerations

In the last section, we focused on enhancing the result obtained in Section 2.5 by introducing corrections to the way the change in gravitational potential was calculated. In this section, we consider corrections to the phase shift due to the optical medium, and general atmospheric considerations for the light gravimeter.

2.7.1 Phase shift due to the change in the air refractive index

In the last sections, we have seen that the light gravimeter requires the use of large distances to operate. As can be seen from Eq. 231, there are two ways to increase the gravimetric signal. One could think in increasing the factor $k_0\,\Delta V(z)$ by increasing the wavenumber. Alternatively, one can increase the arm length—or equivalently, the measurement time—since $T = d/c$. Because manipulating γ or x-ray beams is rather complicated, it turns out that, the most practical strategy for improving the signal is to increase the interferometer's measurement time[28]. However, achieving a significant phase shift would require extending the vertical arm to such a length that the light beam would need to propagate through the atmosphere over a round-trip path.[29]. This introduces an important challenge since the density of the atmosphere changes as the altitude, temperature, pressure, and humidity vary. This

[28]This also has the side effect of increasing the change in gravitational potential $\Delta V(z)$. However, for sufficiently large distances, the contribution from this potential difference becomes negligible, and the gravimetric signal grows only linearly (see Eq. 271 and the subsequent discussion).

[29]This problem only occurs if the light gravimeter is operated in a planet with a dense atmosphere.

change in the density of the air produces a change in the refractive index so there is an additional phase shift in the phase measured. In fact, the principal source of error in lunar laser ranging is the atmosphere [**50**]. Thus, we can expect that something similar will happen in this case. In this section, we calculate the order of magnitude of the phase shift caused by the change in refractive index along the atmosphere.

If the wavenumber of an electromagnetic wave in the vacuum is k_0, then, its wavenumber in an optical medium with refractive index n is given by [**47**]

$$k = k_0 n. \tag{276}$$

The refractive index of a light beam traversing the atmosphere has a dependence on the altitude. Thus, from Eq. 228, the phase of the arm of the interferometer that goes upwards (i=2) must be written (without considering the effect of the GR) as

$$\Phi_2 = k_0 \int n(s) ds. \tag{277}$$

Notice that the integral is the definition of optical pathlength [**48**], this is why the phase accumulated by a light beam is interpreted as the optical pathlength traveled (and weighted by the wave number k_0). To solve the integral in Eq. 282, we need to determine the function $n(z)$. This task is not trivial since the refractive index depends on the density of the medium which depends on the temperature, pressure, and humidity. Several models and measurements of the dependence of the refractive index on those parameters have been reported, see for example, Refs. [**69, 70, 71**]. For our analysis, we will use the following Sellmeier formula reported in Ref. [**72**]

$$n^2 = 1 + \frac{\mathcal{P}}{\mathcal{T}}\alpha(k), \tag{278}$$

where $\mathcal{P}$ is the atmospheric pressure, $\mathcal{T}$ is the air temperature, and $\alpha(k)$ is a parameter whose value depends on the wavelength [**72**]. Thus, the dependence of the refractive index on the altitude can approximately be written as

$$n(z, k_0) \approx 1 + \frac{1}{2}\frac{\mathcal{P}(z)}{\mathcal{T}(z)}\alpha(k_0), \tag{279}$$

and by using Eq. 276, we get

$$k = k_0 \left[1 + \frac{1}{2}\frac{\mathcal{P}(z)}{\mathcal{T}(z)}\alpha(k_0)\right]. \tag{280}$$

Therefore, there is a correction to the wavelength due to the change in altitude that can be combined with Eq. 216 to yield

$$k \approx k_0 \left[1 + \frac{\Delta V(z)}{c^2} + \frac{1}{2}\frac{\mathcal{P}(z)}{\mathcal{T}(z)}\alpha(k_0)\right]. \tag{281}$$

This last equation shows that the light beam is redshifted not only by the GR but also by the change in refractive index as the beam travels through the atmosphere. Therefore, the phase shift due solely to the refractive index can be written as

$$\Delta\Phi_n = k_0\alpha(k_0)\left[\left(\int_0^{z_{max}} \frac{\mathcal{P}(z)}{\mathcal{T}(z)} dz\right) + \frac{\mathcal{P}(z_{max})}{\mathcal{T}(z_{max})} 2(d - z_{max})\right] - \Phi_{n,1}. \tag{282}$$

We assumed a constant refractive index for the light beam at ground level so $\Phi_{n,1} = k_0 d_g \alpha(k_0)[\mathcal{P}(0)/\mathcal{T}(0)]$. In contrast, for light traveling upwards, we modeled a variable refractive index in the altitude interval $(0, z_{max})$, reflecting changes in atmospheric density. Beyond z_{max}, up to the maximum height d, we again assumed a constant refractive index. Now, to determine the order of magnitude of the contribution due to the change in the refractive index, we need to have an equation describing the dependence of the pressure ($\mathcal{P}$) and temperature ($\mathcal{T}$) on the altitude. An equation giving that dependence on a gravitational field is known as a Barometric formula [**73**]. This equation can be obtained by modeling the atmospheric pressure as the hydrostatic pressure of a fluid and using a thermodynamic equation

of state to introduce the temperature dependence. As an example, let us consider the differential hydrostatic pressure for a fluid of uniform density ρ in a region of constant gravitational field [**74**]

$$d\mathcal{P} = -\rho\, g\, dz, \tag{283}$$

and let us use the equation of state of an ideal gas

$$\mathcal{P} = N k_B \mathcal{T}/V, \tag{284}$$

where N is the number of molecules, k_B is the Boltzmann constant, $\mathcal{T}$ is the temperature, and V is the volume. By combining these equations, we get

$$\frac{d\mathcal{P}}{\mathcal{P}} = -\frac{\bar{m}\, g}{k_B \mathcal{T}} dz, \tag{285}$$

where $\bar{m}$ is the average mass of a fluid molecule per unit of volume. To integrate this equation, we need to establish the temperature dependence with altitude. Let us consider the simplest case where $\mathcal{T}$ is a constant. In that case, the barometric equation is

$$\mathcal{P}(z) = \mathcal{P}_0 \exp\left(-\frac{\bar{m}\, g\, z}{k_B \mathcal{T}}\right), \tag{286}$$

where $\mathcal{P}_0$ is the pressure at sea level. This result was obtained with little effort and shows that the atmospheric pressure decreases exponentially. Notice that we can easily improve our model by introducing corrections to the hydrostatic pressure equation and the equation of state (see for example Ref. [**73**]). For our purposes, it will suffice to introduce a correction by considering that the temperature is not constant but decreases linearly with the altitude, i.e.,

$$\mathcal{T}(z) = \mathcal{T}_0 - \beta z, \tag{287}$$

where $\mathcal{T}_0$ is the temperature at sea level, and β is a parameter that can be adjusted experimentally or obtained theoretically by using conservation-energy arguments. In our analysis, we will use the experimental value of $\beta = 0.00649\,\mathrm{K\,m^{-1}}$ [**73**]. Using this correction for the temperature, the barometric equation is given by

$$\mathcal{P}(z) = \mathcal{P}_0 \left(1 - \frac{\beta z}{\mathcal{T}_0}\right)^{\bar{m} g/k_B \beta}. \tag{288}$$

Notice that this equation defines a maximum altitude given by $z_{max} = \mathcal{T}_0/\beta$. By substituting Eqs. 287 and 288 into Eq. 279, and then into Eq. 282, we get after considering the contribution of the beam going upwards and then going downwards, we get

$$\Delta\Phi_n = k_0\, \mathcal{P}_0\, \alpha(k_0) \left(\int_0^{z_{max}} \left(1 - \frac{\beta\, z}{\mathcal{T}_0}\right)^{\bar{m}\, g/k_B \beta} \left(\mathcal{T}_0 - \beta\, z\right)^{-1} dz + \frac{\mathcal{P}(z_{max})}{\mathcal{T}(z_{max})} (d - z_{max}) \right) - \Phi_{n,1}, \tag{289}$$

Now, by considering that $\lambda_0 = 650\,\mathrm{nm}$, $\mathcal{P}_0 = 1\,\mathrm{atm}$, and $\mathcal{T}_0 = 288.15\,\mathrm{K}$; we can evaluate $\alpha(k_0) = 1.5693 \times 10^{-6}\,\mathrm{K\,Pa^{-1}}$ [**72**], and $z_{max} = 21103\,\mathrm{m}$. Besides, by considering that $g = 9.8\,\mathrm{m\,s^{-2}}$, $k_B = 1.38 \times 10^{-23}\mathrm{J\,K^{-1}}$, and that for dry air $\bar{m} = 4.8 \times 10^{-26}\,\mathrm{kg}$ [**75**]; we can evaluate the above integral to obtain

$$\Delta\Phi_n \sim 10^7\,\mathrm{rad} - \Phi_{n,1}. \tag{290}$$

As is the case with lunar laser ranging, we can expect that the atmosphere will be the principal source of error when operating the light gravimeter. The fluctuations in the value of the phase shifts can spoil the measurement, and in the case of the refractive index, we expect large fluctuations since its contribution to the phase is larger than the effect caused by the GR. Since the atmospheric pressure does not change appreciably during the day, we expect that the fluctuations in temperature will be the source of principal error. To confirm this, we can estimate the fluctuation in the value calculated in Eq. 290 caused by a variation in the temperature model given by Eq. 287. The variational derivative of Eq. 289 with respect to $T_0(z)$ (Eq. 287) is given by

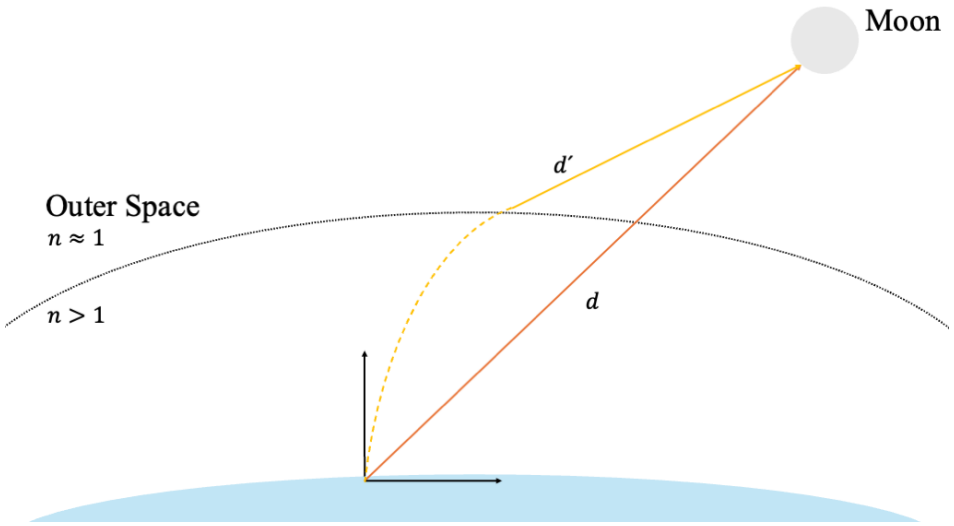

Figure 9: The continuous change in the refractive index of the atmosphere causes the bending of the light as it passes through it. As a result, the objects in the sky appear to be higher than their true position ($d' > d$). Notice that this effect is zero if the light travels in the direction of the zenith. The effect has been exaggerated for purposes of illustration.

$$\frac{\delta\left(\Delta\Phi_n + \Phi_{n,1}\right)}{\mathcal{T}(z)} = -k_0\,\mathcal{P}_0\,\alpha(k_0)\int_0^{z_{max}}\left(1-\frac{\beta\,z}{\mathcal{T}_0}\right)^{\bar{m}\,g/k_B\beta}\left[\mathcal{T}(z)\right]^{-2}dz. \tag{291}$$

We can evaluate this result for $\lambda_0 = 650\,\text{nm}$ and the same parameter values used before to get

$$\frac{\delta\left(\Delta\Phi_n + \Phi_{n,1}\right)}{\mathcal{T}(z)}\Big|_{\mathcal{T}(z)=\mathcal{T}_0-\beta z} \sim 10^5\,\text{rad}\cdot\text{K}^{-1} \tag{292}$$

This result indicates that the fluctuations due to the temperature are considerably high and clever approaches are needed to overcome them and be able to operate the light gravimeter. Notice that the phase shift $\Delta\Phi_n$ and its fluctuations are linearly proportional to k_0.

One possible solution to reduce the atmospheric error is to perform a differential measurement such as that analyzed in Ref. **[50]**. This technique involves two consecutive measurements via a fast switching between two retroreflectors (on the Moon or on two different Earth-orbiting satellites) and, because of the similarity of the optical path between the two measurements, the phase difference of these successive measurements can be used to isolate the Earth's atmospheric error. Similarly, another possible solution could be to use two beams with different frequencies and therefore with varying responses to the change in the refractive index of the atmosphere.

2.7.2 Atmospheric refraction

Besides the phase shift of Eq. 289. The change in the refractive index also bends the light while it passes through the atmosphere. This continuous bending of the light is known as atmospheric refraction **[76]**. As a result, the objects in the sky appear higher than their true position as shown in Fig. 9. This effect is null at the zenith and it increases towards the horizon. Thus, if the retroreflector in Fig. 4 is not at the zenith, it is imperative to consider corrections to the optical pathlength of the upper arm of the interferometer. The problem becomes more complicated because the refraction (and consequently the bending) depends on the wavelength. Fortunately, the model introduced in Section 2.6.3 considers that the upper arm of the interferometer points to the zenith. Thus, in our analysis, we can safely ignore this correction.

2.7.3 Rayleigh Scattering

Another effect of an electromagnetic wave passing through the atmosphere is the scattering of some of the wave's energy. The incoherent scattering caused by the air molecules produces an attenuation of

the light beam that can be described by the Rayleigh scattering [**77**]

$$\alpha' = \frac{2k^4}{3\pi N'}|n-1|^2, \tag{293}$$

where N' is the number of molecules per unit volume and α' is the attenuation coefficient. Thus, the intensity of the beam can be described by

$$I(z) = I_0 e^{-\alpha' z}. \tag{294}$$

Notice that the attenuation coefficient is proportional to k^4. Thus, in the visible spectrum, red light is scattered less than violet light. In fact, by using the isothermal model of Eq. 286, it is possible to show that the density varies exponentially with height, and by using this, we can estimate the intensity at the Earth's surface relative to the incident intensity on top of the atmosphere at different wavelengths at zenith [**77**]. The result is shown in Table 4. Notice that as expected, the intensity at shorter wavelengths is attenuated more than for larger wavelengths. This result is important since according to Eq. 263, the GR produces a larger phase shift for smaller wavelengths. Thus, there is a trade-off between a larger phase shift and a smaller attenuation of the light beam. Notice that the results in Table 4 only consider the attenuation of the incoming beam, but the same effect occurs with the outgoing beam. Thus, for a violet light beam, Rayleigh scattering would cause an attenuation of almost half the initial intensity for the upper arm in Fig. 4. What is more, the attenuation is greater than that of Eq. 294 because of the presence of water vapor that causes strong absorption bands in the infrared and ozone which causes absorption of the ultraviolet [**77**].

Table 4: Intensity at the Earth's surface relative to the incident intensity on top of the atmosphere for different wavelengths at zenith [**77**]. This result is obtained by considering the isothermal model of the atmosphere (Eq. 286), and the Rayleigh scattering Eq. 294.

Color	$I(z_{max})/I_0$
Red (650 nm)	0.96
Green (520 nm)	0.90
Violet (410 nm)	0.76

2.8 Light beam considerations

In this section, we analyze some of the properties that the light source, used to operate the light gravimeter, needs to have and some additional systematics introduced by considering more realistic light beams.

2.8.1 Rayleigh distance

The successful implementation of the interferometer shown in Fig. 4, requires a cautious selection of the initial light beam waist and its bandwidth to maximize the contrast of the fringes. In section 2.7.3, we saw that the Rayleigh scattering causes an attenuation of the beam intensity. Besides Rayleigh scattering, a rapid divergence of the laser beam can cause the beam width to diverge such that for a long distance as that considered for the experimental setup of Fig. 4, only a fraction of the beam will be retroreflected, causing a loss of intensity. By considering a laser beam with a Gaussian profile, and setting the initial beam waist at $z = 0$, the beam waist can be described by [**47**]

$$w(z) = w_0\sqrt{1+\left(\frac{z}{z_R}\right)^2}, \tag{295}$$

where z_R is the Rayleigh length defined as

$$z_R = \frac{\pi w_0^2}{\lambda_0}. \tag{296}$$

This length defines the distance at which the cross-sectional area doubles or the distance at which $w(z) = \sqrt{2}w_0$. We can use the above equation to find out the initial beam width needed to have a

Rayleigh length of the same order of magnitude as the average distance from the Earth to the Moon, i.e., $z_R \sim 10^8$m. Thus, by using $\lambda_0 = 650\,\text{nm}$, we have that $w_0 \sim 4\,\text{m}$. For reference, notice that the Appollo 11 and 14 retroreflectors have an array size of 46 cm $\times$46 cm [**51**]. This means that the cross-section of the Gaussian beam (defined as the area of a circle of radius w) is around one order of magnitude larger than the retroreflector area. Therefore, an ideal implementation of the light gravimeter would require the placing of a retroreflector with a larger array size to avoid a considerable loss of intensity of the returning beam.

2.8.2 Coherence length

The interference fringes discussed in Section 2.4 only are formed when the light bandwidth $\Delta\nu$ and the path difference of the two arms of the interferometer Δl satisfy the following relation [**78, 47**]

$$\Delta l_c \Delta\nu \lesssim c. \tag{297}$$

From this relation, the coherence length of the light source is defined as

$$\Delta l_c = \frac{c}{\Delta\nu}. \tag{298}$$

Notice that the long distances required to operate the light gravimeter are not a problem because the coherence length depends on the path difference and not on the absolute path length of the individual arms. However, given the enormous length of the vertical arm, it sounds more realistic to use an unbalanced arms configuration with a shorter arm on the ground. In that case, the experimental design must consider that the path difference has to be much shorter than the coherence length so the contrast of the fringes is not affected. To illustrate this point, consider a laser with a bandwidth of 10 kHz, the coherence length for that laser would be around $\Delta l_c \sim 30$ km.

2.8.3 Mode Matching

Let us consider a laser beam with a Gaussian profile to quantify the effect of mode mismatching on the interference fringes. The electric field of this laser beam when it arrives at the detector is given by[30]

$$\vec{E_i}(r,t) = E_0\hat{x}\frac{w_0}{w(z)}\exp\left[\frac{-r^2}{w^2(z)}\right]\cos\left[-k_0 z - k_0\frac{r^2}{2R(z)} + \psi(z) + wt\right], \tag{299}$$

where r is the distance measured in a plane transverse to the propagation axis, $R(z) = z\big[1 + (z_R/z)^2\big]$ is the radius of curvature, $\psi(z) = \arctan(z/z_R)$ is the Gouy phase and $i = 1, 2$ is the path traveled by the beam in the interferometer. The irradiance obtained by the interference of a Gaussian beam with electric field $\vec{E_1}$ that traveled a distance d_g and another beam with electric field $\vec{E_2}$ that traveled a distance $2d$ is given by

$$I \propto \langle|\vec{E}|^2\rangle_T = \lim_{T\to\infty}\frac{1}{T}\int_t^{t+T}|\vec{E}|^2 dt', \tag{300}$$

where $\vec{E} = \vec{E_1} + \vec{E_2}$ and $|\vec{E}|^2 = |\vec{E_1}|^2 + |\vec{E_2}|^2 + 2\vec{E_1}\cdot\vec{E_2}$ so $I = I_1 + I_2 + I_{12}$ with $I_1 \propto \langle|\vec{E_1}|^2\rangle_T$, $I_2 \propto \langle|\vec{E_2}|^2\rangle_T$, and $I_{12} \propto 2\langle\vec{E_1}\cdot\vec{E_2}\rangle_T$. Thus,

$$I_1 \propto \left[\frac{E_0\, w_0}{w(d_g)}\right]^2 e^{-2r^2/w^2(d_g)}, \tag{301}$$

$$I_2 \propto \left[\frac{E_0\, w_0}{w(2d)}\right]^2 e^{-2r^2/w^2(2d)}, \tag{302}$$

and

$$I_{12} \propto -\left[\frac{E_0^2 w_0^2}{w(2d)\, w(d_g)}\right]\exp\left\{-r^2\left[\frac{1}{w^2(2d)} + \frac{1}{w^2(d_g)}\right]\right\} \cos\left\{k_0 2d - k_0 d_g + \frac{k_0 r^2}{2}\left[\frac{1}{R(2d)} - \frac{1}{R(d_g)}\right] - \psi(2d) + \psi(d_g)\right\}, \tag{303}$$

[30] For this calculation, we are supposing that the whole vertical beam is retro-reflected without suffering any apodization.

The effect of mode matching can be seen by averaging the irradiance over a circular detector of radius ρ to get the total power as follows

$$P \propto \int_0^{\rho} \int_0^{2\pi} I\, r\, dr\, d\theta. \tag{304}$$

The integration of the I_1 and I_2 terms is straightforward. The result is given by

$$P_1 \propto \left(\frac{E_0 w_0}{2}\right)^2 \left[1 - e^{-2\rho^2/w^2(d_g)}\right], \tag{305}$$

and

$$P_2 \propto \left(\frac{E_0 w_0}{2}\right)^2 \left[1 - e^{-2\rho^2/w^2(2d)}\right]. \tag{306}$$

Integrating the interference term I_{12} is more complicated. Fortunately, for our analysis, we can get a qualitative result by considering that $d_g \sim 0$ for which $1/R(d_g) \sim 0$ and $2d \gg z_R$ for which $1/R(2d) \sim 0$, i.e., in the limit of large or short z the curvature term $k_0 r^2/2R(z)$ of Eq. 299 is approximately zero and the oscillatory term of the beam becomes that of a plane wave (except for the Gouy phase contribution). Therefore, in this approximation, the oscillatory term does not contribute significantly to the integral and it can be considered constant, so the integration yields

$$P_{12} \propto \frac{E_0^2 w_0^2\, w(2d)\, w(d_g)}{2\left[w^2(2d) + w^2(d_g)\right]} \left(1 - \exp\left\{ - \left[\frac{1}{w^2(2d)} + \frac{1}{w^2(d_g)}\right]\rho^2 \right\}\right) \cos\left\{k_0 2d - k_0 d_g + \frac{k_0 \rho^2}{2}\left[\frac{1}{R(2d)} - \frac{1}{R(d_g)}\right] - \psi(2d) + \psi(d_g)\right\}. \tag{307}$$

Finally, $P = P_1 + P_2 + P_{12}$ is given by

$$P \propto \left(\frac{E_0 w_0}{2}\right)^2 \left(2 - e^{-2\rho^2/w^2(d_g)} - e^{-2\rho^2/w^2(2d)} + \frac{2w(2d)\, w(d_g)}{\left[w^2(2d) + w^2(d_g)\right]} \left(1 - \exp\left\{ - \left[\frac{1}{w^2(2d)} + \frac{1}{w^2(d_g)}\right]\rho^2 \right\}\right) \cos\left\{k_0 2d - k_0 d_g + \frac{k_0 \rho^2}{2}\left[\frac{1}{R(2d)} - \frac{1}{R(d_g)}\right] - \psi(2d) + \psi(d_g)\right\}\right). \tag{308}$$

This result indicates that the main effect of mode mismatching is a reduction in the contrast or visibility of the fringes. To see this, let's compute the interferometric visibility defined as $\mathcal{V} = (P_{max} - P_{min})/(P_{max} + P_{min})$ where P is maximized(minimized) with respect to the argument of the cosine in P_{12}. The result is

$$\mathcal{V} \propto \frac{4\, w(2d)\, w(d_g) \left(1 - \exp\left\{ - \left[\frac{1}{w^2(2d)} + \frac{1}{w^2(d_g)}\right]\rho^2 \right\}\right)}{\left[w^2(2d) + w^2(d_g)\right]\left[2 - e^{-2\rho^2/w^2(d_g)} - e^{-2\rho^2/w^2(2d)}\right]} \tag{309}$$

By considering that $\rho \to \infty$, the above expressions simplify to

$$P_1, P_2 \propto \left[\frac{E_0 w_0}{2}\right]^2, \tag{310}$$

$$P_{12} \propto \frac{E_0^2 w_0^2\, w(2d)\, w(d_g)}{2\left[w^2(2d) + w^2(d_g)\right]} \cos\left\{k_0 2d - k_0 d_g - \psi(2d) + \psi(d_g)\right\}, \tag{311}$$

and

$$P \propto \left(\frac{E_0 w_0}{2}\right)^2 \left(2 + \frac{2w(2d)\, w(d_g)}{\left[w^2(2d) + w^2(d_g)\right]} \cos\left\{k_0 2d - k_0 d_g - \psi(2d) + \psi(d_g)\right\}\right). \tag{312}$$

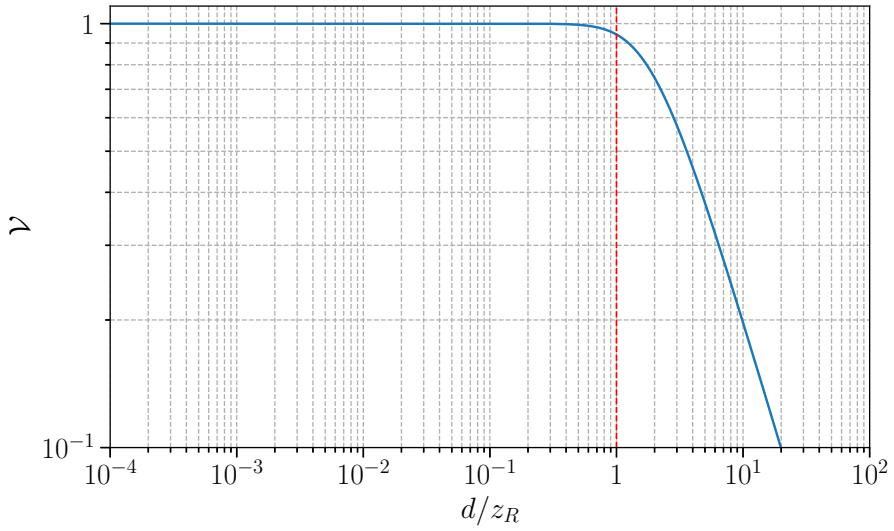

Figure 10: Visibility of the interference of two Gaussian Beams according to Eq 313. For this plot, we supposed that $w_0 = 1\text{m}$, $d_g = 1\text{m}$, and $\lambda_0 = 650\,\text{nm}$ so that the Rayleigh distance is $z_R = 4.8 \times 10^6\text{m}$. Refer to the text for additional details on the calculation.

with the visibility given by

$$\mathcal{V} \propto \left\{ \frac{2\, w(2d)\, w(d_g)}{\left[w^2(2d) + w^2(d_g)\right]} \right\}. \tag{313}$$

Figure 10 shows how according to Eq. 313, the visibility begins to drop drastically when $d \sim z_R$ as expected. This effect is much less relevant in atomic gravimetry due to the short distances over which the atoms travel.

Besides the loss of visibility, Eq. 308 also indicates the existence of two new systematic effects when considering Gaussian laser beams due to the Radius of curvature and the Gouy phase terms. The phase shift caused by the Gouy phase can be defined according to Eq. 308 as

$$\Delta\Phi_\psi = -\psi(2d) + \psi(d_g) = -\arctan\left(2d/z_R\right) + \arctan\left(d_g/z_R\right), \tag{314}$$

and the phase shift due to the radius of curvature as

$$\Delta\Phi_R = \frac{k_0\rho^2}{2}\left[\frac{1}{R(2d)} - \frac{1}{R(d_g)}\right] = \frac{k_0\rho^2}{2}\left[\frac{1}{2d\left[1 + (z_R/2d)^2\right]} - \frac{1}{d_g\left[1 + (z_R/d_g)^2\right]}\right] \tag{315}$$

Let's analyze these phase shifts in the limit $d_g \sim 0$ and $d \gg z_R$. For this limit, the expansions $\arctan = (x - x^3/3 + x^5/5 + \ldots)$ valid at $x = 0$ and the expansion $\arctan = (\pi/2 - 1/x + 1/3x^2 + \ldots)$ valid at $x = \infty$ can be used to approximate the phase shift due to the Gouy phase. By using the dominant term in each expansion, the sensitivity due to this phase shift can be written as

$$\left(\frac{\Delta\Phi_\psi}{\Delta\Phi_g}\right)_{light} = \left(\frac{\pi}{2} - \frac{d_g\lambda_0}{\pi w_0^2}\right)\frac{\lambda_0}{2\pi g}\left(\frac{c}{2d}\right)^2, \tag{316}$$

where we used Eq. 234 and $T = d/c$. Similarly, for the phase shift due to the Radius curvature

$$\left(\frac{\Delta\Phi_R}{\Delta\Phi_g}\right)_{light} = \frac{\rho^2}{2g}\left(\frac{1}{2d} - \frac{d_g}{z_R^2}\right)\left(\frac{c}{2d}\right)^2. \tag{317}$$

It is instructive to look for the equivalent phase shifts in the case of atomic gravimetry. This correspondence can be elucidated by considering the limit when $d_g \sim 0$ and $d \sim 0$. Following the same procedure as before, the sensitivity due to the phase shift of the Gouy phase becomes

$$\left(\frac{\Delta\Phi_\psi}{\Delta\Phi_g}\right)_{light} = -\frac{\Delta z\,\lambda_0^2}{2g\,\pi^2 w_0^2\,T^2}, \tag{318}$$

where $\Delta z = d_g - 2d$. By substituting $\Delta z = \frac{1}{2}gT^2$ which is the vertical displacement of an atom in an atomic gravimetry, the sensitivity becomes

$$\left(\frac{\Delta\Phi_\psi}{\Delta\Phi_g}\right)_{light} = -\frac{\lambda_0^2}{4\,\pi^2 w_0^2}. \tag{319}$$

This result maps perfectly with the corresponding result in atomic gravimetry discussed in Ref. [**79**]. Similarly, in the case of the phase shift due to the Radius curvature, the result is

$$\left(\frac{\Delta\Phi_R}{\Delta\Phi_g}\right)_{light} = -\frac{\Delta z\,\rho^2\lambda_0^2}{2\,g\,T^2\,\pi^2 w_0^4}. \tag{320}$$

By considering that the value of ρ/T is approximately equal to the value of the standard deviation of the atomic velocity distribution in the atomic gravimetry σ_v, the sensitivity becomes

$$\left(\frac{\Delta\Phi_R}{\Delta\Phi_g}\right)_{light} = -\frac{\Delta z\,\lambda_0^2\sigma_v^2}{2\,g\,\pi^2 w_0^4}. \tag{321}$$

Once again, this result matches the corresponding result in atomic gravimetry [**79**]. Notice that even though Eqs. 316 and 317 represent the correct result for the distances required to operate the light gravimeter, the correspondence with atomic gravimetry is seen only when the arm length and the time interval are on the order of magnitude of the corresponding values in atomic gravimetry.

2.8.4 Beam misalignment

A misalignment of the light beam in the vertical arm of Fig. 4 introduces a phase shift. This shift can be calculated by considering the additional optical path traversed by the misaligned beam. Figure 11 illustrates the path of a beam entering a corner cube at an angle θ relative to the z-axis and its subsequent retroreflection. While the derivation is tedious, it can be easily shown that the beam exits the corner cube at the same angle θ. To analyze the interference at the detector (located at P_0), we must consider the interaction between the retroreflected plane wave at p_f and the beam from the other arm (at p_0). For small angles, the optical path (highlighted in red in the figure) is given by

$$d' \approx 2d - d\theta^2, \tag{322}$$

while the displacement (Δx) in the x-axis is given (for small angles) by

$$\Delta x \approx 2d\theta. \tag{323}$$

By taking $d_g = 2d$ in Eq. 261 and considering the correction to the optical path due to the beam misalignment, we get

$$\Delta\Phi'_{light} = \Delta\Phi_g + \sigma_{\Delta\Phi_d}, \tag{324}$$

where

$$\sigma_{\Delta\Phi_d} \approx -k_0 d\theta^2. \tag{325}$$

Then, for distances close to the Earth, we can use Eq. 234, and the sensitivity will be given by

$$\left(\frac{\sigma_g}{g}\right)_{light} \approx -\frac{c^2}{gd}\theta^2, \tag{326}$$

where we considered $T = d/c$. Or more in general,

$$\left(\frac{\sigma_g}{g}\right)_{light} \approx -\frac{c^2}{\Delta V}\theta^2. \tag{327}$$

Eq. 326 indicates that achieving a sensitivity on the order of 10^{-9} requires an extraordinarily precise angle of 10^{-9} rad for a distance $d = 10^8$ m. Notably, the sensitivity improves as the distance d increases.

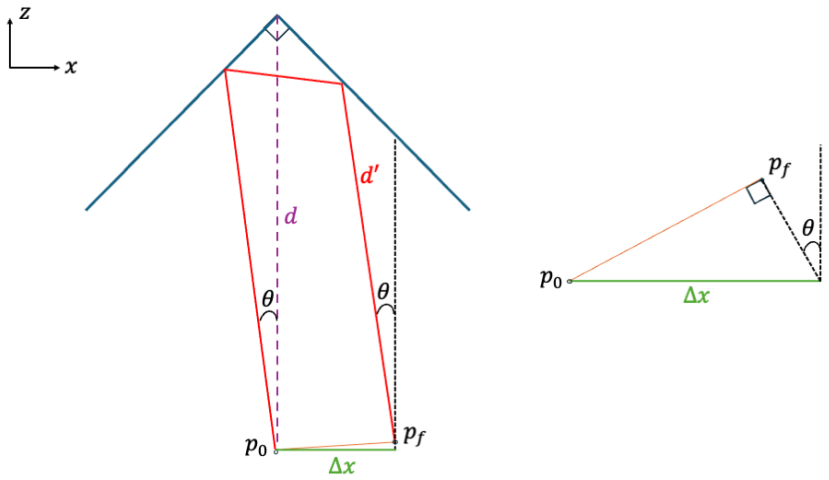

Figure 11: Path of a light beam through a corner cube reflector with misalignment. The beam enters the corner cube at an angle θ relative to the z-axis and is retroreflected. The figure shows the incident beam, its path through the corner cube, and the exiting beam, which leaves at the same angle θ. The optical path is highlighted in red, demonstrating the additional distance traversed due to misalignment. Points p_0 (detector location) and p_f are marked to show the interference analysis. The figure also indicates the displacement Δx in the x-axis and the vertical distance d, helping visualize the geometrical relationships described in the optical path length and displacement equations.

While this may seem counterintuitive, it arises from the phase scaling quadratically with distance (close to the Earth), while the uncertainty due to misalignment grows only linearly. To be consistent with our notation of systematic contributions, we will define $\Delta\Phi_{ma} \equiv \sigma_{\Delta\Phi_d}$. For reference, for $\lambda_0 = 650\,\text{nm}$, and $\theta = 10^{-4}\,\text{rad}$, the contribution is about $\Delta\Phi_{ma} \sim -10^7\,\text{rad}$.

Examining the systematic error caused by misalignment in light gravimeters is an instructive exercise, since it allows a straightforward comparison with the corresponding systematic error in atomic gravimeters. When considering a vertical misalignment of the Raman wave vector by an angle θ in an atomic gravimeter, the phase of a typical atomic gravimeter is modified as follows [**17**]

$$\Delta\Phi'_{matter} = \Delta\Phi_{matter} + (\sigma_{\Delta\Phi_g})_{matter}, \tag{328}$$

where

$$(\sigma_{\Delta\Phi_g})_{matter} = k_{eff} g T^2 (\cos\theta - 1), \tag{329}$$

and for small angles

$$(\sigma_{\Delta\Phi_g})_{matter} \approx -k_{eff} g T^2 \frac{\theta^2}{2}. \tag{330}$$

Thus, the sensitivity due to vertical misalignment in atomic gravimetry is given by

$$\left(\frac{\sigma_g}{g}\right)_{matter} \approx -\frac{\theta^2}{2}. \tag{331}$$

We can observe that the sensitivity to beam misalignment in matter gravimetry exhibits a quadratic dependence on the deviation angle, similar to light gravimetry (as shown in Eq. 326). However, in the case of light gravimetry, the sensitivity is further modulated by the inverse of the wave vector change due to gravitational redshift, as expressed in Eq. 216. This causes the deviation angle requirement to be less restrictive for matter gravimetry (a precision of 1μGal requires an angle less than 45μrad [**17**]). A more thorough analysis of the effect of beam misalignment in atomic gravimetry can be found in [**79**]. The presence of the factor $c^2/\Delta V$ in Eq. 327, absent in Eq. 331, stems from fundamental differences in the phase shift calculations. In the light interferometer, Eq. 325 represents a correction to the phase

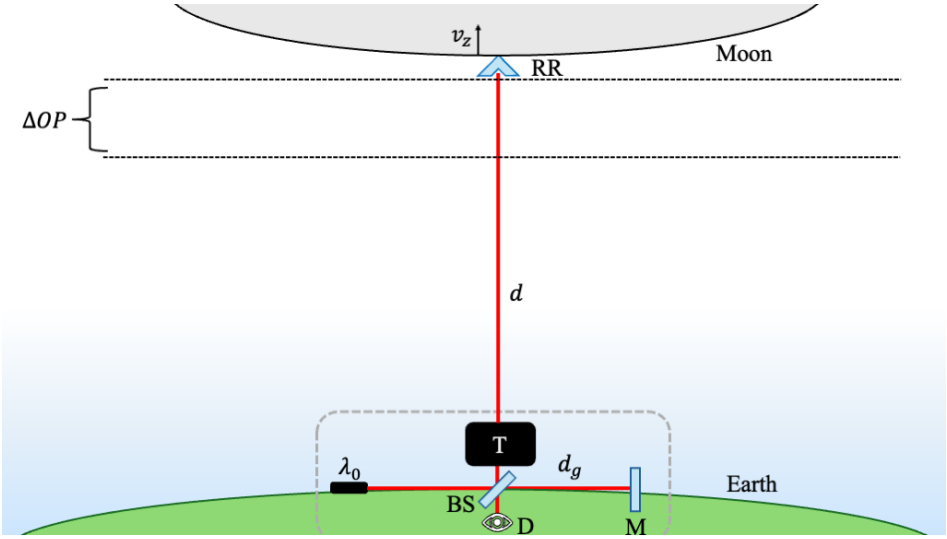

Figure 12: The Doppler effect causes successive crests of waves to take different amounts of time to arrive at the detector which can be interpreted as a change in the optical path followed by the light beam. Figure not at scale.

term ($\Delta\Phi_d$) determined solely by differences in optical path lengths (Eq. 261), which are independent of g. Conversely, in the matter interferometer, the correction applies to the gravity-dependent phase term which is independent of path length.

2.8.5 Doppler Shift

Since the retroreflector used to return the light beam to the Earth is orbiting either in a satellite or the Moon, there is a Doppler shift caused by the fact that successive pulses or successive crests of waves take different amounts of time to arrive at the observer [**42**]. Let us consider a reference frame where the Earth is static and the retroreflector is in motion (see Fig 12). The change in frequency due to the Doppler effect is given by [**77**]

$$\Delta w = \vec{k_0} \cdot \vec{v}, \tag{332}$$

where $\vec{v}$ is the velocity of the retroreflector. The sign of the change in frequency depends on whether the retroreflector is approaching or moving away from the Earth. The light beam is sent through the zenith which is aligned with the z-axis of the reference frame, thus, only the z-component of the velocity is relevant in our calculation, i.e.,

$$\Delta w = k_0 v_z. \tag{333}$$

Due to the motion of the retroreflector, the light beam travels an additional distance (optical path) given by

$$\Delta OP \propto v_z \tau, \tag{334}$$

where τ is the time we spend taking data measurements. This distance causes a phase shift given by Eq. 229, i.e.,

$$\Delta\Phi_D = k_0 \Delta OP \propto k_0 v_z \tau. \tag{335}$$

For example, by considering $\lambda_0 = 650\,\text{nm}$, $\tau = 1\,\text{s}$ and, $|v_z| \sim 1\,\text{Km}\,\text{s}^{-1}$, we get $|\Delta\Phi_D| \sim 10^6\,\text{rad}$. This phase shift is of consideration due to the large Doppler effect caused by the large number of cycles that the wave performs during the measurement time. Notice that in this rough estimation, we considered $|v_z|$ to have a constant value[31] approximately equal to the average orbital speed of the Moon.

[31]We can consider $|v_z|$ to have a constant value for short values of τ since the Moon's orbital period is 27 days, so dv_z/dt is negligible for the measurement time considered.

If we perform a measurement and then move the gravimeter to a new position, we'll need to determine the change in $\Delta\Phi(\tau)$ for the time it took to move the gravimeter and begin a new measurement. This is only possible if v_z can be determined with high enough precision. Fortunately, since the distance to the Moon can be determined with a precision of less than 1 cm [**50, 51**], the value of v_z can be determined with high precision as well. A quick estimation can be done by considering that the orbit of the Moon around the Earth is circular, in that case, the relationship between the orbital speed of the Moon and the radius of the orbit can be easily computed, and the precision of 1 cm in the radius of the orbit gives a fractional precision on the orbital speed of about 10^{-10}.

Table 5 summarizes the different contributions, analyzed so far, to the phase measured with the experiment proposed in Fig. 4 and the order of magnitude of each contribution

$$\Delta\Phi(\tau) = \Delta\Phi_d + \Delta\Phi_g + \Delta\Phi_{ms} + \Delta\Phi_{ma} + \Delta\Phi_n + \Delta\Phi_D(\tau) + \Delta\Phi_\psi + \Delta\Phi_R. \tag{336}$$

$\lambda_0 = 650\,\text{nm}$, $d = 10^8\,\text{m}$, $w_0 = 1\,\text{m}$, $\rho = 1\,\text{cm}$
$\Delta\Phi_d \sim 10^{15}\,\text{rad} - k_0 d_g$
$\Delta\Phi_g \sim -10^6\,\text{rad}$
$\Delta\Phi_{ms} \sim 10^4\,\text{rad}$
$\Delta\Phi_{ma} \sim -10^7\,\text{rad}$
$\lvert\Delta\Phi_D\rvert \sim 10^6\,\text{rad}$
$\Delta\Phi_n \sim 10^7\,\text{rad} - \frac{\alpha(k_0)}{2}\frac{P_0}{\mathcal{T}_0}k_0 d_g$
$\Delta\Phi_\psi \sim -10^0\,\text{rad} + \arctan\left(\frac{d_g}{z_R}\right)$
$\Delta\Phi_R \sim 10^{-36}\,\text{rad} - \frac{\rho^2 k_0/2}{d_g\left[1+(z_R/d_g)^2\right]}$

Table 5: Order of magnitude of the different phase contributions analyzed so far for the experiment proposed in Fig. 4. $\Delta\Phi_d$ is the geometrical phase, $\Delta\Phi_g$ is the gravitational phase due to the Earth, $\Delta\Phi_{ms}$ is the gravitational phase shift due to the Moon and the Sun, $\Delta\Phi_{ma}$ is the phase shift due to the misalignment, $|\Delta\Phi_D|$ is the phase shift due to the Doppler effect, $\Delta\Phi_n$ is the phase shift due to the change in refractive index of the atmosphere, $\Delta\Phi_\psi$ is the phase shift due to the Gouy phase, and $\Delta\Phi_R$ is the phase shift due to the radius of curvature. Refer to the text for additional details about how these estimations were obtained.

2.9 Comparisson of Light and Matter gravimeters

The universality of free fall—the observation that all bodies accelerate identically under gravity regardless of their composition—was established empirically by Galileo and later incorporated in 1752 into Newton's law of universal gravitation. Today, this principle of dropping a test mass and measuring its trajectory through space-time remains fundamental in determining the absolute value of the gravitational acceleration [**80**]. This method has proved to be highly effective, for instance, highly precise gravity measurements can be achieved using lasers to measure the free fall of cooled atomic ensembles in a vacuum [**17**]. In this section, we focus on the study of the differences between light and matter gravimeters. The fundamental question we aim to address is whether there is a physical reason that makes one type of gravimeter more suitable for measuring gravity, or if both types are physically equivalent, with the only differences being the distinct experimental challenges involved in their implementation.

We begin by comparing the energy change involved in the process of dropping a mass with the energy change involved in the gravitational redshift of a photon. If the energy required for a photon to climb a distance d were different from the energy a mass loses when dropped from the same distance, it would indicate that one type of gravimeter involves a greater energy change than the other, providing a clear advantage. However, this is not the case. It turns out that the process of dropping a mass and the redshift of a photon are energetically equivalent. This idea was proposed by Einstein in 1911 [**81**] using the following thought experiment [**68**]: Consider a particle of rest mass m that is dropped from the top of a tower, as illustrated in Fig. 13. The particle falls freely with an acceleration g and reaches the ground with a final velocity given by $v = \sqrt{2\,g\,d}$. An observer on the ground measures the total energy of this mass as

$$E = mc^2 + \frac{1}{2}mv^2 + \mathcal{O}(v^4) = mc^2 + mgd + \mathcal{O}(v^4). \tag{337}$$

Suppose that we can convert all this energy into a photon of the same energy and direct it upwards. When this photon reaches the top of the tower, it has a rest energy E'. Suppose that we convert all this energy into a particle of mass $m' = E'/c^2$. Then, we must have that $m' \leq m$, otherwise, we could obtain perpetual motion. Therefore, a photon climbing in the Earth's gravitational field is redshifted and loses the energy[32] given by

$$\Delta E = mgd. \tag{338}$$

This result was demonstrated experimentally by measuring the redshift [**66, 67, 68**] which can be obtained from Eq. 337, i.e.,

$$\frac{E}{E'} = \frac{mc^2}{mc^2 + mgd + \mathcal{O}(v^4)} = 1 - \frac{gd}{c^2} + \mathcal{O}(v^4) \tag{339}$$

from which one arrives at Eq. 216 by using the Planck relation and[33] $\Delta V = gd$.

Recapitulating, in the case of dropping a mass, the potential energy given by Eq. 338 is converted into kinetic energy. We could say that the potential energy is lost because it was converted into another form of energy, in this case, kinetic energy. Something similar happens in the case of the GR, in this case, an amount of energy equal to the potential energy given by Eq. 338 is taken from the total energy of the photon and converted into another type of energy, whatever type of energy it is, we can say that this energy is lost[34]. Therefore, we can conclude that the processes of dropping a mass and a photon's redshift are energetically equivalent, i.e., the change in potential energy (in the case of the mass dropping) and the change in total energy (in the case of the GR) are the same, in both cases, the change in energy is given by Eq. 338.

From an energy point of view, even though we are used to hear phrases such as *photons do not have mass*, there is no fundamental difference between *lifting* light or dropping a mass as both processes involve the same change in gravitational potential. In the case of the comparison between light and matter gravimeters, there is also no fundamental difference between both approaches because the phase signal of both interferometers is obtained from the action divided by $\hbar$, as we show next. First, let us consider the phase for the light gravimeter in Eq. 228, expressed in terms of momentum using de Broglie's relation

$$\Phi_{light,i} = \frac{1}{\hbar}\int_{\Gamma_i}\left(1 - \frac{\Delta V}{c^2}\right)\vec{p_0}\cdot\vec{dr} + \varphi_i, \tag{340}$$

where φ_i is an arbitrary initial phase offset. The total energy of the photon is given by $E_{light} = p_0 c$, so the dot product can be written as $\vec{p_0}\cdot\vec{dr} = E_{light}\cos(\theta)dr/c$, where θ is the angle between $\vec{p_0}$ and $\vec{dr}$. Now, by taking $\theta = 0$, and using the change of variable $dr \equiv c\,dt$, we get

$$\Phi_{light,i} = \frac{1}{\hbar}\int_{\Gamma_i}\left(1 - \frac{\Delta V}{c^2}\right)E_{light}dt + \varphi_i. \tag{341}$$

By taking the difference of phase in both paths, we arrive at the signal measured by the interferometer

$$\Delta\Phi_{light} = \frac{E_{light}}{\hbar}\left[\left(\int_{\Gamma_2} dt - \int_{\Gamma_1} dt\right) - \frac{1}{c^2}\left(\int_{\Gamma_2}\Delta V dt - \int_{\Gamma_1}\Delta V dt\right)\right] + \left(\varphi_2 - \varphi_1\right), \tag{342}$$

On the other hand, for a typical atomic gravimeter [**17**], the phase acquired on each of the arms is given by the well know expression [**21**]

$$\Phi_{matter,i} = \frac{1}{\hbar}\int_{\Gamma_i} L_{matter}\,dt + \varphi_i, \tag{343}$$

[32] In this sense, the energy that is lost acts as a kind of potential energy.

[33] For purposes of comparison we simply take $d \ll R_e$.

[34] In this thought experiment, this energy is recovered in the form of potential energy when the photon is converted again into a particle of mass m.

where $L_{matter} = -m_0c^2/\gamma - m_0\Delta V$ is the Lagrangian of the atom of rest mass m_0 subject to the gravitational potential and $i = 1, 2$ represents the path. Thus, by substituting L_{matter}, we get

$$\Phi_{matter,i} = \frac{1}{\hbar}\int_{\Gamma_i} -m_0c^2\left(1+\gamma\frac{\Delta V}{c^2}\right)dt/\gamma + \varphi_i. \tag{344}$$

The rest energy term is constant on each path so we can write

$$\Delta\Phi_{matter} = \frac{E_{matter}}{\hbar}\left[-\left(\int_{\Gamma_2} d\tau - \int_{\Gamma_1} d\tau\right) - \frac{1}{c^2}\left(\int_{\Gamma_2}\Delta V dt - \int_{\Gamma_1}\Delta V dt\right)\right] + \left(\varphi_2 - \varphi_1\right), \tag{345}$$

where $E_{matter} = m_0c^2$ is the rest energy of the atom and $d\tau = dt/\gamma$ is the proper time of the atom's center of mass.

Equations 342 and 345 are general, independent of the paths chosen, and can be written into a single equation as

$$\Delta\Phi_{light,matter} = \frac{E_{light,matter}}{\hbar}\left[\pm\left(\int_{\Gamma_2} dt' - \int_{\Gamma_1} dt'\right) - \frac{1}{c^2}\left(\int_{\Gamma_2}\Delta V dt - \int_{\Gamma_1}\Delta V dt\right)\right] + \left(\varphi_2 - \varphi_1\right). \tag{346}$$

In this context, dt' represents dt in the case of the light gravimeter and it becomes $d\tau$ in the case of the matter gravimeter. Equation 346 shows that the interferometric phase calculation is essentially equivalent and takes the same form in both types of gravimeters. Although the light and matter gravimeters initially seem different, they fundamentally operate in the same way. This is one of our main results besides Eq. 234.

Let's break down the three terms inside parentheses in Eq. 346. The integration paths (Γ_1 and Γ_2) are usually chosen such that for the first term, the difference between the integrals along each path cancels out, rendering this term zero. The second and third terms, however, are more intriguing. In the case of the light gravimeter, the phase is given by the second term while the third term is zero because it represents the difference in initial phase offsets and both interferometer arms share the same initial phase. On the other hand, in the case of the matter gravimeter, the role of the second and third terms depend on the reference frame being used. The third term turns out to be zero in the laboratory reference but in the reference frame that follows the atom's center of mass, it assumes a non-zero value attributed to the phase "imprinted" on the atom by the laser beams [**17, 82**]. Notably, in this atom-centric frame, the second term of Eq. 346 becomes zero. Caution must be taken when interpreting these terms in the output phase of the matter gravimeter; nevertheless, notice that the total phase difference is invariant as expected.

From Eq. 346, it may seem that since the rest energy of an atom is much larger than the energy of a visible-light photon, then the interferometric signal of a matter gravimeter would be immediately larger. However, after integrating Eq. 346 (in the lab reference frame) using the usual paths of integration [**17**], it can be easily shown that $\Delta\Phi_{matter} = 2\frac{m_0\,g}{\hbar}\Delta v\,T^2$ where Δv is the change in velocity caused by the Raman transitions, and for the case of a two-photon process $\Delta v = \hbar k_0/m_0$. This result does not depend on the rest energy of the atom and only depends on the wave vector of the light use to drive the Raman transitions. In the case of the light gravimeter, after integrating using the paths and limits discussed in Section 2.5, we arrive at Eq. 234 that only depends on the wave vector of the light that interferes. We re-write the result of integrating Eq. 346 for reference

$$|\Delta\Phi_{light,matter}| = k'gT^2, \tag{347}$$

where k' is k_0 for the case of light gravimetry and k_{eff} in the case of matter gravimetry. This final equation is more suitable for comparing the performance of both gravimetry techniques. There are two scenarios for comparing the sensitivity: equal interrogation times or equal traveled distances. If we could construct both a light and a matter interferometer with the same "free-fall" time (T), and assuming k_{eff} and k_0 are equal, the phase (and therefore the sensitivity) of both interferometers would be identical. This would result in perfect equivalence between the two gravimeters at short times, where g is approximately constant. On the other hand, launching atoms upwards at small velocities (as in an atomic fountain) results in a relatively small displacement over about one second. In contrast, the light

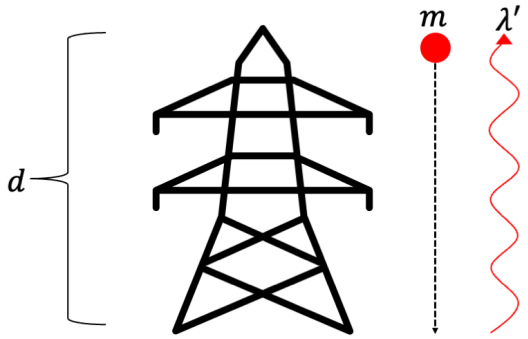

Figure 13: Thought experiment proposed by Einstein in 1911. A mass m is dropped from a tower at a distance d. When it arrives at the ground, all its energy is converted into a photon directed upwards. The photon must lose the energy given by Eq. 338 otherwise, perpetual motion could happen.

gravimeter covers this same distance in a much shorter interrogation time due to the high speed of light (c). Therefore, for equal traveled distances, the matter gravimeter has a clear advantage in terms of sensitivity.

Another interesting observation from Eq. 347, is that this equation is identical for both gravimeters except for a factor of two that appears because $k_{eff} \simeq 2k_0$ in atomic gravimeters. This difference arises because atomic gravimeters often use Raman transitions, which involve the momentum transfer of two photons. If a single-photon transition were used, the equations would be perfectly equivalent. In the atomic gravimeter, a sequence of pulses $(\pi - \pi/2 - \pi)$ is applied, with an interrogation time T between pulses. In the light gravimeter, the beam splitter acts as a $\pi/2$-pulse, while the retro-reflecting mirrors serve the role of the π-pulse, with an interrogation time T defined by the time it takes light to reach the mirror.

In summary, both types of interferometers fundamentally operate according to Eq. 346, and its phase for the usual paths of integration is given by Eq 347. Comparing them with equal interrogation times yields identical phase and sensitivity ($\Delta\Phi_{light} = \Delta\Phi_{matter}$), assuming $k_{eff} = k_0$. However, this equality comes at the cost of needing a substantially longer interferometric arm to increase the interrogation time for the light gravimeter due to the high value of the speed of light in vacuum. This requirement of very long arms is the main cause of many of the systematics analyzed in this study. A further study that considers the use of slow light could help overcome these issues since it would allow the use of much shorter arms. Enhanced sensitivity could also be achieved using more energetic photons, but this approach would require significantly more complex optical components.

2.10 Conclusions and perspectives

This chapter presented a comprehensive analysis of light-based gravimetry, demonstrating that measuring gravity using photons via gravitational redshift is fundamentally equivalent to matter-based approaches. We derived the general expression for the interferometric phase (Eq. 346) and showed that both light and matter gravimeters operate on the same physical principle, yielding identical sensitivities for equal interrogation times when $k_{eff} = k_0$. However, the high speed of light necessitates extremely long interferometric arms ($d \sim 10^8$ m) to achieve competitive sensitivities, introducing significant systematic errors from atmospheric effects (particularly refractive index variations contributing $\sim 10^7$ rad), beam misalignment (requiring $\theta < 10^{-9}$ rad), and Doppler shifts from orbital motion. While the light gravimeter offers conceptual simplicity by eliminating atomic manipulation and laser cooling systems, these stringent experimental requirements—especially precise alignment over astronomical distances and atmospheric corrections—present formidable technical challenges. Future work could explore slow-light implementations to reduce arm length requirements, multi-wavelength differential measurements to mitigate atmospheric errors, or satellite-based Mach-Zehnder configurations to avoid retro-reflection complications. The fundamental equivalence established here also suggests potential applications in testing the universality of gravitational redshift through the parameter α in space-based experiments.

Appendix

A Numerical program to simulate the decoherence of the Rabi oscillations

In this section, we will provide a heuristic proof of the condition in Eq. 210 through a numerical simulation. The sequence of pulses of Eq. 14 is applied to a cloud of atoms in free-fall. Thus, since the duration of the pulses is finite, during the process of Rabi oscillations, every atom not only undergoes a change in its internal state but also a change in its external state. Let's suppose that the atom is initially in the ground state (g) and has a moment p such that it can be described by $|\psi(0)\rangle = |g, p\rangle$. To make this state evolve, we will apply an algorithm similar to the split-operator method used in Section 1.8.6. We will consider infinitesimal steps in time and at every step, the state will evolve first in momentum and then in its internal state through the Rabi oscillations.

The change in momentum due to an infinitesimal step in time for an atom under a free-fall Hamiltonian (Eq. 140) was calculated in Eq. 154. On the other hand, the most general solution to the Rabi oscillations is given by **[28]**

$$\begin{aligned} C_g(t) &= C_g(0)\cos\frac{\Omega t}{2} - iC_e(0)\sin\frac{\Omega t}{2}, \\ C_e(t) &= C_e(0)\cos\frac{\Omega t}{2} - iC_g(0)\sin\frac{\Omega t}{2}. \end{aligned} \tag{348}$$

For infinitesimal small time steps, this solution can be approximated as

$$\begin{aligned} C_g(t) &\approx C_g(0) - iC_e(0)\frac{\Omega t}{2}, \\ C_e(t) &\approx C_e(0) - iC_g(0)\frac{\Omega t}{2}. \end{aligned} \tag{349}$$

Therefore, we can use Eqs. 154 and 349 to compute the evolution at every time step. For the first time step, the change in momentum applied to the initial state ($|\psi(0)\rangle = |g, p\rangle$) gives

$$|\psi(\Delta t)\rangle = \exp\left(-\frac{i}{\hbar}\frac{(p-\hbar\Delta k_-)^2}{2m}\Delta t\right)|g, p-\hbar\Delta k_-\rangle\,,$$

by applying the Rabi oscillations on this state gives

$$\begin{aligned} |\psi(\Delta t)\rangle = \exp\left(-\frac{i}{\hbar}\frac{(p-\hbar\Delta k_-)^2}{2m}\Delta t\right)|g, p-\hbar\Delta k_-\rangle \\ - i\frac{\Omega t}{2}\exp\left(-\frac{i}{\hbar}\frac{(p-\hbar\Delta k_-)^2}{2m}\Delta t\right)|e, p-\hbar\Delta k_-\rangle\,, \end{aligned}$$

Notice that we have defined

$$k_{\pm} \equiv \frac{ma_{\pm}}{\hbar}t, \tag{350}$$

to distinguish between the momentum transferred in the excited state from that transferred in the ground state (see Eq. 3). For the second time step, the change in momentum produces

$$\begin{aligned}|\psi(2\Delta t)\rangle = \exp\left(-\frac{i}{\hbar}\frac{(p-\hbar\Delta k_-)^2+(p-2\hbar\Delta k_-)^2}{2m}\Delta t\right)|g, p-2\hbar\Delta k_-\rangle \\ -i\frac{\Omega t}{2}\exp\left(-\frac{i}{\hbar}\frac{(p-\hbar\Delta k_-)^2+(p-\hbar\Delta k_- -\hbar\Delta k_+)^2}{2m}\Delta t\right)|e, p-\hbar\Delta k_- -\hbar\Delta k_+\rangle\,,\end{aligned}$$

while the Rabi oscillations produce

$$\begin{aligned}|\psi(2\Delta t)\rangle = \exp\left(-\frac{i}{\hbar}\frac{(p-\hbar\Delta k_-)^2+(p-2\hbar\Delta k_-)^2}{2m}\Delta t\right)|g, p-2\hbar\Delta k_-\rangle \\ -i\frac{\Omega t}{2}\exp\left(-\frac{i}{\hbar}\frac{(p-\hbar\Delta k_-)^2+(p-2\hbar\Delta k_-)^2}{2m}\Delta t\right)|e, p-2\hbar\Delta k_-\rangle \\ -i\frac{\Omega t}{2}\exp\left(-\frac{i}{\hbar}\frac{(p-\hbar\Delta k_-)^2+(p-\hbar\Delta k_- -\hbar\Delta k_+)^2}{2m}\Delta t\right)|e, p-\hbar\Delta k_- -\hbar\Delta k_+\rangle \\ -\left(\frac{\Omega t}{2}\right)^2\exp\left(-\frac{i}{\hbar}\frac{(p-\hbar\Delta k_-)^2+(p-\hbar\Delta k_- -\hbar\Delta k_+)^2}{2m}\Delta t\right)|g, p-\hbar\Delta k_- -\hbar\Delta k_+\rangle\,.\end{aligned}$$

For the third iteration, we follow the same procedure, and so on. Notice that the algorithm becomes computationally more expensive at each iteration, therefore, the procedure must be stopped after N time steps, and the amplitude of all the sub-states that ended up in the ground (excited) state can be summed to compute the global amplitude of the ground (excited) state and from this, the final population of the corresponding state can be inferred. The following program performs several simulations of this algorithm with different initial velocities (corresponding to different initial cloud temperatures [**18**]). For each simulation, the phase shift of Eq. 211 is computed and recorded as well. Finally, the phase shift due to the finite pulse duration obtained at each iteration is plotted against the corresponding visibility of the Rabi oscillations obtained through the simulation. The output of the program is shown in Fig. 14. By looking at this plot, the condition of Eq. 210 is obtained.

```
import numpy as np
import matplotlib.pyplot as plt

num_experiments = 10  # Number of simulations
rabi_steps = 26  # Number of Rabi oscillation steps

# Constants
hbar = 1e-34
m = 1e-25  # Mass of 87Rb
g = 9.8  # Gravitational acceleration
w = 1e4  # Rabi frequency
initial_velocity = 3e-3  # Initial velocity

# Parameters
magnetic_acceleration = g / 6  # Magnetic acceleration
g1 = g + magnetic_acceleration  # Acceleration 1
g2 = g - magnetic_acceleration  # Acceleration 2
t_pi = np.pi / w  # Time for a pi pulse
dt = t_pi / rabi_steps  # Time step
iw_dt_2 = -1j * w * dt / 2  # Factor for Rabi oscillations
fp = -1j * dt / (2 * m * hbar)  # Factor for temporal evolution
dp1 = m * g1 * dt  # Momentum change with g1
dp2 = m * g2 * dt  # Momentum change with g2

# Global results
cef_squared_values = []
```

```
phase_values = []

# perform simulation several times
for it in range(1, num_experiments):
    v = it * initial_velocity
    p = m * v  # Initial momentum

    phase = (m / (2 * hbar)) * (3 * v * (g1 - g2) * (t_pi ** 2) + ((g1 ** 2) - (g2 ** 2)) * (t_pi ** 3))
    phase_values.append(phase)

    pgv = np.array([p])
    pev = np.array([p])

    # begin with all population in ground state
    cgv = np.array([1 + 0j])  # Initial coefficient g
    cev = np.array([0 + 0j])  # Initial coefficient e

    time_values = np.array([0])
    cef = [cev[0]]
    cgf = [cgv[0]]

    # compute rabi oscillation for rabi_steps
    for step in range(rabi_steps):
        time_values = np.append(time_values, time_values[-1] + dt)
        pgv = np.append(pgv, pgv[-1] + dp1)
        pev = np.append(pev, pev[-1] + (dp1 if step == 0 else dp2))

        # Apply temporal evolution only to relevant elements
        cgv *= np.exp(fp * (pgv[-1] ** 2))
        cev *= np.exp(fp * (pev[-1] ** 2))

        # Rabi oscillations, doubling the number of components
        cgv_temp = np.concatenate([cgv, iw_dt_2 * cev])
        cev_temp = np.concatenate([cev, iw_dt_2 * cgv])
        cgv, cev = cgv_temp, cev_temp

        # Double the size of pgv and pev to match cgv and cev
        pgv = np.concatenate([pgv, np.full(len(cgv) - len(pgv), pgv[-1])])
        pev = np.concatenate([pev, np.full(len(cev) - len(pev), pev[-1])])

        # Update the final coefficients
        cgf.append(np.sum(cgv))
        cef.append(np.sum(cev))

        # Add a new time value only after completing all operations
        time_values = np.append(time_values, time_values[-1] + dt)

    # Ensure that time_values and cef have the same length
    time_values = time_values[:len(cef)]

    cef_squared = np.abs(cef) ** 2

    # Plot (adjust according to reference data)
    plt.plot(time_values, cef_squared)
    plt.xlabel('time (s)')
    plt.ylabel('|c_e|^2')
    plt.text(t_pi / 10, 0.6, f'phase: {phase}')
    plt.pause(0.3)

    cef_squared_values.append(cef_squared[-1])

# Final plot
plt.figure()
plt.plot(phase_values, cef_squared_values)
plt.xlabel('phase')
plt.ylabel('|c_e(t=t_pi)|^2')
plt.show()
```

Listing 1: Python code for the simulation of decoherence of the Rabi oscillations in a magnetic gravimeter.

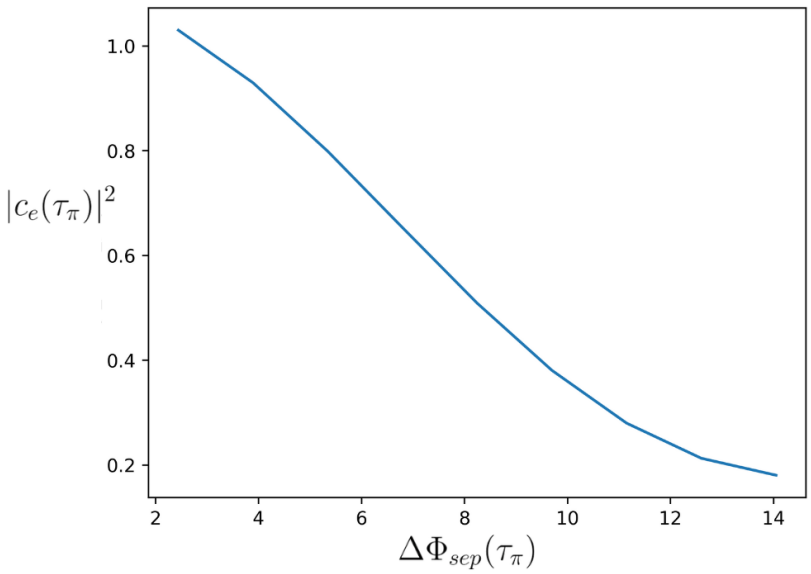

Figure 14: Phase shift due to the finite duration of a π-pulse used to drive Rabi oscillations (Eq. 211) versus the population of the excited state immediately after the pulse is applied. All the population is initially in the ground state, thus, full visibility means that after the pulse is applied all the population is transferred to the excited state. Notice that when the phase shift is of the order of π, the visibility is reduced significantly, this establishes the condition in Eq. 210.

References

[1] N.P. Robins, P.A. Altin, J.E. Debs, and J.D. Close. Atom lasers: Production, properties and prospects for precision inertial measurement. *Physics Reports*, 529(3):265–296, 2013.

[2] Savas Dimopoulos, Peter W. Graham, Jason M. Hogan, Mark A. Kasevich, and Surjeet Rajendran. Atomic gravitational wave interferometric sensor. *Phys. Rev. D*, 78:122002, Dec 2008.

[3] Savas Dimopoulos, Peter W. Graham, Jason M. Hogan, Mark A. Kasevich, and Surjeet Rajendran. Gravitational wave detection with atom interferometry. *Physics Letters B*, 678(1):37–40, 2009.

[4] Jan Harms, Bram J. J. Slagmolen, Rana X. Adhikari, M. Coleman Miller, Matthew Evans, Yanbei Chen, Holger Müller, and Masaki Ando. Low-frequency terrestrial gravitational-wave detectors. *Phys. Rev. D*, 88:122003, Dec 2013.

[5] Rym Bouchendira, Pierre Cladé, Saïda Guellati-Khélifa, François Nez, and François Biraben. New determination of the fine structure constant and test of the quantum electrodynamics. *Phys. Rev. Lett.*, 106:080801, Feb 2011.

[6] J. B. Fixler, G. T. Foster, J. M. McGuirk, and M. A. Kasevich. Atom interferometer measurement of the Newtonian constant of gravity. *Science*, 315(5808):74–77, 2007.

[7] Holger Müller, Sheng-wey Chiow, Sven Herrmann, Steven Chu, and Keng-Yeow Chung. Atom-interferometry tests of the isotropy of post-Newtonian gravity. *Phys. Rev. Lett.*, 100:031101, Jan 2008.

[8] Vincent Ménoret, Pierre Vermeulen, Nicolas Le Moigne, Sylvain Bonvalot, Philippe Bouyer, Arnaud Landragin, and Bruno Desruelle. Gravity measurements below 10^{-9} g with a transportable absolute quantum gravimeter. *Scientific Reports*, 8(1):12300, Aug 2018.

[9] Ben Stray, Andrew Lamb, Aisha Kaushik, Jamie Vovrosh, Anthony Rodgers, Jonathan Winch, Farzad Hayati, Daniel Boddice, Artur Stabrawa, Alexander Niggebaum, Mehdi Langlois, Yu-Hung Lien, Samuel Lellouch, Sanaz Roshanmanesh, Kevin Ridley, Geoffrey de Villiers, Gareth Brown, Trevor Cross, George Tuckwell, Asaad Faramarzi, Nicole Metje, Kai Bongs, and Michael Holynski. Quantum sensing for gravity cartography. *Nature*, 602(7898):590–594, Feb 2022.

[10] Bin Chen, Jinbao Long, Hongtai Xie, Chenyang Li, Luokan Chen, Bonan Jiang, and Shuai Chen. Portable atomic gravimeter operating in noisy urban environments. *Chin. Opt. Lett.*, 18(9):090201, Sep 2020.

[11] Michel Van Camp, Olivier de Viron, Arnaud Watlet, Bruno Meurers, Olivier Francis, and Corentin Caudron. Geophysics from terrestrial time-variable gravity measurements. *Reviews of Geophysics*, 55(4):938–992, 2017.

[12] Wolfgang Torge and Jürgen Müller. *Geodesy*. De Gruyter, Berlin, Boston, 2012.

[13] Jorge Padín, Angel Martín, and Ana Belén Anquela. Archaeological microgravimetric prospection inside don church (Valencia, Spain). *Journal of Archaeological Science*, 39(2):547–554, 2012.

[14] Jaroslava Panisova, Marek Fraštia, Tina Wunderlich, Roman Pašteka, and David Kušnirák. Microgravity and ground-penetrating radar investigations of subsurface features at the St Catherine's Monastery, Slovakia. *Archaeological Prospection*, 20(3):163–174, 2013.

[15] I. Bishop, P. Styles, S. J. Emsley, and N. S. Ferguson. The detection of cavities using the microgravity technique: case histories from mining and karstic environments. *Geological Society, London, Engineering Geology Special Publications*, 12(1):153–166, 1997.

[16] Daniele Carbone, Michael P. Poland, Michel Diament, and Filippo Greco. The added value of time-variable microgravimetry to the understanding of how volcanoes work. *Earth-Science Reviews*, 169:146–179, 2017.

[17] A Peters, K Y Chung, and S Chu. High-precision gravity measurements using atom interferometry. *Metrologia*, 38(1):25, feb 2001.

[18] Edgar Zuniga, Eduardo Gomez, and Luis Octavio Castanos-Cervantes. Precision limits of magnetic T^3-atomic gravimetry due to atomic cloud expansion. *Phys. Rev. A*, 109:013304, Jan 2024.

[19] M. Kasevich and S. Chu. Measurement of the gravitational acceleration of an atom with a light-pulse atom interferometer. *Applied Physics B*, 54(5):321–332, May 1992.

[20] L. O. Castaños and E. Gomez. Model for a phase-space selector using microwave transitions. *Physical Review A - Atomic, Molecular, and Optical Physics*, 89(1):1–26, 2014.

[21] Jason M. Hogan, David M. S. Johnson, and Mark A. Kasevich. Light-pulse atom interferometry. `https://arxiv.org/abs/0806.3261`, 2008.

[22] Manolo R. Lam, Natalie Peter, Thorsten Groh, Wolfgang Alt, Carsten Robens, Dieter Meschede, Antonio Negretti, Simone Montangero, Tommaso Calarco, and Andrea Alberti. Demonstration of quantum brachistochrones between distant states of an atom. *Phys. Rev. X*, 11:011035, Feb 2021.

[23] Andreas Steffen, Andrea Alberti, Wolfgang Alt, Noomen Belmechri, Sebastian Hild, Michał Karski, Artur Widera, and Dieter Meschede. Digital atom interferometer with single particle control on a discretized space-time geometry. *Proceedings of the National Academy of Sciences*, 109(25):9770–9774, 2012.

[24] M. Zimmermann, M. A. Efremov, A. Roura, W. P. Schleich, S. A. DeSavage, J. P. Davis, A. Srinivasan, F. A. Narducci, S. A. Werner, and E. M. Rasel. T3-interferometer for atoms. *Applied Physics B*, 123(4):102, Mar 2017.

[25] O. Amit, Y. Margalit, O. Dobkowski, Z. Zhou, Y. Japha, M. Zimmermann, M. A. Efremov, F. A. Narducci, E. M. Rasel, W. P. Schleich, and R. Folman. T^3 stern-gerlach matter-wave interferometer. *Phys. Rev. Lett.*, 123:083601, Aug 2019.

[26] KAUSHAL SK and WETHERILL GW. Rubidium 87- strontium 87 age of carbonaceous chondrites. *J Geophys Res*, 75(2):463–468, 1970.

[27] Carlos F. Bunge, José A. Barrientos, and A. V. Bunge. Roothaan-Hartree-Fock ground-state atomic wave functions: Slater-type orbital expansions and expectation values for Z = 2-54. *Atomic Data and Nuclear Data Tables*, 53(1):113–162, 1993.

[28] J.J. Sakurai and J. Napolitano. *Modern Quantum Mechanics*. Cambridge University Press, 2017.

[29] Daniel Adam Steck. Rubidium 87 D Line Data. *Journal of Geophysical Research*, 2009(2):31, 2010.

[30] Stefano Scotto. *Rubidium Vapors in High Magnetic Fields*. Phd thesis, Université Paul Sabatier - Toulouse III, 2016. NNT: 2016TOU30318, tel-01482289v2.

[31] S. Gasiorowicz. *Quantum Physics*. Wiley, 2003.

[32] Richard P Feynman. *Statistical Mechanics: A Set of Lectures*, chapter 2, pages 46–53. Frontiers in Physics. Perseus Books, Boulder, CO, 7 edition, December 1972.

[33] Harold J. Metcalf and Peter van der Straten. *Optical Traps for Neutral Atoms*, pages 149–164. Springer New York, New York, NY, 1999.

[34] M.D Feit, J.A Fleck, and A Steiger. Solution of the Schrödinger equation by a spectral method. *Journal of Computational Physics*, 47(3):412–433, 1982.

[35] C Leforestier, R.H Bisseling, C Cerjan, M.D Feit, R Friesner, A Guldberg, A Hammerich, G Jolicard, W Karrlein, H.-D Meyer, N Lipkin, O Roncero, and R Kosloff. A comparison of different propagation schemes for the time dependent Schrödinger equation. *Journal of Computational Physics*, 94(1):59–80, 1991.

[36] P.A. Maksym and H. Aoki. Fast split operator method for computation of time dependent quantum states of bilayer graphene in a magnetic field. *Physica E: Low-dimensional Systems and Nanostructures*, 112:66–70, 2019.

[37] Shev MacNamara and Gilbert Strang. Operator splitting. In Roland Glowinski, Stanley J. Osher, and Wotao Yin, editors, *Splitting Methods in Communication, Imaging, Science, and Engineering*, pages 95–114. Springer International Publishing, Cham, 2016.

[38] Donald A McQuarrie. *Statistical Mechanics*. Harper's chemistry series. Longman, London, England, December 1976.

[39] Philip R. Bevington, D. Keith Robinson, J. Morris Blair, A. John Mallinckrodt, and Susan McKay. Data reduction and error analysis for the physical sciences, 1993.

[40] A. Bertoldi, F. Minardi, and M. Prevedelli. Phase shift in atom interferometers: Corrections for nonquadratic potentials and finite-duration laser pulses. *Phys. Rev. A*, 99:033619, Mar 2019.

[41] S. Y. Chen and T. C. Ralph. Estimation of gravitational acceleration with quantum optical interferometers. *Phys. Rev. A*, 99:023803, Feb 2019.

[42] Makan Mohageg, Luca Mazzarella, Charis Anastopoulos, Jason Gallicchio, Bei-Lok Hu, Thomas Jennewein, Spencer Johnson, Shih-Yuin Lin, Alexander Ling, Christoph Marquardt, Matthias Meister, Raymond Newell, Albert Roura, Wolfgang P. Schleich, Christian Schubert, Dmitry V. Strekalov, Giuseppe Vallone, Paolo Villoresi, Lisa Wörner, Nan Yu, Aileen Zhai, and Paul Kwiat. The deep space quantum link: prospective fundamental physics experiments using long-baseline quantum optics. *EPJ Quantum Technology*, 9(1):25, Oct 2022.

[43] Ta-Pei Cheng. *Relativity, Gravitation and Cosmology*. Oxford Master Series in Physics. Oxford University Press, London, England, December 2004.

[44] A. M. Nobili, D. M. Lucchesi, M. T. Crosta, M. Shao, S. G. Turyshev, R. Peron, G. Catastini, A. Anselmi, and G. Zavattini. On the universality of free fall, the equivalence principle, and the gravitational redshift. *American Journal of Physics*, 81(7):527–536, 07 2013.

[45] Michael Nauenberg. Einstein's equivalence principle in quantum mechanics revisited. *American Journal of Physics*, 84(11):879–882, 11 2016.

[46] A. Coley. Schiff's conjecture on gravitation. *Phys. Rev. Lett.*, 49:853–855, Sep 1982.

[47] Eugene Hecht. *Optics, Global Edition*. Pearson Education, London, England, 5 edition, October 2016.

[48] Malvin Carl Teich and Bahaa E A Saleh. *Fundamentals of Photonics*. Wiley Series in Pure and Applied Optics. John Wiley & Sons, Nashville, TN, 2 edition, September 1991.

[49] Mark Kasevich and Steven Chu. Atomic interferometry using stimulated raman transitions. *Phys. Rev. Lett.*, 67:181–184, Jul 1991.

[50] Zhang, Mingyue, Müller, Jürgen, Biskupek, Liliane, and Singh, Vishwa Vijay. Characteristics of differential lunar laser ranging. *A&A*, 659:A148, 2022.

[51] James G. Williams, Luca Porcelli, Simone Dell'Agnello, Lorenza Mauro, Marco Muccino, Douglas G. Currie, Dennis Wellnitz, Chensheng Wu, Dale H. Boggs, and Nathan H. Johnson. Lunar laser ranging retroreflectors: Velocity aberration and diffraction pattern. *The Planetary Science Journal*, 4(5):89, may 2023.

[52] P Villoresi, T Jennewein, F Tamburini, M Aspelmeyer, C Bonato, R Ursin, C Pernechele, V Luceri, G Bianco, A Zeilinger, and C Barbieri. Experimental verification of the feasibility of a quantum channel between space and earth. *New Journal of Physics*, 10(3):033038, mar 2008.

[53] Giuseppe Vallone, Daniele Dequal, Marco Tomasin, Francesco Vedovato, Matteo Schiavon, Vincenza Luceri, Giuseppe Bianco, and Paolo Villoresi. Interference at the single photon level along satellite-ground channels. *Phys. Rev. Lett.*, 116:253601, Jun 2016.

[54] Daniele Dequal, Giuseppe Vallone, Davide Bacco, Simone Gaiarin, Vincenza Luceri, Giuseppe Bianco, and Paolo Villoresi. Experimental single-photon exchange along a space link of 7000 km. *Phys. Rev. A*, 93:010301, Jan 2016.

[55] Luca Calderaro, Costantino Agnesi, Daniele Dequal, Francesco Vedovato, Matteo Schiavon, Alberto Santamato, Vincenza Luceri, Giuseppe Bianco, Giuseppe Vallone, and Paolo Villoresi. Towards quantum communication from global navigation satellite system. *Quantum Science and Technology*, 4(1):015012, dec 2018.

[56] D.E. Smith. Determination of the earth's gravitational potential from satellite orbits. *Planetary and Space Science*, 8(1):43–48, 1961.

[57] D. G. King-Hele. The Earth's Gravitational Potential, deduced from the Orbits of Artificial Satellites. *Geophysical Journal International*, 4(Supplement$_1$) : 3 − −16, 121961.

[58] George B. Arfken, Hans J. Weber, and Frank E. Harris. Chapter 15 - legendre functions. In George B. Arfken, Hans J. Weber, and Frank E. Harris, editors, *Mathematical Methods for Physicists (Seventh Edition)*, pages 715–772. Academic Press, Boston, seventh edition edition, 2013.

[59] R. H. Merson. The motion of a satellite in an axi-symmetric gravitational field. *Geophysical Journal of the Royal Astronomical Society*, 4(S0):17–52, 1961.

[60] John P. Vinti. Representation of the earth's gravitational potential. *Celestial mechanics*, 4(3):348–367, Dec 1971.

[61] D. G. KING-HELE, G. E. COOK, and JANICE M. REES. Earth's gravitational potential: Evaluation of even zonal harmonics from the 2nd to the 12th. *Nature*, 197(4869):785–785, Feb 1963.

[62] R. R. NEWTON, H. S. HOPFIELD, and R. C. KLINE. Odd harmonics of the earth's gravitational field. *Nature*, 190(4776):617–618, May 1961.

[63] S.M. Klosko and C.A. Wagner. Spherical harmonic representation of the gravity field from dynamic satellite data. *Planetary and Space Science*, 30(1):5–28, 1982.

[64] Frédéric Chambat and Bernard Valette. Mean radius, mass, and inertia for reference earth models. *Physics of the Earth and Planetary Interiors*, 124(3):237–253, 2001.

[65] Wolfram Alpha LLC. Wolfram|alpha, 2024. Accessed September 9, 2024.

[66] Guennadi N. Belozerski. Mössbauer spectroscopy, applications*. In John C. Lindon, editor, *Encyclopedia of Spectroscopy and Spectrometry (Second Edition)*, pages 1573–1583. Academic Press, Oxford, second edition edition, 1999.

[67] Charles W Misner, Kip S Thorne, and John Archibald Wheeler. *Gravitation*. Princeton University Press, Princeton, NJ, 2017.

[68] Bernard Schutz. *A First Course in General Relativity*. Cambridge University Press, 3 edition, 2022.

[69] Edson R. Peck and Kaye Reeder. Dispersion of air*. *J. Opt. Soc. Am.*, 62(8):958–962, Aug 1972.

[70] Philip E. Ciddor. Refractive index of air: new equations for the visible and near infrared. *Appl. Opt.*, 35(9):1566–1573, Mar 1996.

[71] L. J. Yang, H. Y. Zhang, Y. Li, and H. Y. Wei. Absolute group refractive index measurement of air by dispersive interferometry using frequency comb. *Opt. Express*, 23(26):33597–33607, Dec 2015.

[72] A. Börzsönyi, Z. Heiner, M. P. Kalashnikov, A. P. Kovács, and K. Osvay. Dispersion measurement of inert gases and gas mixtures at 800 nm. *Appl. Opt.*, 47(27):4856–4863, Sep 2008.

[73] Gábor Lente and Katalin Ősz. Barometric formulas: various derivations and comparisons to environmentally relevant observations. *ChemTexts*, 6(2):13, Apr 2020.

[74] Gérard C. Nihous. Notes on hydrostatic pressure. *Journal of Ocean Engineering and Marine Energy*, 2(1):105–109, Feb 2016.

[75] Howard D. Goodfellow and Eric F. Curd. Chapter 4 - physical fundamentals. In Howard D. Goodfellow and Risto Kosonen, editors, *Industrial Ventilation Design Guidebook (Second Edition)*, pages 39–109. Academic Press, second edition edition, 2020.

[76] Jean Meeus. *Astronomical Algorithms*. Atlantic Books, Royal Tunbridge Wells, England, 2 edition, December 1998.

[77] John David Jackson. *Classical electrodynamics*. John Wiley & Sons, 2012.

[78] Leonard Mandel and Emil Wolf. Preface. In *Optical Coherence and Quantum Optics*. Cambridge University Press, Cambridge, September 1995.

[79] J. M. Cervantes, M. A. Maldonado, J. A. Franco-Villafañe, T. Roach, V. M. Valenzuela, and E. Gomez. Selection of a raman beam waist in atomic gravimetry. *OSA Continuum*, 4(7):1996–2007, Jul 2021.

[80] John E. Debs, Kyle S. Hardman, Paul A. Altin, Gordon McDonald, John D. Close, and Nicholas P. Robins. From apples to atoms: measuring gravity with ultra cold atomic test masses. *Preview*, 2013(164):30–33, 2013.

[81] A. Einstein. Über den einfluß der schwerkraft auf die ausbreitung des lichtes. *Annalen der Physik*, 340(10):898–908, 1911.

[82] Peter Wolf, Luc Blanchet, Christian J Bordé, Serge Reynaud, Christophe Salomon, and Claude Cohen-Tannoudji. Does an atom interferometer test the gravitational redshift at the compton frequency? *Classical and Quantum Gravity*, 28(14):145017, jun 2011.